

THESIS

Study of nano-roughness for silica-on-silicon technology by Scanning Electron Microscopy and light scattering.

to obtain the

DOCTORATE DEGREE

in

THE LOUIS PASTEUR UNIVERSITY OF STRASBOURG

Speciality: Engineering Sciences - Photonics

by

Alexis BONY

Host laboratory: Alcatel SEL AG, Research and Innovation Center in Photonics – Passive Components Division, Stuttgart, Germany.

University laboratory: Laboratoire des Systèmes Photoniques – EA2312, Illkirch, France.

Defended the 6th of December 2004 before the doctoral committee:

MEYRUEIS Patrick	Professor – Louis Pasteur University, Strasbourg, France.
MONTGOMERY Paul C.	Researcher – CNRS-PHASE, Strasbourg, France.
GORECKI Christophe	Research Director – CNRS-LOPMD, Besançon, France.
O'DONNELL Kevin A.	Professor – CICESE, Enseñada, Mexico.
TAKAKURA Yoshitane	Researcher – Louis Pasteur University, Strasbourg, France.
SATZKE Klaus	Researcher – Alcatel SEL AG, Stuttgart, Germany

A mes parents.

Acknowledgements

I owe thanks to many people who helped me at different stages of this Ph.D.

First of all, I am indebted to Yoshitake Takakura for his permanent availability, assistance, and patience, despite the null administrative advantage he could receive from this task. Yoshi's usual approach, which consists in criticizing every idea, result, measurement, or data, although sometimes driving to despair, proved to be an indispensable mentor during this work.

Organizing a Ph.D. work between a company and a university requires time and persistence, and I am glad to thank Dr. Kurt Lösch, Dr. Armin Baumgärtner and Dr. Klaus Satzke, from Alcatel SEL AG, and Prof. Meyrueis, from the Photonic Systems Laboratory of Louis Pasteur University for the faith they granted me.

Constituting a jury is not an easy task for a Ph.D. student, and I would like to thank Dr. Paul Montgomery, Dr. Christophe Gorecki, and Prof. Kevin O'Donnell for having accepted evaluating this work with enthusiasm.

I had initially planned to cite all the people who helped me in many ways during this Ph.D., and started writing a list in order to be sure not to forget anybody. Unfortunately, the size of this list would generate a new paragraph to be fulfilled. However, I would particularly like to acknowledge André Heid, who trained me using the SEM, and was always available to answer my numerous questions, and André Bilger, who prepared the mechanical pieces for the light scattering experiment.

Carrying out a Ph.D. brings its dose of stress, and I would like to thank the persons who shared my life during this period for their patience and support.

As a Ph.D. is often considered as the end of one's education, I would like to thank my parents for their convinced and unalterable encouragement. Their first priority has always remained the achievement of my aspirations or wishes (even at the expense of financial reason), and these few lines are only a poor compensation in comparison with the invaluable heritage they gave me.

Table of contents

I	Introduction	12
I.1	What is roughness	12
I.1.1	Defining roughness	12
I.1.2	Roughness and light scattering	15
I.2	Measuring roughness	16
I.2.1	Instruments for surface roughness measurement	16
I.2.2	Comparison between instruments	28
I.3	Silica-on-silicon optical waveguides	29
I.3.1	Materials and fabrication	29
I.3.2	Applications	30
I.3.3	Roughness formation	30
II	SEM-based waveguide sidewall roughness measurement	32
II.1	State of the art of available techniques for sidewall roughness measurement	32
II.2	Visual inspection and Line-Edge Roughness measurement	35
II.2.1	Sidewall quality assessment via visual inspection	36
II.2.2	Line-Edge Roughness measurement	38
II.3	Stereoscopic approach	41
II.3.1	Theoretical description of the procedure	41
II.3.2	Practical implementation	45
II.3.3	Results	48
II.3.4	Conclusion on stereoscopic approach	51
II.4	Shape-from-shading approach	52
II.4.1	Algorithm implementation	52
II.4.2	Profile reconstruction	53
II.4.3	Calibration issues	55
II.4.4	Roughness distinction and resolution	56
II.4.5	Issues for practical implementation	57
II.4.6	Extension to deep silica etching	65
II.5	Comparison of stereoscopy, SFS, and competing techniques	67
II.5.1	Comparison of stereoscopy and shape-from-shading techniques	67
II.5.2	Comparison with competing techniques	68
II.6	Ideas for further developments	69
III	Light scattering from silica-on-silicon wafers	70
III.1	Physical description of the studied phenomena	70
III.1.1	Physical origin of speckle	70
III.1.2	Speckle correlations	72
III.1.3	Angle-resolved light scattering	74
III.2	Experimental aspects	75
III.2.1	Experimental set-up	75
III.2.2	Description of the samples	78
III.3	Angle-resolved light scattering	82
III.3.1	Diffused fringes	82
III.3.2	Thickness retrieval	86
III.3.3	Grazing angle approach	89
III.3.4	Retrodiffusion approach	91
III.4	Speckle correlations	94
III.4.1	Principles of speckle pattern recording and of correlation evaluation	94

III.4.2	Experimental angle-resolved speckle correlations	95
III.4.3	Alternative way of evaluating speckle correlation (via digital correlation calculation in Fourier plane)	97
III.4.4	$C^{(10)}$ correlation condition	103
III.5	Conclusions on speckle and light scattering studies	105
	Bibliography.....	108

Table of Figures

Figure 1: Personal translation from French version "Garfield travaille du chapeau", Jim Davis.	8
Figure 2: Classification of surface errors (reproduced and adapted from [Briers, 1993]).	12
Figure 3: Example of stylus system (from Veeco documents).	17
Figure 4: Schematic view of the scanning tunneling microscope.	18
Figure 5: Interatomic force vs. distance curve(left), and principle of operation of the AFM (right).	19
Figure 6: Schematics of secondary electron detectors (after JEOL documents).	21
Figure 7: Components of SEM (left) and schematics of LEO GEMINI 1550 column (right).	22
Figure 8: Working principle of a confocal microscope.	24
Figure 9: Different types of objectives settled in interferometric microscopes (from [Aziz, 2000]).	25
Figure 10: Principles of wavefront local tilts acquisition (from [Platt, 2001]).	26
Figure 11: The three basic steps for silica optical waveguide fabrication.	30
Figure 12 : SEM-images of waveguide sidewall showing evidence of roughness	31
Figure 13: AFM tip geometry for sidewall inspection (from [Nyysönen, 1991]).	32
Figure 14: Si sidewall imaged by AFM (from [Juan, 1996]).	33
Figure 15: Overview of waveguide sidewall topography on test sample.	35
Figure 16: Two examples of sidewall roughness aspect.	36
Figure 17: Etched sidewalls compared in [BAZYLENKO, 1996a].	36
Figure 18: Typical SEM image for LER measurement.	38
Figure 19: Initial SEM (left) and Sobel-filtered (right) images	39
Figure 20: Thresholded image (left) and extracted profile (right).	39
Figure 21: Auto-correlation for LER-extracted profile.	40
Figure 22: SEM plane of view (left), symmetrical tilts around y -axis.	42
Figure 23: Non-tilted (left) and tilted (right) sample configuration for optimal sidewall imaging.	43
Figure 24: Two stereoscopic images of the same waveguide sidewall area.	45
Figure 25: Definition of the reconstruction parameters	46
Figure 26: Reference SEM image with rectangle selected for topography calculation and corresponding reconstructed waveguide sidewall profile.	48
Figure 27: Auto-correlation along x -direction for sidewall stereo-reconstructed profile.	51
Figure 28: Reconstructed waveguide sidewall profile (left) and corresponding SEM image area (right).	54
Figure 29: Pixel value histogram for the subtraction of filtered image to original image.	54
Figure 30: Reconstructed profiles from initial SEM image (left) and low-pass filtered SEM image (right).	55
Figure 31: SEM image of 2 nd sample and inspected area (left), and corresponding reconstructed profile (right).	56
Figure 32: Original (a), contrast-stretched (b), median-processed (c), histogram-equalized (d) images.	61
Figure 33: Intensity histograms corresponding to original (a), contrast-stretched (b), median- processed (c), histogram-equalized (d) images.	62
Figure 34: Profile standard deviation as a function of vertical position on the sidewall, extracted from original SEM image (lower) and contrast-stretched image (upper).	63
Figure 35 : Sidewall from 40 μ m-etched silica sample.	65
Figure 36: Set-up for imaged (subjective) speckle pattern recording (from [Fricke-Begemann, 2004]).	71

Figure 37: Set-up for far-field (objective) speckle pattern recording (from [Hamed, 2004])..	71
Figure 38: Notations for angles of illumination and scattering.....	72
Figure 39: Experimental set-up for angle-resolved light measurement (adapted from [Takakura, 1996]).....	75
Figure 40: Set-up for angle-resolved speckle pattern recording.	76
Figure 41: Typical speckle pattern (left) and histogram of pixel intensity data (right).	77
Figure 42: Mechanical part to ensure alignment of CCD camera with rotation arm.	78
Figure 43: SEM image of sample C.	79
Figure 44: Thickness fluctuations for sample M1_1548_1.....	80
Figure 45: Overview of angle-resolved scattered intensity for sample C, $\theta_i = 5^\circ$	82
Figure 46: Angle-resolved intensity measurement for sample B and C, $\theta_i = 5^\circ$	83
Figure 47: Forward and back scattered angle-resolved intensity for sample B.	84
Figure 48: Angle-resolved intensity for sample C, with $\theta_i = 5^\circ$ (upper) and $\theta_i = 10^\circ$ (lower).	84
Figure 49: Thickness estimation for sample C.....	87
Figure 50: Thickness estimation for sample B.....	88
Figure 51: Speckle pattern obtained with an angle incidence of 80°	90
Figure 52: Retroreflection as a function of the angle of incidence for different thickness fluctuation amplitudes σ_H (from [Blumberg, 2002]).....	92
Figure 53: Two experimental sets of retroreflections curves from [Blumberg, 2002].	93
Figure 54: Correlation in the reciprocal scattering configuration as a function of θ_{s2} for fixed θ_{i2} (initially 10°). (Curves at 15° and 20° are superimposed and shifted for clarity).....	96
Figure 55: Correlation (down) and intensity (up) for sample C as a function of θ_{s2} , for p-p polarization.....	97
Figure 56: Correlation peak for two identical speckle images.....	99
Figure 57: Correlation peak for sample A in reciprocal configuration with $\theta_{i1} = 10^\circ$	99
Figure 58: Correlation image for sample A in reciprocal configuration, $\theta_{i1} = 15^\circ$ (left) and $\theta_{i1} = 20^\circ$ (right).....	100
Figure 59: Correlation peak for sample A in reciprocal configuration with $\theta_{i1} = 30^\circ$	100
Figure 60: Correlation image for sample C, same condition as for Figure 55, $\theta_{s2} = 20.2^\circ$	101
Figure 61: Same as Figure 60, but $\theta_{s2} = 24.6^\circ$ (left) and $\theta_{s2} = 25.6^\circ$ (right).	101
Figure 62: Correlation image, sample B, same conditions as Table 8, with $\theta_{i2} = 6^\circ$ (left) and $\theta_{i2} = 9^\circ$ (right).....	102
Figure 63: Same as Figure 57, but with preliminary zero-padding.....	102

Forewords... or pseudo-Ph.ilosophical forewords for this D.octoral work.

Why to start a Ph.D. ?

Among the various available responses to potential candidates, ranging from obtaining title to personal achievement, a rather intuitive one is *simply* "to do research". Research then appears like being on the opposite side (at least on the Eastern side of the Atlantic) as making business, money. But the global trend launched by steering institutions, industrial (technological market breakthrough) and academic needs (fundings, technological implementation of initially abstract ideas), goes in the sense of an attenuation of this opposition.

But what is behind the word research ?

Research is often coupled with development, the latter having the oriented meaning towards device prototyping or method elaboration. One may also link research with teaching, the expertise necessary to accomplish scientific investigation being a prerequisite. But such a direct definition based on semantic distinctions may all the more not satisfy us in our quest of "research" since the terms previously evoked are generally interpenetrated, and consequently not plainly distinguishable.

An alternative definition could be given in terms of objectives to be achieved, and sorted out between finding a solution to a given problem or exploring a new field. Attempts were made to pursue both objectives in this Ph.D.

Research and development... or Connecting the dots.

For the first case, ab initio completely new solutions are extremely scarcely to appear, and require either brilliant intuition either long maturation time. Therefore, another approach was selected, which is illustrated below.

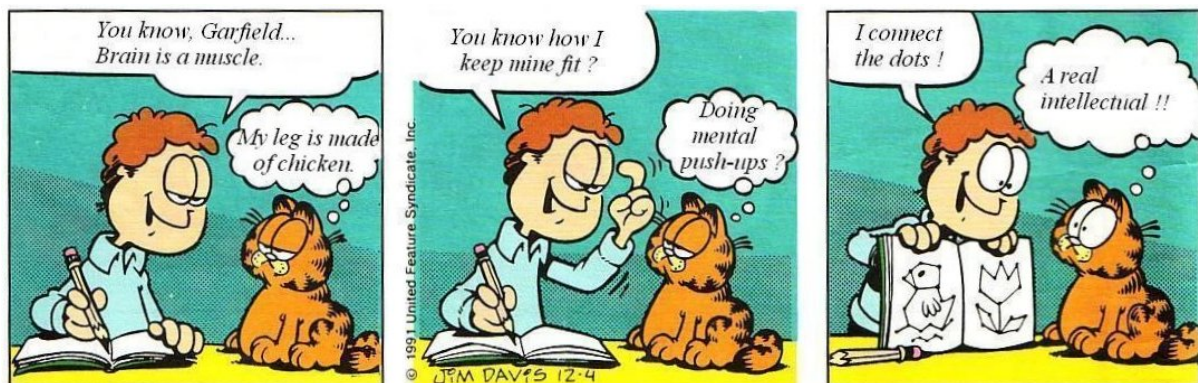
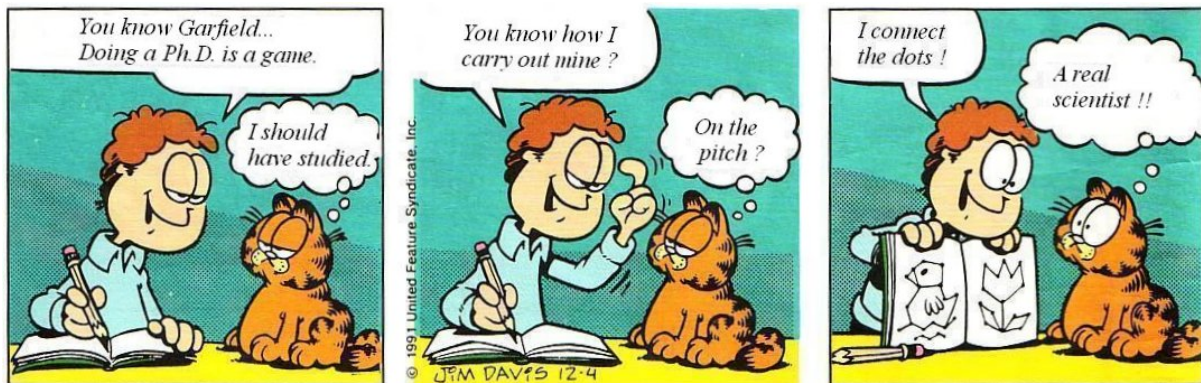


Figure 1: Personal translation from French version "Garfield travaille du chapeau", Jim Davis.

With a bit of imagination, one reaches the following dialog.



We therefore tried to connect a few dots to carry out research and development. First, between industry and academic institutions, then between several existing fields of science or technical solutions.

For the second case, we tried to repeat experiments previously reported in literature, and then to extend them taking into account the own nature of our samples or set-ups.

...and objectives.

Due to its collaboration context, the objectives for this Ph.D. were of double nature. First, from the industrial side, the need for a waveguide sidewall roughness measurement method was expressed. The investigation was thus oriented towards the development of a non-destructive characterization technique on full wafer, using available equipment (namely scanning electron microscope). The dots chosen to be connected were thus scanning electron microscopy with image-based shape-extraction techniques.

On the more academic side, the efforts were oriented towards a better experimental understanding of angle-resolved light scattering and speckle correlations obtained from silica-on-silicon wafers (with the intent to generalize the results to any transparent-on-reflector system). Particularly, flame hydrolysis deposited silica-on-silicon wafers present the interesting feature of having multiple-scale topography variations. The ultimate idea (objective) was thus to carry out a feasibility study on the application of angle-resolved light scattering and speckle correlation for roughness and waviness measurements.

General introduction

The last decade developments in optical telecommunications have involved wide use of glass fibers for data transmission. Whereas those fibers are typically settled for long information carrier lines across oceans, small optical components have been used as a companion to route signals between them, or multiplex the information content sent via a fiber. Silica-on-silicon technology is the candidate selected at Alcatel SEL for the realization of such optical components, and consists of several silica layers with distinct refractive index deposited on a silicon substrate. It presents the definite advantage to enable fast index matching when coupling them to optical fibers. This characteristic is a first step towards propagation loss reduction, which is a prerequisite to avoid too frequent signal regeneration.

As a common feature, these components contain several optical waveguides, which are etched into silica. The etching being highly anisotropic, it usually results in the presence of surface roughness on the sides of these waveguides, what is referred to as sidewall roughness. This sidewall roughness has been identified to be an important source of optical power loss, and one may then wish to reduce, or at least control, its amplitude. A motivation of the work reported here is consequently the development of an easy way of assessing these sidewall roughnesses.

Before optical waveguides are etched into silica, the wafers used for component fabrication constitute a system of a transparent (for visible light) layer over a reflecting substrate. The study of such a system dates long back in the history of optics, but efforts are still active to understand its scattering properties when illuminated with laser light. Particularly, the influence of surface roughness amplitude at the upper interface (air/transparent layer) is still subject to discussion, and thickness fluctuations have been evidenced to play a significant role in the scattering process. A second motivation for the work reported here is thus to experimentally investigate further laser light scattered by such samples, both in terms of angular intensity distribution and speckle correlations, with the idea to use these properties as a surface probe.

This thesis is divided into three chapters, that are organized as follows. Chapter 1 recalls the fundamentals in studies related to surface roughness. This consists first in a definition of what is usually referred to as roughness, and then in a review of different available techniques and instruments for surface topography investigation. This step is necessary, as roughness evaluation is always a trade-off between experimental requirements, sample-related constraints, and available/accessible equipment. In the same vein, silica-on-silicon wafer and waveguide fabrication are reminded.

Chapter 2 deals with sidewall roughness evaluation for optical waveguide. A survey of already reported techniques for this challenge orientates this work towards scanning electron microscopy as a tool for inspection. After the description of a widespread practice that consists in looking at a waveguide's edge's variations from its top (line edge roughness measurement), the core of this chapter presents two original approaches for quantitative sidewall roughness estimation developed within this work. The first one is based on stereoscopy, and efforts are reported to detail both theoretical modeling of the procedure, its

practical implementation, and to comment its results. The second approach relies on the application of a shape-from-shading algorithm, and much care is dedicated to the quality of the reconstructed surface profile, its calibration in terms of height values, and the reproducibility of the procedure.

Chapter 3 reports work carried out for angle-resolved light scattering measurement and speckle correlation. A set-up was built up during this work, and practical details on its realization are first given. Angle-resolved intensity measurement of light scattered are then reported, and compared with related simulations and measurements reported in literature. Two particular approaches are then discussed with reference to their potential for thickness fluctuations evaluation, namely illumination with a grazing angle of incidence and light reflection. Last section deals with angular speckle correlation for light scattered by silica-on-silicon wafers, compare them with literature results, and deals with the particular case of speckle correlation in the presence of diffused fringes.

I Introduction

I.1 What is roughness

I.1.1 Defining roughness

This section explains what is usually referred to as roughness in surface measurement. The first part will introduce the different concepts necessary to understand surface topographic variations, differentiating them with their lateral dimensions. Then a mathematical description of relevant parameters in surface roughness measurement is provided for both two- and three-dimensional topographic data.

I.1.1.1 Terminology in surface height variations

The different aspects of surface quality are well summarized by the diagram of Figure 2 [Briers, 1993]:

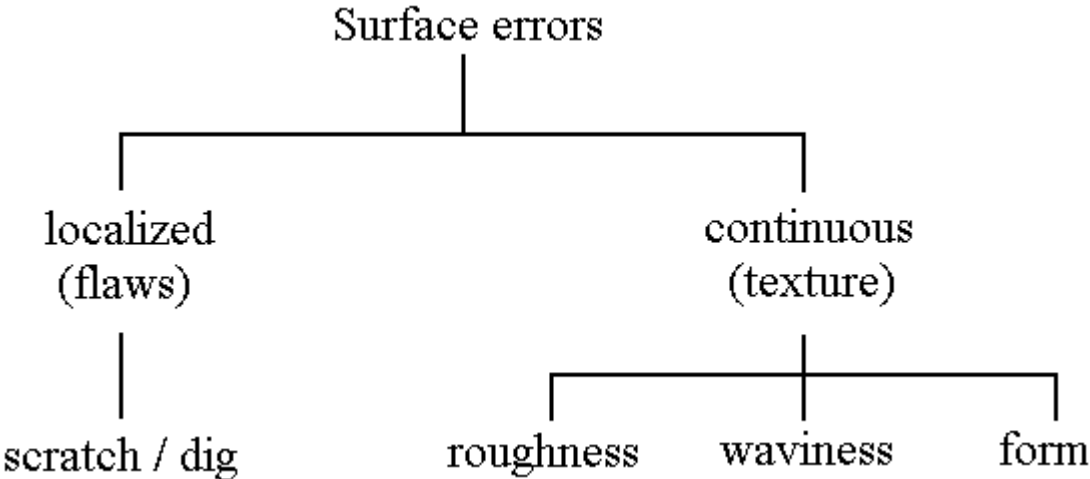


Figure 2: Classification of surface errors (reproduced and adapted from [Briers, 1993]).

Whereas scratches and digs constitute isolated defects, texture refers to the global appearance of the surface topographical features. Roughness, waviness, and form are related to the flatness of a surface, and consist in the deviations of the surface topography from planarity (or from the ideal surface shape for structured surfaces). Depending on the horizontal spacing between these deviations, roughness, waviness, and form are arbitrarily distinguished. Waviness is generally attributed to variations with horizontal spacings of the order of 1 to 10mm. Deviations in surface ideal shape with smaller spacings are referred to as roughness, while form is used to describe height variations on larger lateral scales.

Roughness is random by nature, either isotropic (with no direction privileged in structure) or anisotropic (which is generally the case for optical waveguide sidewalls for instance), and may originate from different processes. Its definition is consequently achieved in terms of

surface statistics. Roughness is generally characterized along two dimensions: vertically and horizontally. Among vertical parameters are the average height variations from the mean height and its root-mean-square equivalent. Among horizontal parameters is the power spectral density, which characterized roughness in terms of its spatial wavelength components.

Next section provides an overview of the mathematical parameters used to describe the roughness features in these two directions.

I.1.1.2 Mathematical description

Depending on the application aimed at, a surface can be described in a continuous or digitized way. One may thus characterize a surface using surface parameters (for a continuous surface) or parameter estimators (discrete surface). Because topographic data come out from measurements in the form of sampled values, the following presentation is restricted to parameter estimators in this section. They are first given for the case of two-dimensional profiles, and extended when possible to three-dimensional data.

- Vertical parameter estimators

The most widely used parameters to describe surface height variations in the vertical direction are the average and the root-mean-square height deviations. The average height deviation is defined as follows for the cases of 2D- and 3D-data:

$$Ra = \frac{1}{N} \sum_{i=1}^N |z_i| \quad \text{and} \quad Ra = \frac{1}{N_x N_y} \sum_{i=1}^{N_x} \sum_{j=1}^{N_y} |z_{ij}| \quad (1)$$

In these formulae, N ($N_x \times N_y$) is the number of points in the profile (or in the area respectively), and z_i (z_{ij}) are the height deviations with respect to surface mean line (shape). The root-mean-square roughness (RMS) is defined as follows for 2D- and 3D-data respectively:

$$Rq = \sqrt{\frac{1}{N} \sum_{i=1}^N z_i^2} \quad \text{and} \quad Rq = \sqrt{\frac{1}{N_x N_y} \sum_{i=1}^{N_x} \sum_{j=1}^{N_y} z_{ij}^2} \quad (2)$$

Although these two parameters provide useful information on the order of magnitude of the vertical roughness, it is noticeable that completely different surfaces may have the same average or RMS roughness. Refinement in the vertical roughness characterization may be performed using parameters such as skewness for instance. Skewness is defined as follows:

$$Skewness = \frac{1}{Rq^3} \frac{1}{N} \sum_{i=1}^N z_i^3 \quad \text{and} \quad Skewness = \frac{1}{Rq^3} \frac{1}{N_x N_y} \sum_{i=1}^{N_x} \sum_{j=1}^{N_y} z_{ij}^3 \quad (3)$$

According to [Briers, 1993], positive values indicate smooth surfaces with hills, whereas negative values generally account for the presence of holes. Other parameters may be employed for surface roughness description in the vertical direction, but will not be reviewed here. The other feature that may distinguish surfaces with similar Ra or Rq is their horizontal aspect. Next section describes the parameters used to take this feature into account.

- Horizontal parameter estimators

Two parameters are widely used for surface roughness characterization in horizontal direction: the auto-correlation function and the power spectral density. The auto-correlation function is estimated by the following formulae for the cases of two [Marx, 1990] and three dimensions respectively:

$$C(j\Delta) = \frac{1}{N} \sum_{k=1}^{N-j} z_k z_{k+j} \quad \text{and} \quad C(i\Delta_x, j\Delta_y) = \frac{1}{N_x N_y} \sum_{m=1}^{N_x-i} \sum_{n=1}^{N_y-j} z_{m,n} z_{m+i,n+j} \quad (4)$$

where Δ represents the sampling interval and N the number of points. The auto-correlation function describes with which confidence it is possible to know the height of a point, having the height of a first point. It is intuitive that for non-periodic surfaces, the correlation between two points decreases as the distance between them increases. The correlation length is usually defined as the distance for which the auto-correlation function reaches an arbitrary fraction of its maximal value (often $1/e$), and is representative of the horizontal variations of the surface profile.

The power spectral density (PSD) is estimated as follows for the cases of two [Vorburger, 2002] and three dimensions respectively:

$$PSD_{2D}\left(\frac{j}{N\Delta}\right) = \frac{\Delta}{N} \left| \sum_{k=1}^N z_k \exp(2\pi i j k / N) \right|^2 \quad \text{and}$$

$$PSD_{3D}\left(\frac{j_x}{N_x \Delta_x}, \frac{j_y}{N_y \Delta_y}\right) = \frac{\Delta_x \Delta_y}{N_x N_y} \left| \sum_{m=1}^{N_x} \sum_{n=1}^{N_y} z_{m,n} \exp\left[2\pi i \left(j_x \frac{m}{N_x} + j_y \frac{n}{N_y}\right)\right] \right|^2 \quad (5)$$

This function describes the surface variations in terms of spatial components, and thus provides us with the different lateral scales of roughness, and their contributions to the global RMS parameter.

It will be seen in next section how horizontal characteristics play a crucial role in the interpretation of roughness measurements.

I.1.2 Roughness and light scattering

Different values for the vertical and horizontal parameters characterizing roughness will have distinct behavior related to light scattering. As RMS values indicate departures from flatness, it is intuitively understood that the higher the value is, the higher the scattering phenomenon will be. However, it is noticeable that surfaces with the same RMS roughness can yet have completely different light scattering properties. This fact is illustrated in [Coursey, 2001] in terms of differences in horizontal scale of variation. For two surfaces having the same RMS roughness, the one with the more spaced peaks will produce more light scattering than the other one. This leads to higher light scattering for surfaces with longer correlation lengths.

The consequences of roughness towards light scattering are often seen in a negative way. Indeed, roughness is responsible for diffuse scattering when dealing with mirror-like surfaces, thus leading to power loss for various applications. As will be seen in last section of this chapter, waveguide sidewall roughness results in light scattering away from the waveguide, which is translated into transmission power loss when talking about optical communications. However, the presence of surface roughness has also been found to draw interesting positive consequences in the domain of molecular spectroscopy, leading to enhanced yield in Raman spectroscopy [Sánchez-Gil, 2002], infrared absorption [Domingo, 2003] and fluorescence [Kano, 1996].

The interest for quantitative surface measurement in light scattering studies is twofold. First, it helps comparing theoretical or numerical results to experimental data (see for instance [O'Donnell, 1987; Nieto-Vesperinas, 1990]), by providing adequate surface parameters to use in the former. Secondly, it enables comparing light scattering property induced by surface characteristics (see for instance [Knotts, 1992]).

After having described what is usually meant by surface roughness and underlined the interest in its measurement, next section reviews the different apparatus and techniques available for this purpose.

I.2 Measuring roughness

I.2.1 Instruments for surface roughness measurement

This section is a review of the techniques and set-ups available for roughness measurement. The review has been restricted to the methods potentially applicable to silica-on-silicon technology. This position imposes requirements on the scale of height variations that can be accessed (typically from 1nm to 1 μ m), and on the nature of the materials under investigation. The principles of operation of the methods reviewed are shortly explained. The advantages and results achievable are emphasized, as well as the limitations imposed by the different techniques.

The way of classifying the different approaches is somehow arbitrary. A possible solution, according to [Vorburger, 2002], is to consider profiling methods, area profiling methods, and area averaging methods. The first two methods record the surface profile respectively in two and three dimensions (probe methods for instance), and then deduce roughness parameters. Area averaging methods do not record surface profile, but provide statistical roughness parameters (angle-resolved light scattering for example). In our case, the different techniques are sorted out according to their general principle of operation. First, techniques based on the application of a probe on the surface are introduced. Methods employing an electron or an optical beam are then successively described.

I.2.1.1 Probe methods

In this chapter, measurement techniques based on the application of a probe on the sample under study are reviewed. An early instrument of this type is the now classical stylus profiler. More recent instruments are usually included in the term “scanning probe microscopy” (SPM). They appeared in the early 80’s with the invention of the Scanning Tunneling Microscope (STM), soon followed by the Atomic Force Microscope (AFM).

- **Stylus profilometer**

A stylus profilometer consists of a fine tip linearly scanned over the surface under study, or maintained fixed while the specimen is displaced below the tip. Gathering of successive scans provides 3D maps of the sample. Figure 3 illustrates the set-up of a stylus-based profilometer described in [Chi]. The tip is in direct contact at low force with the surface, and height variations are detected via a linear variable differential transducer (LVDT), which consists of a magnetic core in translation inside cylindrical coils.

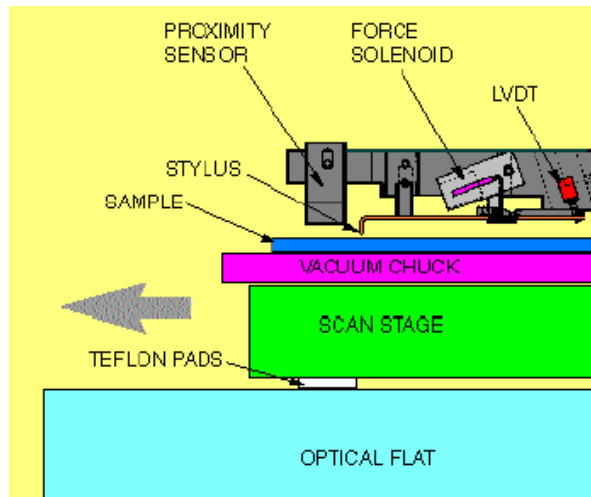


Figure 3: Example of stylus system (from Veeco documents).

An inherent drawback of the technique is that it may be destructive for relatively soft sample. The tip radius ranges from several tenth to a few microns, thus generally limiting the lateral resolution [O'Donnell, 1993]. However, vertical resolution can be as high as 0.5nm. On the other hand, one of the advantages of these instruments is their ability to resolve height steps up to 1mm. They can also produce large scans up to more than $10\text{mm} \times 10\text{mm}$. This later characteristic makes them appropriate for measuring flatness and waviness on entire wafers, that-is-to-say planarity fluctuations which lateral scales are greater than $100\mu\text{m}$ for instance, or for characterizing microelectromechanical systems [Chi].

- **Scanning tunneling microscope**

The scanning tunneling microscope [Binnig, 1982] consists in a very sharp tip scanned over a surface under study. The investigated sample being conductive, tunneling current can take place between the tip and the sample, provided the tip is close enough to the surface. Common working distances for the tip-sample tunnel interaction to occur is in the range of 10nm. By maintaining this tunneling current constant, it is possible to monitor height variations on the surface (another possibility is also to maintain the tip's height constant, and to deduce surface profile from current variations). Resolution can be as high as 0.1nm both in the vertical and lateral ranges. Figure 4 represents a schematic view of the scanning tunneling microscope.

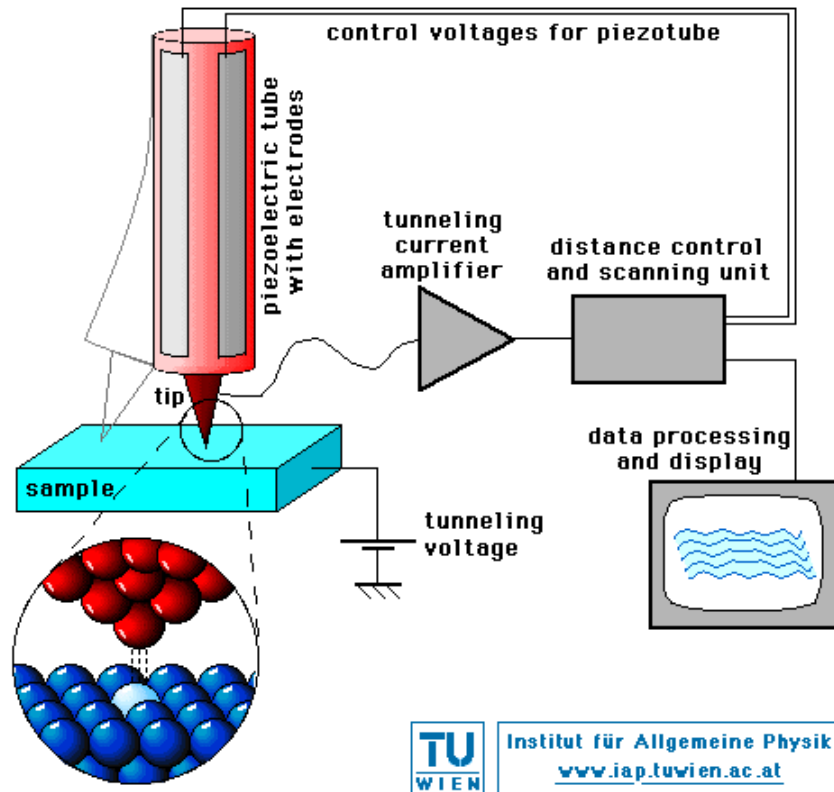


Figure 4: Schematic view of the scanning tunneling microscope.

However, an important requirement for the working of this microscope is that the sample has to be conductive, in order to tunneling current to take place. The atomic force microscope (AFM) was developed to overcome this limitation.

- **Atomic force microscope**

The AFM [Binnig, 1986] can accommodate both conductive and non-conductive samples. Contrarily to the STM, the interaction between the tip and the sample is not based on the tunneling current but on Van der Waals interatomic interaction force. The graph on Figure 5 (left part) represents the interatomic force as a function of sample-tip distance. Depending on this distance, three general working modes can be defined. In contact mode, the tip is only a few tenths of nanometer far from the surface, whereas in non-contact mode it is between 1nm and several tens of nanometer far. In both modes, by keeping the interaction force constant, surface topography is accessed via tip changes in position. The way these changes are monitored is illustrated on Figure 5 (right part). Another mode, usually referred to as *TappingMode*TM (patent Veeco) or intermittent-contact mode, consists in making the tip oscillating at the cantilever resonance frequency, and monitoring oscillation frequency deviations to address surface topography.

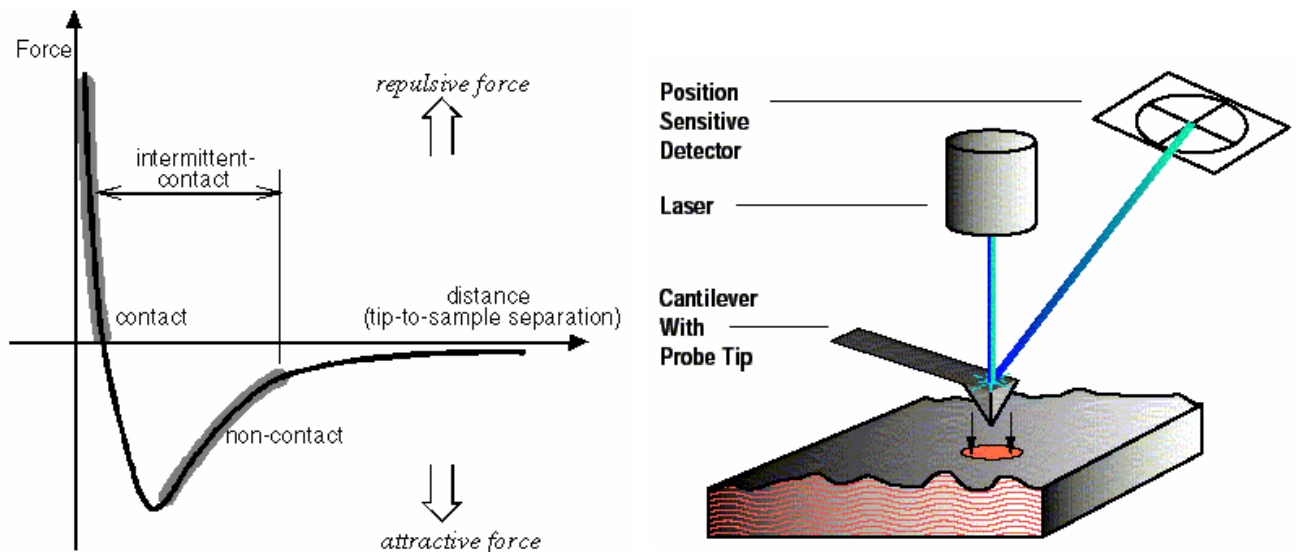


Figure 5: Interatomic force vs. distance curve (left), and principle of operation of the AFM (right).

Vertical resolution in contact mode is of the order of 0.5nm. Resolution is generally higher in contact mode, non-contact and intermittent-contact modes being employed with soft samples, where contact mode could cause sample damages. Lateral resolution is lower than the vertical one, and of the order of 2 to 10 nm. This arises because of the convolution between the tip shape and the surface profile to be measured. Two main disadvantages related to AFM are that, first, it can not accommodate surfaces with height variations higher than $10\mu\text{m}$, and, secondly, its lateral range of measurement is limited to approximately $100\mu\text{m} \times 100\mu\text{m}$.

I.2.1.2 Electron microscopy

The working principles of electron microscopy are briefly reminded, as well as the different elements usually composing electron microscopes, and the classification of these microscopes. After this introduction, much attention is paid to the very Scanning Electron Microscope, as this instrument is employed as a tool in the study reported here. Particularly, its structure is detailed, together with the ways of obtaining topographical information.

Imaging with electrons : working principles:

According to De Broglie relationship, a wavelength λ can be attributed to a moving electron and is defined as $\lambda = \frac{h}{mv}$, where h is Planck's constant, m the electron's mass and v its velocity. When the velocity of the electron is no more negligible with respect to the speed of light c , the relationship can be expressed in the relativistic domain as a function of the accelerating voltage V_{acc} applied to the electrons and results in Equation (6) [Colliex, 1998] :

$$\lambda = \frac{1.226 \cdot 10^{-9}}{\sqrt{V_{acc} + 0.9785 \cdot 10^{-6} V_{acc}^2}} \quad (6)$$

with λ expressed in meter and V_{acc} in Volt.

Numerical application leads to electron's wavelength with values in the picometer range. Table 1 illustrates the order of magnitude which can be expected.

V_{acc} (kV)	Wavelength (pm)	Typical application
1	38.8	Voltage used in this study
20	8.6	Voltage for SEM
100	3.7	Voltage for TEM
1000	0.87	Maximum voltage technically achieved

Table 1: Theoretical wavelength as a function of accelerating voltage.

Although theoretical resolutions are in the picometer range, practical resolution achieved are far from these theoretical limits. For instance, with an accelerating voltage of 1 kV, the resolution of the microscope employed in this study was of the order of 1nm. The source of this difference lies in the practical realization of the electron microscope itself, and the elements which compose it.

Electron microscope: working principle and configuration:

The working principle of an electron microscope is thus as follows. Electrons are first extracted from a source, then beam-shaped and accelerated. The resulting beam interacts with the sample under study. Finally, the desired information is collected with appropriate detectors.

Depending on the sample under study, several configuration may be adopted for the electron microscope. There are four classical combinations, depending on whether the instrument works in transmission or reflection and on whether it is designed with a scanning system or not. The choice towards a given configuration is governed by the nature of the sample under investigation and by the objectives aimed at. The most widespread versions are Transmission Electron Microscope (TEM) without scanning and the Scanning (reflection) Electron Microscope (SEM). As the instrument used in this a SEM, the following part of this section will be limited to this sort of instrument.

Fundamental elements composing scanning electron microscopes:

Two basic elements are first indispensable to electron microscopy: a vacuum system and a sample-holder. The presence of the former is a necessary condition to the required free propagation of electrons for imaging purposes. The latter enables positioning of the sample, what may imply translation, rotation, and tilt operations. The global structure of electron microscopes is usually split into two parts: the column area, containing electron sources and lenses, and the sample-holder area. In order to protect the column, the vacuum system is divided into two parts, one corresponding to the column that is kept permanently under vacuum, and one corresponding to the sample stage that is set to atmospheric conditions for interaction with users.

Three elements are now essential for obtaining an image within the SEM. First there is a need for an electron source. This element is generally realized using tungsten filament or tip, applying respectively high temperature (2500°C) or intense electrical field (1000V for a 200nm-diameter tungsten tip [Colliex, 1998]). The beam shaping is performed with electrical coils which play the role of magnetic lenses. Electrons are accelerated applying electrical potential differences along the column. Finally, after their interaction with the test sample, exiting electrons are collected using semiconductor detectors (for backscattered electrons) or an Everhart-Thornley (for secondary electrons). Figure 6 illustrates this detector configuration.

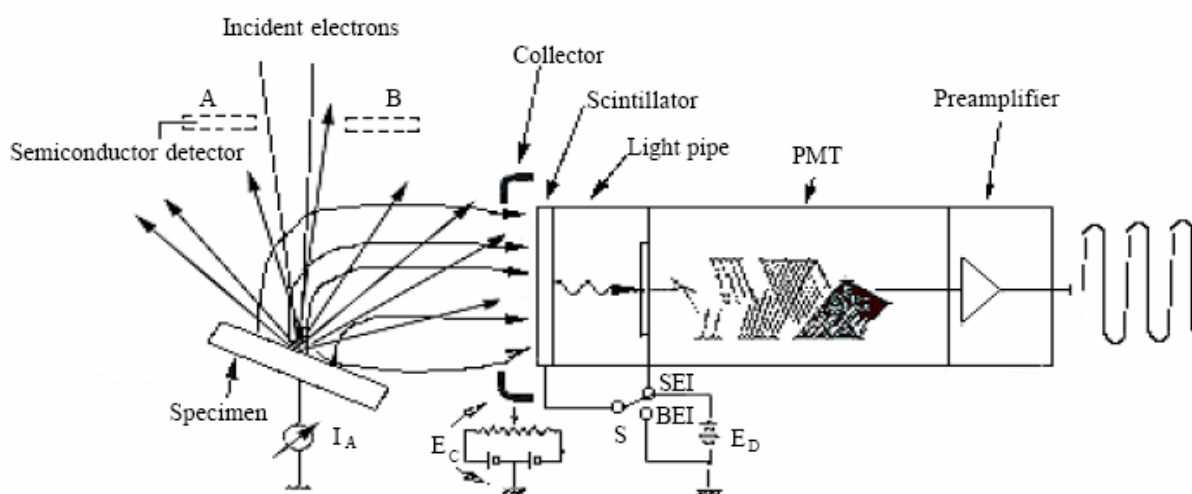


Figure 6: Schematics of secondary electron detectors (after JEOL documents).

Structure of SEM:

The distinct parts composing the apparatus are illustrated on Figure 7 (left part), and consist in a system for the application of a high voltage for providing electron acceleration, a magnetic lens for electron focusing, coils to perform the beam scanning over the surface, and electron detectors. Right part on Figure 7 represents the same schematics for the SEM used in this study.

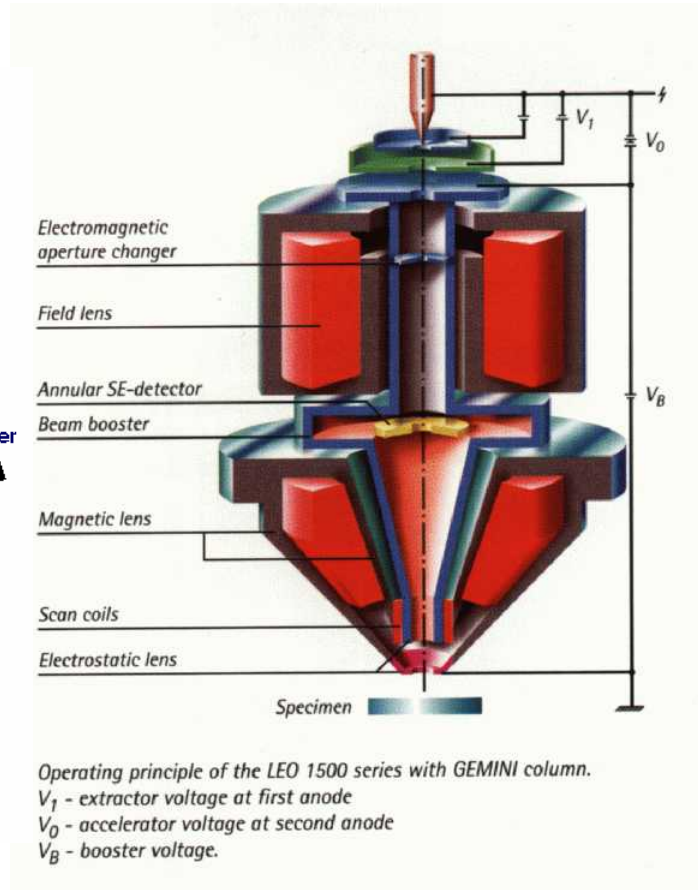
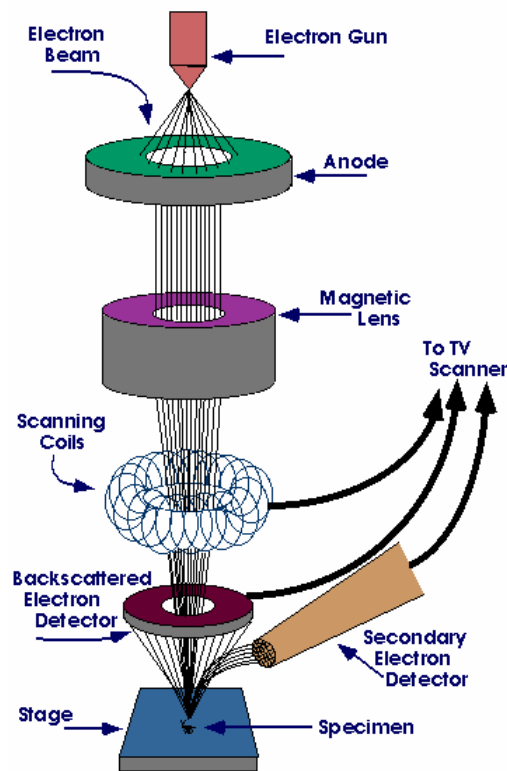


Figure 7: Components of SEM (left) and schematics of LEO GEMINI 1550 column (right).

Many signals may be detected within the SEM provided the use of adequate equipment. As far as surface roughness measurement is concerned, only topographical information is fully relevant. Two types of electrons can provide this information, secondary and backscattered electrons.

Secondary and backscattered electrons:

Secondary electrons (SE) are emitted by the sample with energies below 50eV, and come from the proximity of the specimen surface (a few nm). The SE yield is typically higher at low energy electron beam, thus leading to an operation of the microscope at low accelerating voltage. Because of their low energy, they can be deflected (and thus isolated) and then collected via a detector located on the side (cf. Figure 7). There is also the possibility to collect SE via an in-lens detector, where the collection efficiency is generally greater.

Backscattered electrons are electrons which are retroreflected from the surface with the a slightly lower energy than their incoming one (usually around 20 keV). They carry both topographical and compositional information. A combination of signals recorded at different angles of observation enables the separation of these two informations, and thus topography retrieval [Kaczmarek, 1998].

Spatial resolution with SEM using secondary electrons is of the order of a few nm, compared to a few tens of nm when working with backscattered electrons. This feature often influences the choice of working with secondary electrons when dealing with topography studies.

Topography information with secondary electrons:

Surface images obtained via secondary electrons carry intrinsically qualitative topographical information. As explained in [Joy, 1997], several factors contribute to this visual characteristic. First, the yield of secondary electrons depends on the angle that the impinging electron beam makes with the local surface normal, the yield being higher for illumination at large angles compared to surface normal. Secondly, the sample parts facing secondary electron detectors appear brighter than those opposite. Finally, edges are emphasized with bright lines, resulting from an higher secondary electron yield, because at edges the electrons can exit from two local surfaces.

Two operating factors influence the resolution when working with SEM : the working distance, or vertical position of the specimen, and the accelerating voltage. The higher the accelerating voltage is, the higher the spatial resolution. However, when increasing the accelerating voltage, charging effects can occur at the sample surface, resulting from the accumulation of electrons, and leading to image distortion or to the appearance of dazzling features. In order to avoid this charging, specimen surfaces are often coated with conductive materials like gold by sputtering for example, thus enabling surface electrons to evacuate. However , this coating may hide some topographical features of the sample and make the surface appear smoother than it really is.

However, SEM does not directly provide quantitative tri-dimensional topographic data, as was the case for AFM. Techniques thus have to be applied to retrieve relief data aiming at quantitative characterization of the surface.

Chapter 2 will be dedicated to the use of scanning electron microscopy for sidewall roughness measurement. Next section surveys existing optical techniques for surface topography inspection.

1.2.1.3 Optical methods

Methods based on the interaction of light with the sample all have one aspect in common: they are non-destructive. This feature has largely contributed to their popularity and several of them have been installed for in-line process control. This overview starts with imaging techniques, which includes classical optical microscopy, confocal microscopy, interferometry, and wavefront sensing. Statistical approaches are then reviewed, like those based on the study of surface scattered speckle properties, of angle-resolved scattered light, and on ellipsometry. Additional approaches are evoked for completeness.

- **Imaging techniques**

The first imaging technique that should appear in this review is the classical optical microscope. Although it lacks vertical information (as it is the case with electron microscopy) and has limited resolution, it remains familiar (in the way images are obtained) and convenient to use (generally no sample preparation). For these reasons, there is hardly a fabrication facility without optical microscope, for instance for default inspection. Here however, focus is given to three other optical imaging techniques, namely confocal microscopy, interferometric microscopy and wavefront sensing.

Confocal microscope:

A confocal microscope is composed of an illumination source, an optical microscope objective above the surface under study, and a receptor, generally a photomultiplier tube [Webb, 1996]. The idea behind confocal microscopy is to limit the light reaching the detector by inserting a pinhole in front of it. The role of the pinhole is to restrict the photons incoming onto the detector to those originating from a reduced area of the sample, thus reducing the depth of field of the initial optical microscope. Scanning as a function of vertical and lateral directions, this leads to the obtention of images as a function of height (or focus), which can then generate three-dimensional data. The schematics of Figure 8 illustrates this working principle.

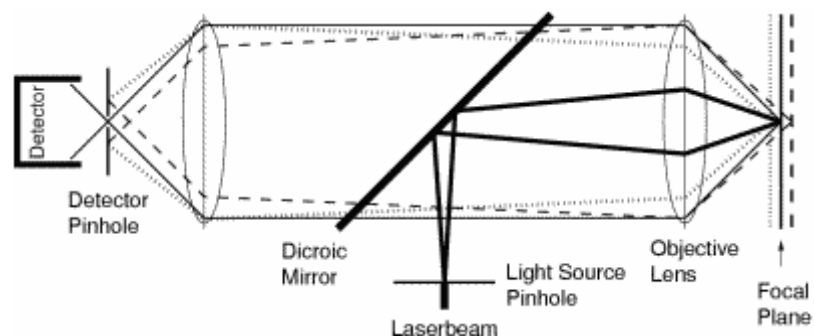


Figure 8: Working principle of a confocal microscope.

This type of microscope has found a wide range of application in the biological domain, where it can be used to image complex volumic features (a dichroic filter is then often used to discriminate fluorescent signal generated from the biological species). It can also be employed in surface metrology, the scanning enabling the detection of surface topography.

With the appropriate components (light source, optical objective, adequate pinhole), the vertical resolution of the instrument can be as low as a few nanometers, but its lateral one remains that of classical optical microscope. Consequently, it makes this instrument well adapted for waviness measurement. It presents the advantage of requiring no particular sample preparation, but may be slow due to the scanning process.

Interferometric microscopy:

The interferometric microscope [Aziz, 2000] uses the principles of light interference (see for instance [Born & Wolf, 2002]) to retrieve the topography of a test surface. For this purpose, a beam of light is split into two parts, one directed to a high quality reference surface and towards the surface under examination. Both surfaces are then imaged on a CCD camera, using a kind of optical objectives as illustrated on Figure 9.

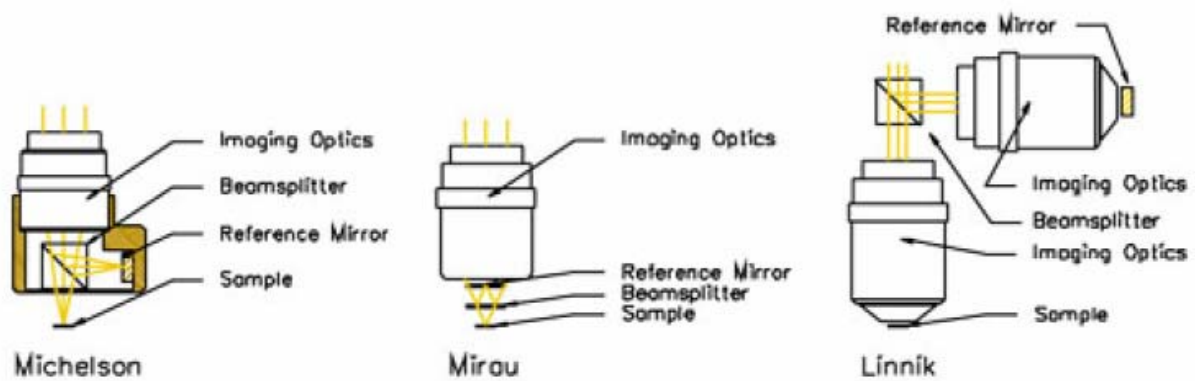


Figure 9: Different types of objectives settled in interferometric microscopes (from [Aziz, 2000]).

Assuming interference conditions are fulfilled, this results in an interference pattern (fringes) on the detector. Two different approaches may then be employed to retrieve topography [Benatmane, 2002]. Using a laser source as illumination, one may then vary incrementally either the test or reference surface, and then computes the topography (Phase Stepping Microscopy). The alternative is to make use of white light illumination to reduce the fringe envelope obtained when vertically scanning along surface's normal, thus making the maximum of this envelope a probe of surface topography (Coherence Probe Microscopy).

Vertical resolutions in the nanometer range are commonly achieved with this type of instrument. Lateral resolution remains however limited by the system {wavelength – objective} and is generally of the order of 400nm. These characteristics make this instrument well adapted to waviness measurement.

Wavefront sensor:

Wavefront sensors can provide a spatial phase map of a laser beam. When this laser beam is directed onto a surface under investigation, the reflected wavefront is affected by the surface topography. Wavefront sensors are based on the Shack-Hartmann wavefront sensor configuration described in [Platt, 2001], and briefly summarized here.

For analyzing the wavefront, the laser beam is passed through a lens array. Every lens focuses a fraction of the beam onto a CCD-detector array. Depending on the local wavefront tilt, the

position of the individual focus points varies. By monitoring these two-dimensional variations in position, the local wavefront slopes are retrieved. The global set of these slopes is then fitted to Zernike polynomials, in order to obtain the reconstructed wavefront. Figure 10 summarizes the principles of wavefront tilt acquisition.

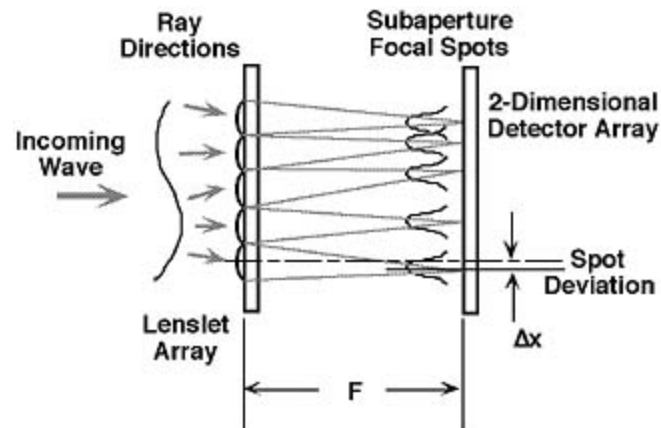


Figure 10: Principles of wavefront local tilts acquisition (from [Platt, 2001]).

The primary purpose of wavefront sensor is to assess beam shape of laser, but it has also applications in surface metrology [Forest, 2004]. Commercial devices can provide height resolution of the order of a few nanometers, with sub-millimeter lateral resolution. Due to these characteristics, the Shack-Hartmann wavefront sensor is more adapted to flatness measurement than to roughness measurement, and can be used for example to control the planarity of Si wafers.

- **Statistical techniques**

The previous techniques perform a surface topography reconstruction before estimating its parameters. Assuming given height variations statistics for modeling, the following techniques then estimates surface parameters from measured light features. Among such techniques, this section highlights speckle techniques, light scattering and ellipsometric measurements.

Speckle:

Speckle is the name given to the granular appearance of light reflected from surfaces. It arises from interferences between light diffused at points on the surface having different heights [Goodman, 1984]. A good overview of surface roughness measurement using laser speckle phenomenon is provided in [Briers, 1993]. There are two major categories of approaches to surface roughness measurement using the optical speckle phenomenon [Hun, 2002].

The first one consists in recording an image of the speckle pattern produced by the surface, and to use its image characteristics (contrast, mean speckle size, form,...) to deduce surface roughness. These methods are usually valid for roughness magnitude below the wavelength of the illumination source.

When the order of magnitude of surface roughness overcomes this limit, the speckle pattern is said to be fully developed, and its image characteristics can not be directly related to surface roughness parameters. There comes the second class of roughness measurement based on

correlation calculations between patterns obtained with different wavelengths or illumination angles [Léger, 1975].

Additional speckle-based techniques assess the properties of speckle patterns scattered by surfaces under speckle illumination [Lehmann, 1999], or can make use of speckle pattern interferometry [Leopold, 1997], achieving sensitivity respectively in the nanometer and micrometer domains.

Speckle-based techniques may thus assess surfaces within different roughness amplitude ranges. They have however two major drawbacks. First, they do not provide directly with an absolute roughness value. Consequently, the preliminary realization of a calibration curve linking speckle-related values and roughness parameters is mandatory. The second drawback is the difficulty to retrieve surface correlation length from speckle-based method. This is one of the motivation for the development of techniques relying on measurement of light scattered by the surface.

Light scattering:

There are basically two steps in light scattering-based techniques aiming at roughness measurement. The first step is to illuminate the surface and to record light that it scatters. Two principal configurations are commonly adopted for this purpose: angle-resolved light intensity measurement in the plane of incidence [Marx, 1990; Takakura, 1996] and integration of the whole light scattered by the surface under study [Duparré, 2002]. The second step consists in modeling the surface illuminated [Ogilvy, 1991], calculating its scattering distribution, and matching this numerical estimation to the corresponding experimental light intensity measurement.

Measurement of roughness amplitude as low as a few nanometers have been reported on reflective surfaces. An advantage of the approach is its ability to take into account the correlation length of the surface while modeling and thus to retrieve it when matching numerical and experimental data sets. A relative drawback is the difficulty to measure surface roughness with amplitude approaching the illumination wavelength [Vorburger, 1993].

Ellipsometry:

Ellipsometry consists in analyzing the polarization of light reflected from the surface under study when illuminating with oblique incidence. Illuminating the surface with a linearly polarized incident laser beam, the analysis is performed when looking at the ratio of light reflected with p and s polarization. A model of the sample material then enables linking these parameters with sample parameters. There exist several configurations for the practical realization of ellipsometers, the main ones being described in [Azzam, 1987]. When adding one or several transparent (for the wavelength considered) layers over the initial reflecting surface, the previous analysis need be performed at several wavelength to compensate the increase in the number of unknowns to be determined, leading to so-called spectroscopic ellipsometry.

The initial purpose of ellipsometry is to retrieve thickness and refractive index for the addressed system, surface roughness being more a limiting factor to the technique than a quantity to assess. However, taking it into account within material model enables the extraction of the equivalent of a roughness layer, which may lead to amplitude values. A limiting factor of ellipsometry is thus its model dependence, both for roughness measurement

and layers' parameters retrieval. An interesting application still in development is yet the determination of surface and interface roughness for silica-on-silicon sample using angle-resolved ellipsometry [Germer, 2000].

For the sake of completeness, two additional statistical optical methods may be cited, namely surface second harmonic generation [Dadap, 1994] and infrared spectroscopy [Ishikawa, 1999]. They have both been shown to be sensitive to SiO₂/Si interface roughness and to be potential candidates to this inspection for thin (10nm-thick) silica layers.

1.2.2 Comparison between instruments

It is often tempting, for calibration or comparison purposes, to carry out measurement on the same sample with two different instruments. When comparing the results, the vertical resolution difference may play a key role, but it is also important to consider the bandwidths (in terms of spatial frequencies) of both instruments. The upper spatial frequency limit is defined by the lateral resolution of the device, whereas the lower one results from the length of the scan for profiling systems for instance. Basically, profile comparisons should be made only where the bandwidths overlap. Instruments with similar vertical resolution may give very distinct RMS value if operating over different spatial frequencies [Vorburger, 2002].

Such a comparative study has sometimes been carried out (see for instance [Duparré, 2002]) with instruments based on different operating principles like AFM, confocal microscope and angle-resolved scattering. Direct RMS values coming from different instruments show high dispersion. Although the agreement between these values is greatly improved when paying attention to the spatial bandwidth of the instruments, perfect agreement remains utopic and some discrepancies are generally persistent. This is partly due to the nature of the surface (like the presence isolated particles [Duparré, 2002]) which reacts differently as a function of the testing instrument, but also partly to external factors linked to measurement itself (uncertainty, errors and calibration) and its procedures (experimental environment, user). A good illustration of this point is the case of measurement reproducibility tests carried out with a common set of test samples over different laboratories using the same type of instrument. Even for the case of a well known and widely commercialized technique such as interferometric microscopy [Briers, 1999], the inter-laboratory dispersion of the measurement remains non-negligible.

As a conclusion to this chapter's section on roughness measure, one may remember that there is a wide choice of various instruments having different characteristics related to working principle, resolution, range of measurement and of application. The challenge in surface metrology is consequently to find the right instrument to a given problem. When one can ideally chose (without financial or practical considerations) among any of the instrument already cited, it is essential to know what are the material to be studied (metal, silica,...), its geometrical arrangement (plane, curved, spherical, cylindrical, sidewall surface,...) and its range of surface topography variations (nanometer, micrometer range).

Next section describes the materials to be used for the studies reported in chapter 2 and 3 of this thesis.

1.3 Silica-on-silicon optical waveguides

Several methods have been developed for the fabrication of silica on silicon optical waveguides. The most widely used procedure consists in the deposition of different refractive index silica layers on a silicon substrate, followed by the etching of these layers for the definition of waveguide structures. An introduction to the different fabrication techniques can be found in [Ladouceur, 1996].

Most of industrial deposition set-ups make use of either Chemical Vapor Deposition [Gorecki, 2000] or Flame Hydrolysis Deposition (FHD) [Kawashi, 1990; Ruano, 2000]. In this section, we will concentrate on the method of fabrication employed for the realization of the samples addressed in this work, that-is-to-say FHD combined with reactive ion etching (RIE) for waveguide formation [Bazylenko, 1996b, McLaughlin, 1998]. Some applications derived from this technology are then given as examples, aiming at integrated optics, but also other recent fields of development. Finally, the presence of roughness in these physical systems is introduced, as well as its induced consequences.

1.3.1 Materials and fabrication

The first step in the fabrication process consists in the generation of a thermal oxide on top of the silicon wafer, its thickness varying from a few hundreds of nm to several μm depending on system design. The purpose for such an oxide formation is twofold: it facilitates the adhesion of further deposited silica layers, and can also serve as a buffer layer to prevent leakage from the wave guiding structure into the silicon substrate [Ladouceur, 1996]. The role of the buffer is often realized via a first silica (SiO_2) layer deposited by FHD. The core layer is then deposited by FHD, but with different gas composition mix to achieve a material of higher refractive index than the buffer layer. Typical doping material for FHD process consists in GeO_2 , B_2O_3 , P_2O_5 , with the refractive index being defined by the relative concentration of the gases. The soot composing the FHD layers are sintered in an adapted furnace for solidification.

The etching of the waveguides is performed via several successive steps, including: mask sputtering (generally Chromium, or Silicium) over the core silica layer, followed by photoresist coating, UV patterning of resist layer, and then successive ion etching of the mask and core silica layer. The remaining photoresist and mask material are then chemically removed.

Finally, the etched structures are covered by a cladding layer, also deposited by FHD, of which the refractive index matches the one of the buffer layer. Figure 11 summarizes this fabrication procedure.

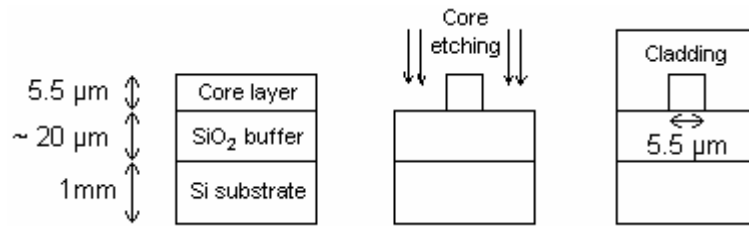


Figure 11: The three basic steps for silica optical waveguide fabrication.

I.3.2 Applications

Due to the boom in optical telecommunications demand in the late 90's, passive optical components using the fabrication techniques previously described have been widely developed. An exhaustive list of all the devices would exceed the frame of this thesis, suffice maybe to mention the Arrayed Waveguide Grating as an example [Smit, 1988]. This device proved well adapted for wavelength multiplexing and demultiplexing, and is now widely implemented in Dense Wavelength Division Multiplexing schemes for optical telecommunications.

More recently, there has been increasing attention dedicated to the application of the fabrication method to the realization of devices for biological and chemical purposes. Such devices can for instance combine micro-sized channels for fluid and light guiding [McLaughlin, 1998; Ruano, 2000 and 2003; Friis, 2001] on the same chip, thus enabling analyzing the interaction of light and fluid, as in fluorescence or light scattering schemes.

I.3.3 Roughness formation

Roughness can appear at different steps along the fabrication process. Surface roughness measurements on silicon wafers have a rather long history, with AFM and angle-resolved light scattering approaches being the most popular techniques, due to their application to metrology in the semiconductor industry. The influence of oxidation techniques and parameters on roughness formation for the case of thin (up to a few hundreds of nm) Si oxide layers is addressed in [Zúñiga-Segundo, 1994]. However at this step, roughness is generally small (up to a few nm), and its consequences in integrated optics application are usually neglected. Roughness can then be generated during the successive FHD of silica layers. Although the air-silica interface is commonly inspected using an AFM, interface roughness between buried silica layers or the substrate can also be assessed, via ellipsometric [Germer, 2000] or interferometric [Perrot, 1995] approaches.

The more critical step yet for roughness formation lies in the silica etching process. This step generally results in the formation of anisotropic roughness onto the waveguide sidewall. Figure 12 illustrates this resulting waveguide sidewall state for two devices investigated during this study.

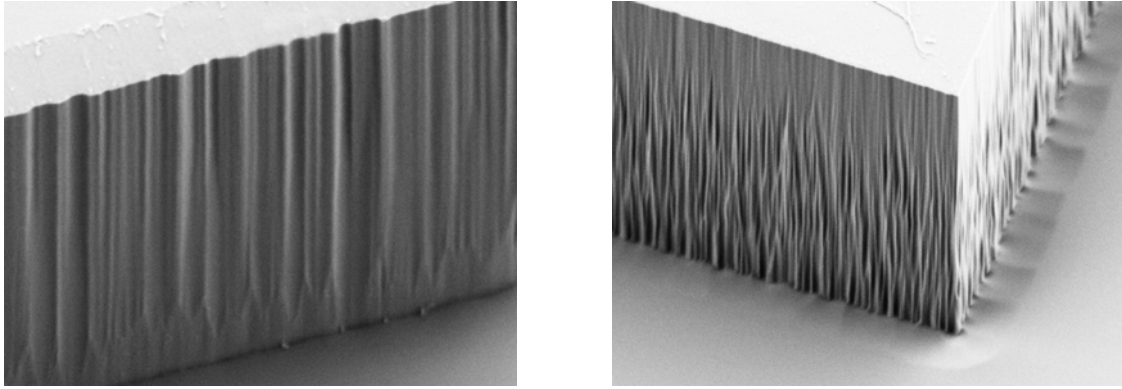


Figure 12 : SEM-images of waveguide sidewall showing evidence of roughness

The origin of sidewall roughness has been experimentally studied [Ladouceur, 1994], including the influence of etching parameters on resulting roughness and waveguide dimensions [Bazylenko, 1996b]. A lot of theoretical work has been carried out to characterize the consequences of waveguide sidewall roughness in terms of optical loss generation [Lacey, 1990; Ladouceur, 1994 & 1997; Rodríguez, 1999; Elson, 2001]. An experimental study was also conducted measuring optical loss for waveguides having sidewall with different quantitative roughness [Bazylenko, 1996a]. Its consequences on the behavior of complete integrated devices has also been studied [Goh, 1997] for the case of an arrayed waveguide grating. The influence of sidewall roughness in microfluidics is not as well characterized, mainly due to the young character of this technology. However, recent studies highlight roughness-induced consequences on flow propagation in microchannels [Hu, 2003].

The quantitative measurement of silica sidewall roughness can thus have significant importance for process refinement in the fabrication of integrated optical devices with expected performances. It may also lead to better understanding of device behavior when performing modeling. Available techniques for measuring sidewall roughness will consequently be reviewed in section 2.1. Sections 2.2 and 2.3 will present two SEM-based approaches for quantitative sidewall roughness measurement of silica waveguide on full wafer.

II SEM-based waveguide sidewall roughness measurement

II.1 State of the art of available techniques for sidewall roughness measurement

As already mentioned, the challenge with roughness measurement consists in finding the right instrument, in terms of resolution and spatial frequency bandwidth, to match the feature scale of the sample to be assessed. In the case of waveguide sidewall roughness, the topography variations lie in the nanometric range, both in vertical and lateral directions. In addition to the dimension requirements, access and materials constraints limit the possibilities to mainly three instruments, namely the Scanning Tunneling Microscope (STM), the Atomic Force Microscope (AFM), and the Scanning Electron Microscope (SEM).

Although STM is well adapted for roughness measurement of flat conductive samples, it has also been used to measure sidewall roughness [Sato, 1991], using a so-called “branched tip” which consists in a pair of tips to access both the vertical and horizontal dimensions. In addition to the use of a special tip, the apparatus requires the sample under study to be conductive, which may be a rather severe constraint.

Sidewall roughness on silica waveguides can also be studied with AFM, and three different approaches have been developed so far. The first one considers the sidewall roughness to be mainly constituted by vertical striations coming from the etching process, and originating in the transfer of the mask edge irregularities into the resist. The roughness being assumed to be one-dimensional along the propagation direction, and provided that the height of the structure of the study can be accessed by the AFM, measurements of contour lines of the mask [Ladouceur, 1992], and of the etched waveguide [Ladouceur, 1994] are performed from the top side, thus enabling prediction of the transmission losses of the device. The two other approaches intend to directly image the waveguide sidewalls. One possibility is similar to the technique adopted with STM, that-is-to-say the use of a special tip, coupled with a non-standard servo-control system, to provide information also in the horizontal direction [Nyyssonen, 1991; Martin, 1994]. This technique has been turned into a purposely dedicated commercial instrument [Veeco, 2003], and its tip geometry is illustrated on Figure 13, with arrows denoting the directions where height information is collected.

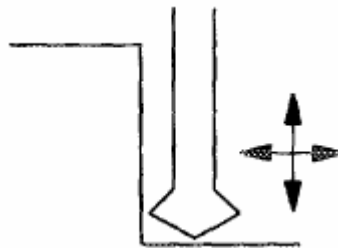


Figure 13: AFM tip geometry for sidewall inspection (from [Nyyssonen, 1991]).

Finally, measurement of sidewall roughness for Si micromirrors has already been performed by tilting the sample under study within the AFM, and used for process refinement [Juan,

1996], or by using samples specially designed to facilitate the access of the AFM tip [Jang, 2003], and a study of the influence of the angle between the AFM tip and the sidewall has been reported [Reynolds, 1999]. Figure 14 illustrates these measurements with samples having around 100nm (a) and 30nm (b) vertical RMS roughness respectively.

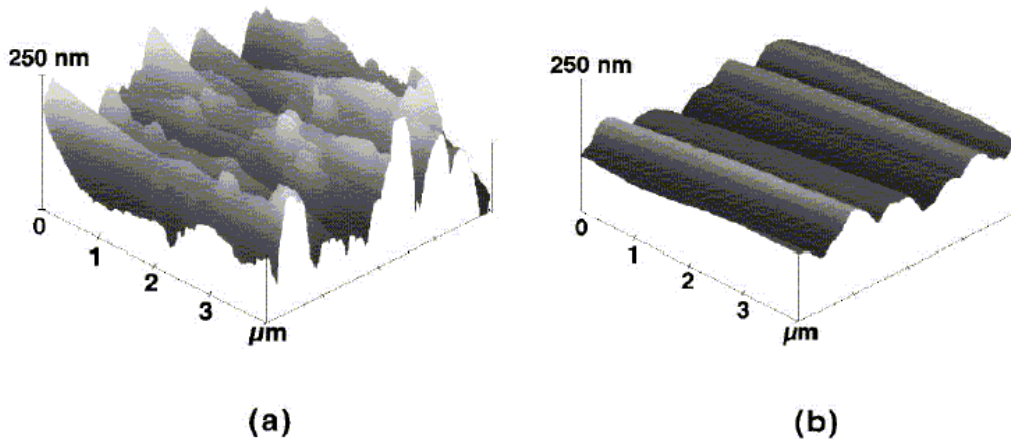


Figure 14: Si sidewall imaged by AFM (from [Juan, 1996]).

The drawbacks with the last two techniques using the AFM is that they require either a purposely-designed tip coupled with a non-standard control system, or the preparation (cut and tilt) of the wafer. Indeed, as detailed in [Reynolds, 1999], using the AFM tip in a configuration other than perpendicular to the sidewall leads to different surface representation and roughness parameters.

Due to its relative ease of use and to the quality of its image contrast, SEM has been used in qualitative waveguide sidewall roughness inspection [Bazylenko, 1996a and 1996b], by direct imaging of the waveguide sidewall. The major drawback when using SEM for roughness assessment, is the lack of quantitative values when imaging the waveguide sidewall for instance, SEM providing only dimensional data on lateral directions. A way to overcome this limitation consists in imaging the waveguide from the top, and in measuring the corrugations appearing on the waveguide's edges due to the presence of sidewall roughness, technique known as Line Edge Roughness (LER) measurement [Reynolds, 1999; Nelson, 1999]. However, this technique can not provide information on the evolution of roughness going from the top to the bottom of the waveguide sidewall. Using a SEM with 4 secondary electron detectors set facing each other, sidewall roughness measurements were reported [Matsutani, 1995], but the technique requires a non-standard SEM and the sidewall to be perpendicular to the electron beam. On the other hand, two family of techniques have already been applied to retrieve topography from arbitrary SEM image, namely those based on stereoscopy [Piazzesi, 1973; Stampfl, 1996] and those on shape-from-shading algorithms [Zhang, 1999]. Stereoscopy uses images of the same physical area recorded under different angles of view or with several detectors, and, after matching the corresponding physical areas in the images [Stampfl, 1996], computes topographical variations from feature shifts between the images [Piazzesi, 1973]. On the other way, shape-from-shading algorithms enable topography retrieval from contrast information present in the image.

The objective of the work is to investigate the potential of Scanning Electron Microscopy for quantitative waveguide sidewall roughness inspection. An additional constraint lies in the conditions of inspection, which is expected to be on full wafer without sample treatment. This requirement has to be understood as a necessary (but not sufficient) condition for further application for in-line inspection. The following strategy was adopted. Wide spread use of SEM for qualitative evaluation of etching quality is first illustrated, together with common LER measurement procedure. Secondly, the application of stereoscopy to the problem of waveguide sidewall roughness quantitative evaluation is investigated. A third section explains the implementation of a shape-from-shading algorithm to test the validity of the approach. The two approaches are then compared and discussed in the context of competing techniques for industrial waveguide sidewall inspection.

II.2 Visual inspection and Line-Edge Roughness measurement

In this section, wide spread uses of SEM for waveguide sidewall inspection are reviewed.

LEO SEM:

The images in this study were recorded using a LEO Gemini 1550 scanning electron microscope. The general working principles of a SEM have been given in chapter 1, and the parameters influencing resolution. For the understanding of this section, no precise knowledge of this very microscope are required, but two points should be kept in mind. This instrument has a resolution of 2.1nm at 1kV operating voltage, and enables sample imaging without requiring preliminary coating.

Description of the reference sample:

The test sample assessed in this study was fabricated by FHD of a buffer and core silica layers on top of a thermally oxidized silicon wafer. The core layer was 5.5 μm -high, and etched by standard RIE process. Figure 15 shows an overview of the topography from a waveguide sidewall.

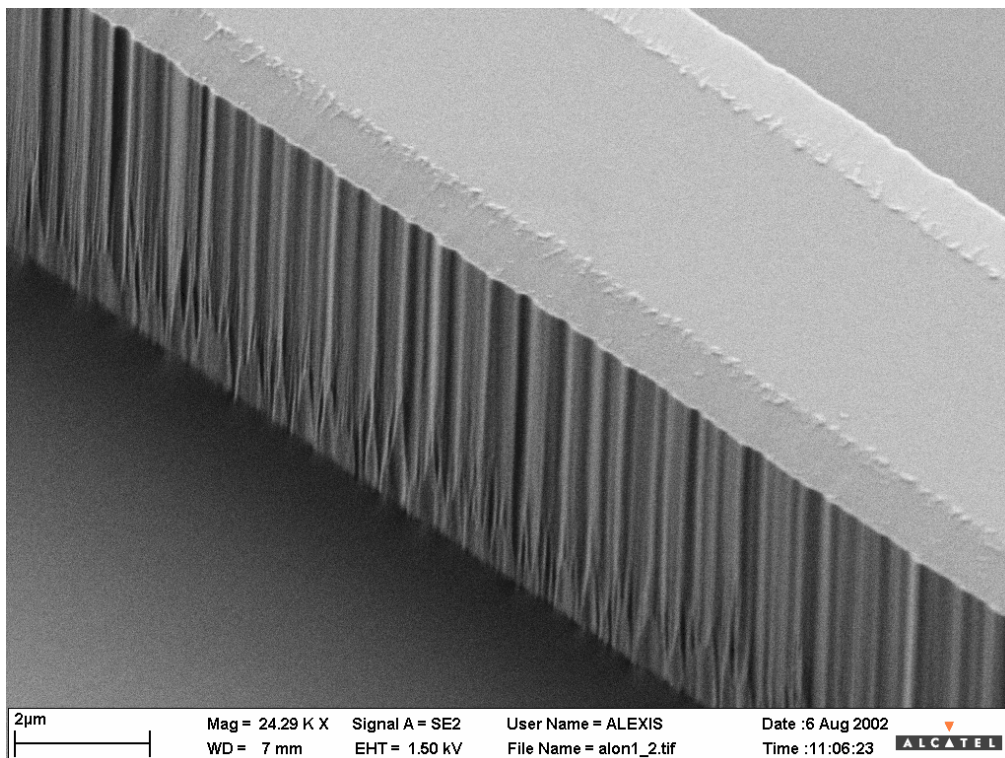


Figure 15: Overview of waveguide sidewall topography on test sample.

II.2.1 Sidewall quality assessment via visual inspection

Quality assessment via visual inspection consists in imaging waveguide sidewall as depicted on Figure 15.

The technique is still frequently used in literature for fabrication study to assess the etching quality of a given process, or even to compare different etching processes or conditions. It is yet certain that this procedure remain largely user subjective, and consequently subject to discussion. However, there are two cases where the approach is interesting : when the roughness magnitudes to be compared are clearly distinguishable and when the form of roughness produced on the sidewall differs from one case to another. Two examples from samples fabricated by Alcatel SEL AG are given to illustrate this point, which may be compared with sample displayed on Figure 16.

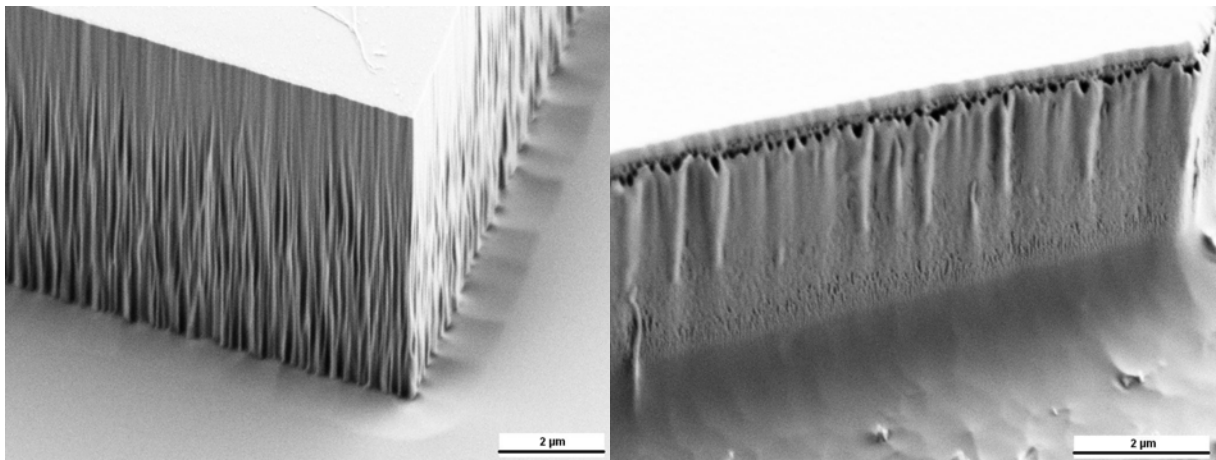


Figure 16: Two examples of sidewall roughness aspect.

The technique (cf. Figure 17), coupled with top-down imaging, has been used to study the influence of sidewall roughness on propagation loss [Bazylenko, 1996a].

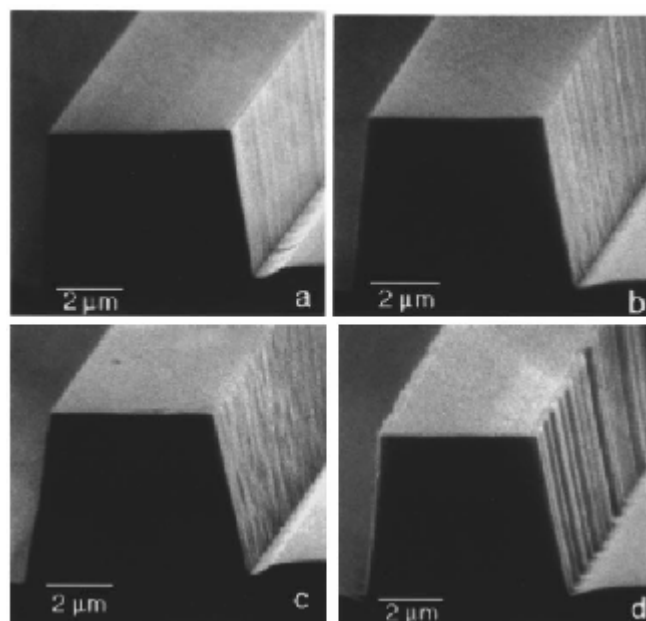


Figure 17: Etched sidewalls compared in [BAZYLENKO, 1996a].

The authors reached the conclusion that an increase in sidewall roughness amplitude of 50nm could lead to a propagation loss increase of 0.2dB/cm. The samples were silica-on-silicon wafers, with weak index confinement, namely the refractive index difference between core and cladding/buffer layers was below 0.01 around 1.46 at a wavelength of 633nm. The core size was 5 μ m x 6 μ m. All these parameters are close to those for our samples. Consequently, this result can be considered an interesting order of magnitude to fix the ideas.

A similar study was internally carried out [Heid, 2003]. Samples coming from different fabrication processes were compared. However, it was not possible to draw any conclusion on the very influence of roughness, for two reasons. First, the roughness amplitudes being qualitatively of the same order of magnitude, comparison was not easy. Secondly, such a sample comparison requires all other parameters such as sidewall angle, waveguide width, layer composition and thickness, remaining constant. Indeed, these parameters also influence propagation losses. This point had already been emphasized in [Bazylenko, 1996a], but is not always easy to achieve experimentally.

The preceding remarks point out the importance of quantitative roughness comparison. Next section details a common procedure in industrial labs to obtain quantitative values for waveguide edge variation measurement.

II.2.2 Line-Edge Roughness measurement

In its initial position, the wafer is perpendicular to the electron beam, and one may image the waveguide from its top, in a so-called top-down configuration. The resulting image presents corrugations on the edges of the waveguide, which originate from the presence of sidewall roughness as depicted on Figure 18.

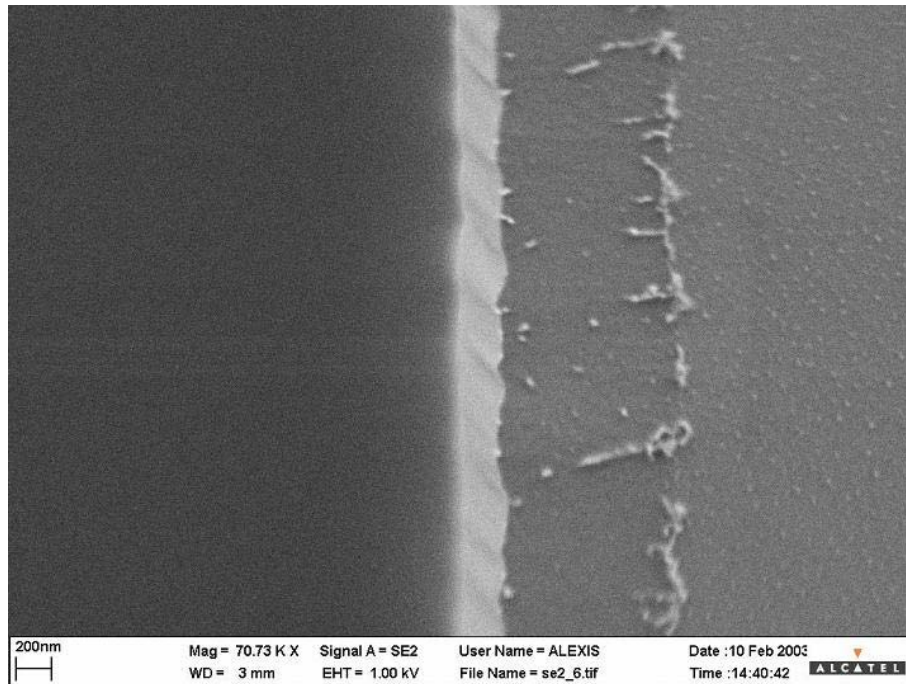


Figure 18: Typical SEM image for LER measurement.

The bright lines are attributed to electron emission by the waveguide sidewalls. In our case, the sidewalls have been observed not to be strictly at 90° with respect to the waveguide top surface, but rather to form an angle around 87° with it. The sidewalls having their normal at 87° with respect to the electron gun direction, their secondary electron emission yield is strongly higher than the one of the other elements (electron yield proportional to $1/\cos$), thus making them brighter. Consequently, the inner edge position variations can be assimilated to height variations on the top part of the sidewall. Particular imaging conditions for LER measurement include short working distance (3mm), high magnification ($\approx 70,000$ times), and moderate operating voltage ($\leq 1\text{kV}$) to avoid charging effects on the sidewalls. Great care is required concerning imaging conditions, because they can dramatically affect quantitative estimated values. Among the parameters of importance are the SEM operating voltage, scan mode [Reynolds, 1999], and stigmation settings [Nelson, 1999].

Once the images have been recorded, an algorithm step is required to identify and locate the edge points, this step being often coupled with contrast enhancement and noise reduction processing [Solecky, 1999]. We adopted the procedure described by Reynolds and Taylor [Reynolds, 1999]. The top-down images are filtered using for instance a Sobel filter within AnalySIS software in order to enhance the edges' visibility, and the edges are then detected under MATLAB (The Math Works, Inc.) software. A linear regression is applied to the detected edge points to avoid any undesirable tilt of the mean edge line. RMS roughness and peak-to-peak variations can thus be retrieved.

The preceding procedure is now illustrated on the reference sample used in this study. Let us start with a SEM image recorded in the conditions previously mentioned. This image is represented on the left part of Figure 19. This image is then processed with a digital Sobel filter to enhance its edges, as illustrated on the right part of Figure 19.

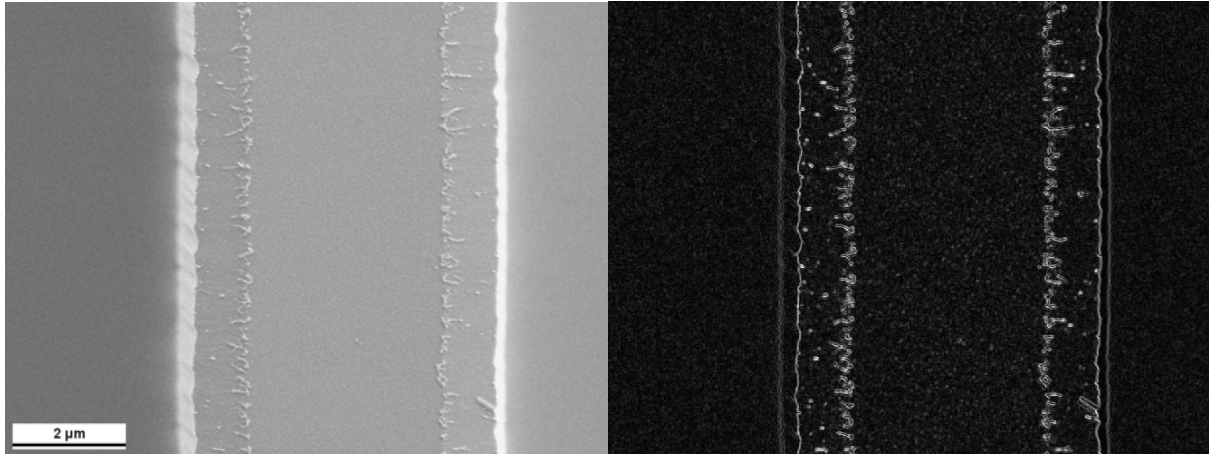


Figure 19: Initial SEM (left) and Sobel-filtered (right) images

Sobel-filtered images are converted to .bmp files, color inverted, manually cleaned points not corresponding to edge points, then converted again into monochrome binary ((0,1) files). Finally, the edge profile is detected under MATLAB software. Figure 20 shows the thresholded image and the corresponding extracted profile.

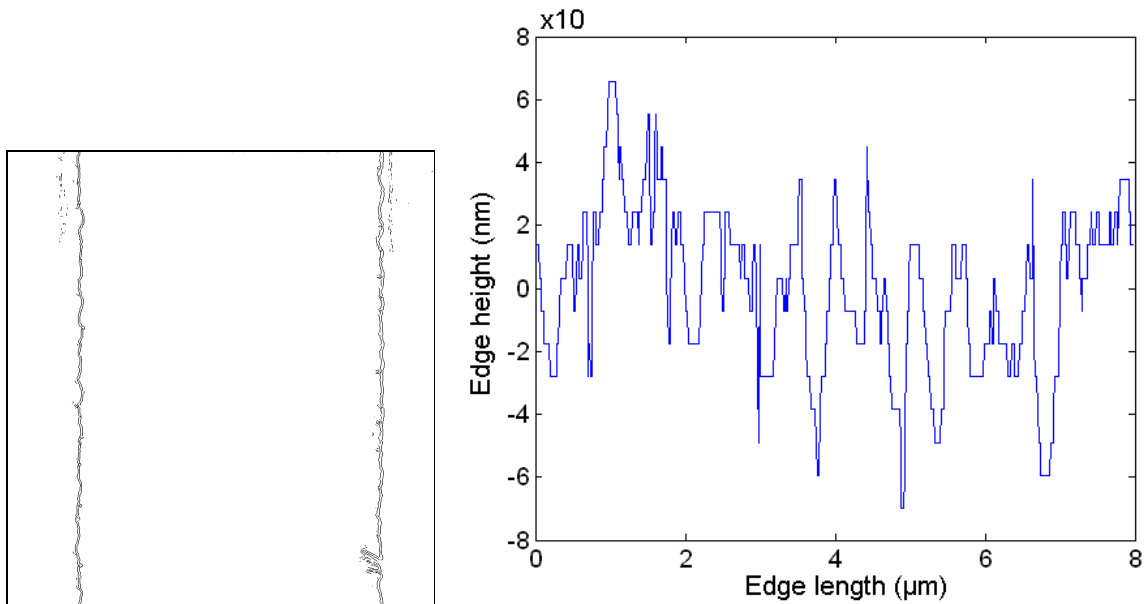


Figure 20: Thresholded image (left) and extracted profile (right).

Calculations on the extracted profiles of Figure 20 lead to a peak-to-peak value of 135nm, and an RMS value of 25nm. Figure 21 shows the auto-correlation function of the LER extracted profile displayed on Figure 20 (right part).

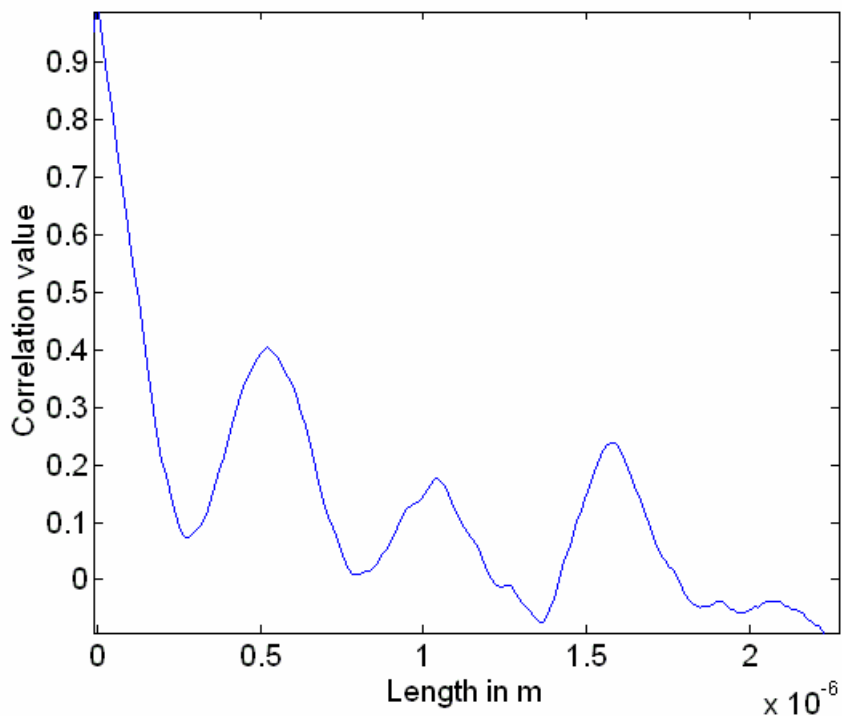


Figure 21: Auto-correlation for LER-extracted profile.

A major limitation of the technique is that it can not assess sidewall roughness as a function of height position on the sidewall. On $5\mu\text{m}$ -high silica waveguide, roughness can change both in magnitude or in form on the sidewall. Next two sections are thus attempts to retrieve sidewall roughness as a function of position on the sidewall.

II.3 Stereoscopic approach

This section begins with a theoretical description of the procedure adopted for measurement. Classical stereoscopy within the SEM is first modeled, and then extended to the study of waveguide sidewall. Practical implementation is described, comprising both image pair recording and pattern matching steps. Some results are then presented and commented, showing the potential, but also the limits of the approach.

II.3.1 Theoretical description of the procedure

To describe the moves undergone by the stage within the SEM, the formalism of algebraic rotation matrices is employed. The matrix for a rotation of angle θ around z is written as follows in the (x,y,z) base:

$$R_z(\theta) = \begin{bmatrix} \cos \theta & -\sin \theta & 0 \\ \sin \theta & \cos \theta & 0 \\ 0 & 0 & 1 \end{bmatrix}_{x,y,z} \quad (7)$$

A main hypothesis governs the forthcoming mathematical descriptions: the object under study being described in the (x,y,z) space, it is assumed that the image formed within the SEM is a projection of the (x,y) plane onto a plane orthogonal to z -axis located above the sample. Such a projection is called a parallel (or orthographic) projection, and differs from the image formation mechanism inside the SEM, which is a central projection. Exact formulae are derived in [Piazzesi, 1973]. However, at high magnification, the image formation can be assimilated to a parallel projection [Horn, 1986, cf. p. 21]. As the study of roughness involves very high magnification, the images recorded in our case lie within this context.

II.3.1.1 Classical stereoscopy within the SEM

The method we propose is an extension from classical stereoscopy. Therefore, classical stereoscopy is first reminded. In its initial position (for full wafer inspection, without any tilt angle), the geometry of the SEM is defined on Figure 22. The plane of view is the (x,y) plane. To gain height information, two tilts of the sample have to be symmetrically performed around y -axis. Figure 22 defines the plane of view (of projection) inside the SEM (left part), and illustrates the two tilts around y -axis (center and right parts).

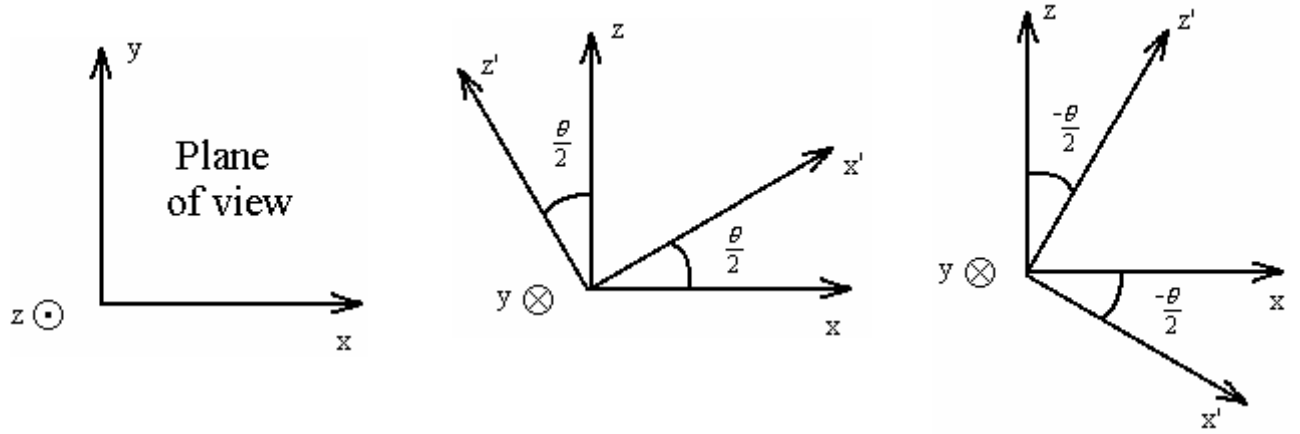


Figure 22: SEM plane of view (left), symmetrical tilts around y-axis.

The application of the first rotation to a point M of coordinates (x,y,z) is mathematically represented as follows, and transforms the point M into $M1$:

$$M1 = R_y\left(\frac{\theta}{2}\right)M = \begin{bmatrix} \cos\frac{\theta}{2} & 0 & -\sin\frac{\theta}{2} \\ 0 & 1 & 0 \\ \sin\frac{\theta}{2} & 0 & \cos\frac{\theta}{2} \end{bmatrix} \begin{bmatrix} x \\ y \\ z \end{bmatrix} = \begin{bmatrix} x \cos\frac{\theta}{2} - z \sin\frac{\theta}{2} \\ y \\ x \sin\frac{\theta}{2} + z \cos\frac{\theta}{2} \end{bmatrix} \quad (8)$$

Operating now a second rotation of opposite angle as depicted on Figure 22 leads to a point $M2$ such that:

$$M2 = R_y\left(-\frac{\theta}{2}\right)M = \begin{bmatrix} x \cos\frac{\theta}{2} + z \sin\frac{\theta}{2} \\ y \\ -x \sin\frac{\theta}{2} + z \cos\frac{\theta}{2} \end{bmatrix} \quad (9)$$

On the two images, only coordinates on x - and y -axis are available. Subtracting term by term the coordinates of the two points, we observe that there is no shift along y -direction, and that the x -shift can be expressed as follows:

$$X_{M2} - X_{M1} = 2z \sin\frac{\theta}{2} \quad (10)$$

This formula is also obtained in [Piazzesi, 1973] for the case of high magnification. The height z of M can thus be deduced from the x -shift between the stereoscopic image pair. The evaluation of waveguide sidewall surface roughness in this configuration would require the sidewall surface to be orthogonal to the electron beam. This involves the cut of the wafer containing the waveguides of interest. Moreover, only one waveguide can be accessed, the others being hidden behind the upper one.

II.3.1.2 Stereoscopy for waveguide sidewall inspection

For optimal imaging of the waveguide sidewall when dealing with full wafers, the sample within the SEM is tilted by 45° , following the description of Figure 23.

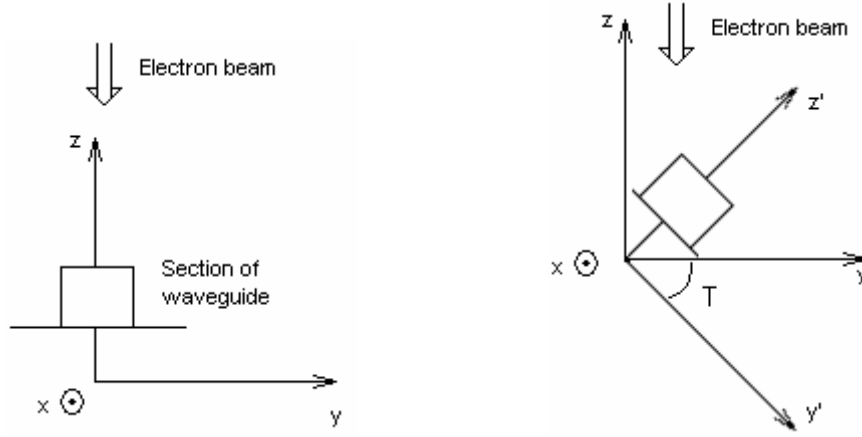


Figure 23: Non-tilted (left) and tilted (right) sample configuration for optimal sidewall imaging.

This operation is described by a rotation of angle T around x -axis, resulting in a matrix similar to Eq. (7). When the sample has been tilted for better observation of the features of interest, a pair of images is recorded on the same physical area, by performing two symmetrical rotations around the normal of the sample. The rotation axis in this case is referred to as z' on Figure 23. $A=(x,y,z)$ constitutes the reference base. The rotation matrix around z' is expressed in the base $B=(x,y',z')$ as

$$R_{z'}^B(R) = \begin{bmatrix} \cos R & -\sin R & 0 \\ \sin R & \cos R & 0 \\ 0 & 0 & 1 \end{bmatrix}_{x,y',z'} \quad (11)$$

In order to mathematically apply this rotation to the previously mentioned tilt, this rotation has to be expressed in the base A . This new matrix is given by the relation:

$$R_{z'}^A = C_B^A R_{z'}^B C_A^B \quad (12)$$

where C_A^B represents the transfer matrix from base A to base B . The columns of this matrix are base A vectors expressed as a function of base B vectors. Consequently, in our case :

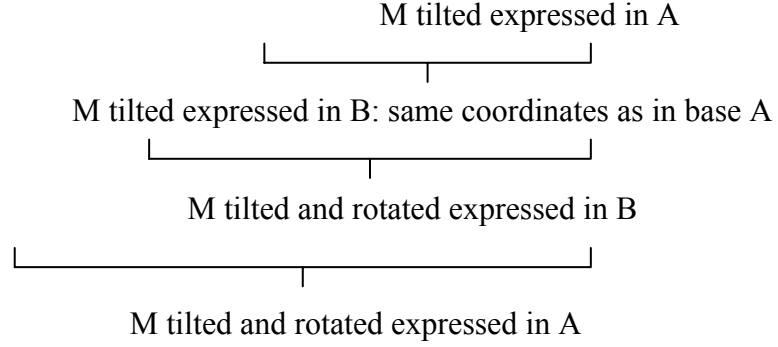
$$C_A^B = R_x(T)^{-1} \quad \text{and} \quad C_B^A = R_x(T) \quad (13)$$

For any point M of coordinates (x,y,z) in base A , the combination of the tilt and rotation operations is equal to :

$$M1 = R_{Z'}^A R_X(T) M \quad (14)$$

This expression can thus be developed into:

$$M1 = R_X(T) R_{Z'}^B(R) R_X(T)^{-1} \underbrace{R_X(T) M}_{\text{M tilted expressed in A}} \quad (15)$$



Calculating the $R_X(T)R_{Z'}^B(R)$, we obtain Equation (16) :

$$R_X(T)R_{Z'}^B(R) = \begin{bmatrix} 1 & 0 & 0 \\ 0 & \cos T & -\sin T \\ 0 & \sin T & \cos T \end{bmatrix} \begin{bmatrix} \cos R & -\sin R & 0 \\ \sin R & \cos R & 0 \\ 0 & 0 & 1 \end{bmatrix} = \begin{bmatrix} \cos R & -\sin R & 0 \\ \cos T \sin R & \cos T \cos R & -\sin T \\ \sin T \sin R & \sin T \cos R & \cos T \end{bmatrix}$$

Calculating now the x -shift that would result in two stereo images recorded by two symmetrical rotations around the sample normal by angles R and $-R$, we obtain:

$$X_{M2} - X_{M1} = 2y \sin R \quad (17)$$

It has to be noticed that in the case of sidewall roughness investigation, the height of the waveguide being along z -direction, sidewall roughness is accessed via data along y -direction. Consequently, recording a stereo image pair according to the described procedure does provide sidewall topographical information, without the need to correct them by any geometrical factor. The major drawback however is the induced y -shift, shift that is not present in classical stereoscopy described in section II.3.1.1. This shift is equal to $-2x \cos T \sin R$, and changes thus along x -direction.

II.3.2 Practical implementation

The practical implementation of the theoretical procedure described consists in two main steps: recording the stereo image pair of a given physical area, then computing its associated surface profile.

II.3.2.1 Image pair recording within the SEM

A stereoscopic image pair is defined as two images of the same physical part of a sample, but recorded under two different angles of view. The two means for obtaining such a difference with the SEM are to tilt the sample (without tilt, the sample is orthogonal to the incident electron beam) and to rotate it (the axis of rotation is always orthogonal to the sample surface). The procedure described in previous section is applied to obtain the stereo image pair, i.e. initial tilt of 45° to image the sidewall followed by two symmetrical rotations around tilted sample's normal.

The images used for stereoscopic reconstruction are typically recorded at 1.5kV operating voltage, with magnification of the order of 40,000 times. At these high magnifications, it is necessary to accurately adjust magnification and stigmatism settings to obtain optimal resolution [Nelson, 1999]. Although the apparatus is equipped with a compucentric set-up for stereoscopic image pair recording, the precision of this feature could not match the requirements imposed by the magnification employed. Consequently, a manual position correction was performed after the sample moves to image the same waveguide sidewall area. Figure 24 shows an example of two stereo images of the same area obtained after rotation around the normal of the sample.

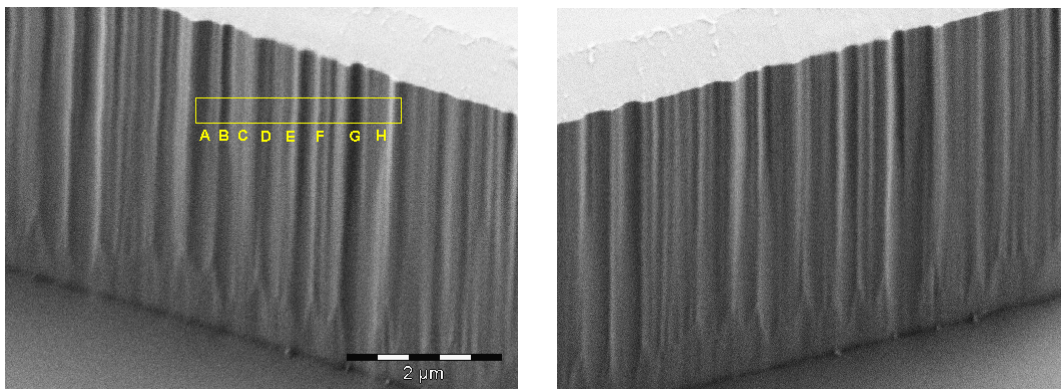


Figure 24: Two stereoscopic images of the same waveguide sidewall area.

The stereo angle for the case of Figure 24 is 40° , which corresponds to two symmetrical rotations of angle $R = 20^\circ$ around sample normal.

II.3.2.2 Stereo profile estimation software

The stereoscopic reconstruction calculations were performed with the so-called AnalySiS software from Soft Imaging System GmbH, via the "stereo" module. The software enables preliminary image scale matching, and requires an user-based verification for stereoscopic image matching.

Principles of topography estimation:

To match the corresponding physical areas, the program calculates a correlation coefficient between two given equal-sized portions of the reference image and search images. It then calculates the same coefficient for different portions on the search image. Two images are considered to correspond to the same physical area where the maximum correlation coefficient is found.

Once corresponding points on the two stereo pictures have been identified, it calculates the height profile of the surface using formula (10).

Reconstruction parameters:

Before performing the reconstruction, several parameters have to be defined for the software. The first of them is the stereo angle. Then, the dimensions of the reference pattern (pattern-width and pattern-height), i.e. the element in the reference image that the software will try to match with its equivalent part in the search image, are selected. It is also necessary to define the area ("max X-shift" and "max Y-shift") in the search image wherein the reference pattern should be matched. This area depends on the amplitude of the lateral shifts between the two stereoscopic images, and should be large enough to cover the biggest point shift. Figure 25 illustrates these parameters.

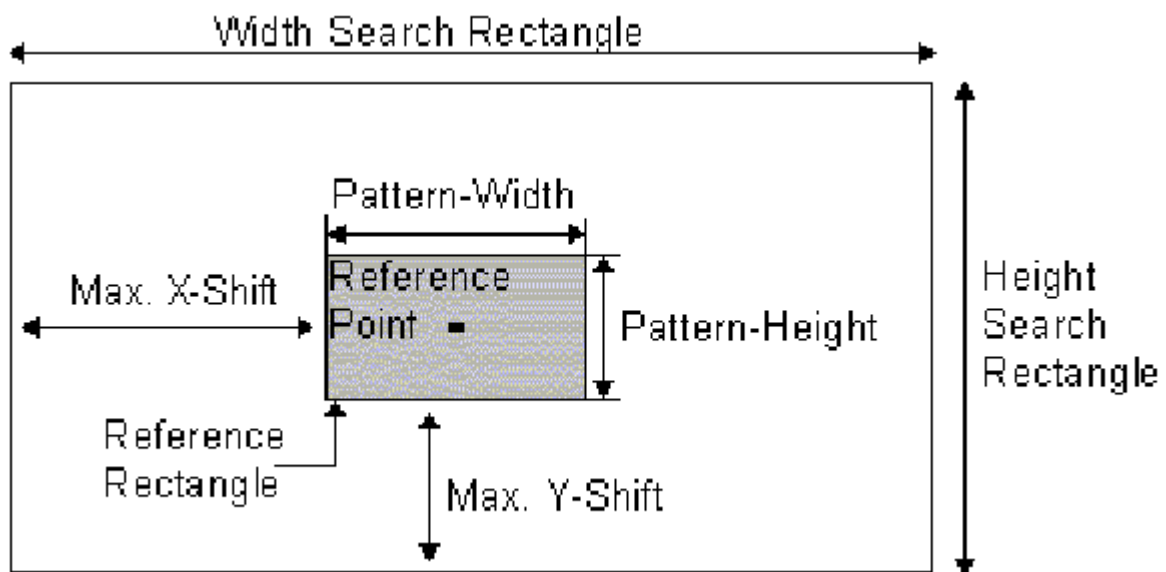


Figure 25: Definition of the reconstruction parameters

Finally, the user has to define the so-called "step width X" and "step width Y" parameters. They determine the steps to sample image pixels for profile calculations, in x - and y -directions respectively.

Influence of reconstruction parameters:

Max. X-Shift: This parameter is of crucial importance, since the calculated height comes from x -shift calculations between the two stereo images. Due to the order of magnitude of sidewall height variations, stereo-induced x -shifts remain low. The area wherein the shifted pixels are looked for is a rectangle of dimensions fixed by Pattern-Width and Pattern-Height parameters, and enlarged by "Max. X-Shift" in x -direction and by Max. Y-Shift in y -direction. In our case, the initial rectangle defined by the "Pattern" parameters already contains the searched pixels in x -direction. The lowest possible value for "Max. X-Shift" was therefore chosen, i.e. 5 pixels.

Max. Y-Shift: As height data are calculated according to X-shift, and due to the geometry of the features of interest (vertical lines), a huge increase in this parameter generally does not affect the reconstructed profile. Moreover, to take into account the stereo-induced y -shift generated by our imaging procedure, high values for this parameters are necessary. Values above 80 were used for the results presented here.

Pattern-Width and Pattern-Height: These two parameters play a symmetrical role, defining the pattern to be matched in the two images. An increase in these parameters leads to clearly fewer unwanted noisy peaks. This is probably because the correlation for pattern matching is performed on a higher number of pixels, thus reducing error appearances (isolated peaks). However, a too high value for this parameter leads to longer computation time and to visibly too soft surface profile (the criterion for such an estimation is the comparison with the profile of the reference single image, cf. Section II.3.3.2).

Treatment parameters:

Three post-reconstruction treatments are available. To each point of which the height is estimated is attributed a correlation parameter between 0 and 1. This parameter evaluates the degree of confidence with which the point is identified in the two images. There is no systematic link between this degree of correlation and the quality of the reconstructed profile. For instance, for small stereo angles ($\sim 0.5^\circ$), the correlation is globally excellent, but the angle not large enough for the profile to be reasonably reconstructed. Low correlation may also arise from reference patterns distorted during the tilt of the sample, because the points that compose it are of different height. The treatment based on the correlation parameter consists in neglecting the points of which the correlation is below a user-defined threshold, and to approximate them by an average performed with their closest neighbors. When using large stereo angles (40°), the resulting matching correlation coefficient can be relatively low (0.1). Consequently, the averaging filter triggered with respect to a given correlation threshold was not used.

The second treatment available is called "clipping", and consists in truncating points with heights largely outside the range of mean heights. This treatment is well adapted in case some feature heights are over-estimated, whereas they could not be identified visually on the SEM image, and was found useful to slightly smoothen profiles containing punctual artifact peaks.

However, too important clipping parameters simply do not render correctly surface profiles. The clipping parameters generally used in our cases were (1.5,1.5) (cf. AnalySiS Software documentation).

Finally, there is also a smoothing filter for height profile available, based on clipping of image pixel gray values (whereas the previous filter was based on height filtering).

Consequently, the correlation filter and the height smoother were generally found to degrade profile details, because of the spatial averaging they operate, and were therefore not used. The clipping filter was cautiously used to re-size over-estimated peaks (according to the initial images) to the same order of magnitude as their surrounding.

II.3.3 Results

II.3.3.1 Example of reconstructed profile

Profile reconstruction:

The two images of Figure 24 are used for profile reconstruction. The selected area for topography retrieval is highlighted by a rectangle on Figure 26 (left part). Letters A-H were added after calculations to match the corresponding areas on the reconstructed profile represented on Figure 26 (right part).

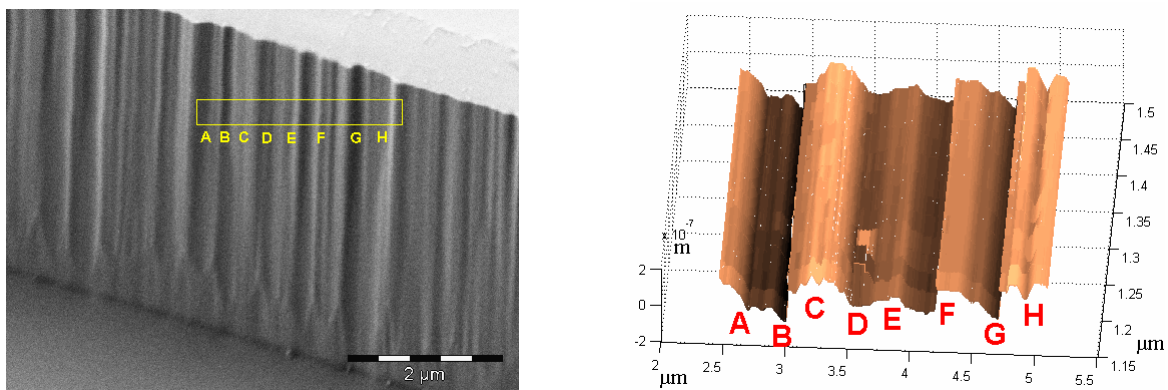


Figure 26: Reference SEM image with rectangle selected for topography calculation and corresponding reconstructed waveguide sidewall profile.

Data correction: Replacing R by $R+\alpha$ and $-R$ by $-R+\alpha$ in expression (16), it is possible to take into account misalignment of the waveguide sidewall with respect to the x -axis of the resulting SEM image. Indeed, this misalignment is equivalent to a rotation of angle α around z' -axis superimposed on the two symmetrical rotations of angles R and $-R$. Using trigonometric simplification identities, formula (17) thus becomes

$$h = \frac{X_{M2} - X_{M1}}{2 \sin(R)} = x \sin(\alpha) + y \cos(\alpha) \quad (18)$$

This formula proves particularly useful to correct small (below 1°) unwanted rotation around z' -axis that would result in tilted reconstructed sidewall profiles.

Resolution: Formula (10) can be rewritten as follows:

$$h = \frac{X_{SH} \cdot X_{SC}}{2 \sin\left(\frac{\theta}{2}\right)} \quad (19)$$

where X_{sh} corresponds to the number of pixels representing the point shift between the two stereoscopic images, X_{sc} stands for the scale of the image along x -axis, h is the height of the point considered, and θ the stereo angle. θ is physically strictly comprised between 0 and 180°. For a given image scale along x -axis, the height resolution is obtained by the height calculated for a shift by one pixel. Thus, the greater θ is, the greater the denominator in the formula and the smaller the height step that can be evaluated, and consequently the higher the vertical resolution is. Typical resolutions when imaging waveguide sidewalls at magnifications of the order of 40,000 for stereo angles of 20° and 40° are around 20nm and 10nm respectively.

However, due to the geometry of this stereoscopy-like procedure, the greater the stereo angle, the larger the feature shift in y -direction between the two stereo images.

II.3.3.2 Consistency of the reconstructed profile

Two techniques were applied to check the validity of the reconstructed profile. First, it is qualitatively compared with the initial SEM image. Secondly, quantitative values obtained from calculations are compared with LER measurements.

Comparison with the SEM initial image

The letters present on Figure 26 match the corresponding areas in the initial SEM image and the stereo-reconstructed profile. As it can be visually noticed, the profile is in good agreement with the topography that can be induced from the original contrast of the initial SEM image.

Comparison with Line Edge Roughness measurements:

Quantitative values obtained via the stereoscopic procedure are compared with values coming from LER measurements described in section II.2.2. The parameters selected for quantitative comparison are the peak-to-peak amplitude of the sidewall variations, which corresponds to the maximum height difference on the two profiles, and the RMS standard deviations (RMS roughness) of the profile data (along x -direction for the stereo profile).

The roughness parameters extracted via both techniques were compared on the same physical areas, and averaged over several locations on the waveguide. Although the same features were qualitatively observed in the top-down image and the estimated profile, noticeable discrepancies were found between quantitative height maps. Namely, the stereo approach tends to overestimate roughness amplitude in comparison with values coming from LER. RMS roughness values of 40 and 60nm were found respectively for LER and stereo procedures, with peak-to-peak height of 120 and 200nm. Table 2 summarizes these results.

	LER	Stereoscopy
Peak-to-peak amplitude	120nm	200nm
RMS roughness	40nm	60-65nm

Table 2: LER and Stereoscopic values for sidewall profile parameters.

These discrepancies may come from software feature mismatching when identifying the corresponding physical areas on the stereo image pair. Indeed, the resolution previously stated has to be understood as the minimal feature size detectable, which would result in a shift of one pixel between the two stereo images. However, a more subtle point is that any pixel mismatch when identifying a given physical area on two stereo pictures would result in a height overestimation of the same quantity (i.e. 10nm), multiplied by the number of pixels, and may lead to dramatic height differences between the stereo and LER procedures. The feature matching step, being already not an easy task due to the relative absence of clearly identifiable patterns, is still more difficult due to the use of large stereo angles. The challenge lies in finding adequate trade-off between high stereo angle (thus high vertical resolution) and acceptable pattern matching error. Further improvement in the pattern matching step could certainly enhance the agreement between values coming from LER and stereo procedures, the consistency between initial SEM image and reconstructed profile (cf. Figure 26) constituting an encouraging result.

In addition to RMS and peak-to-peak values, other parameters, such as correlation length and fractal dimension, are frequently employed for roughness characterization [Constantoudis, 2003], taking into account lateral aspects of roughness. Fourier spectrum and auto-correlation functions along x -direction of stereo-reconstructed profile both indicated that, in addition to high spatial frequency roughness, the waveguide surface present longer-scale topography variation. Figure 27 shows the estimated auto-correlation function for stereo-reconstructed profile.

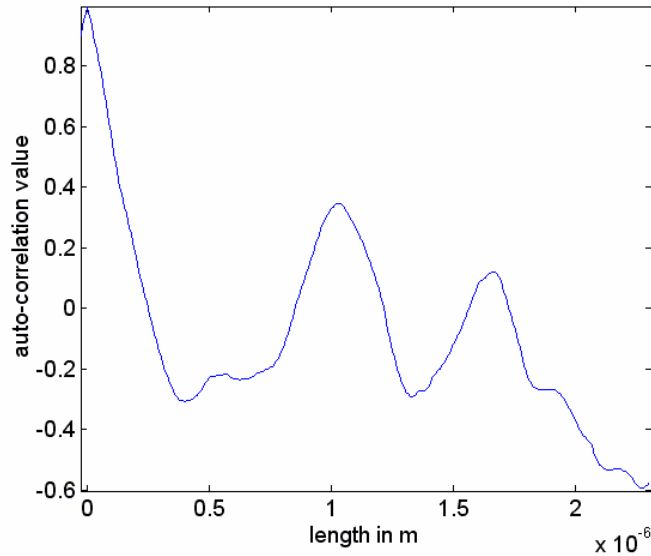


Figure 27: Auto-correlation along x -direction for sidewall stereo-reconstructed profile.

This feature appears in the auto-correlation function curve as a broad peak around $1\mu\text{m}$. LER analysis confirms the existence of this low-frequency quasiperiodicity, as it can be seen on Figure 21.

II.3.4 Conclusion on stereoscopic approach

An adaptation of stereoscopy for waveguide sidewall profile reconstruction aiming at surface roughness evaluation has been presented. The method employed enables non-destructive sidewall inspection on full wafer, without the need for sample coating or cut. The technique looks promising, providing consistent estimation of waveguide sidewall topography. However, due to the roughness values to be assessed as provided by LER measurement, it might be difficult to obtain a reasonable trade-off between high stereo angle and pair image matching requirements. Consequently, an alternative way is investigated, and consists in the use of a shape-from-shading algorithm to retrieve sidewall topography from a single SEM image.

II.4 Shape-from-shading approach

The algorithm selected for this study and its implementation are initially described in section 1. Section 2 presents reconstruction results on SEM sidewall pictures. Calibration issues are discussed in section 3, introducing the roughness measurements and comparisons of section 4.

II.4.1 Algorithm implementation

As suggested by its denomination, a "shape-from-shading" (SFS) algorithm provides the shape, topography, of an illuminated surface, by analyzing the shadow and bright areas produced in the resulting image by the illumination process. Such a technique may of course be employed with real-life pictures under light illumination, but also with those formed from electron scattering, as it is the case with images coming from a SEM for instance. Interest in integrated circuit characterization led to the application of SFS algorithms to SEM pictures with metrological purposes [Jones, 1994; Ellison, 1991; Beil, 1990; Beil, 1991]. The algorithms implemented were mainly global, that-is-to-say that they imposed constraints on the whole image to ensure the convergence of the solution corresponding to the reconstructed profile, and the approaches were generally coupled with stereoscopy, for data reliability enhancement. Although offering up to excellent accuracy in the estimated surface profile, global constraints have the drawback of being computer-time-consuming, and algorithms using local constraint are often preferred when time considerations are dealt with. As it was seen in section II.3, stereoscopy requires a second picture of the same physical area under different illumination or observation conditions, and the use of a pattern matching algorithm to identify the same features on both images.

Our approach was first to apply a local SFS algorithm on a single SEM image. An algorithm proposed by Tsai and Shah [Tsai, 1994] was adapted under MATLAB (The MathWorks, Inc.). The reasons for selecting this algorithm are its relative shortness (around 30 lines of code), its speed of execution (the algorithm uses a local method to compute the height profile), and of course supposed efficiency and robustness. Due to the local nature of the initial algorithm, we adapted it for MATLAB software with matrices, thus achieving parallel-like calculations for all the pixels contained in the image, and thus enabling faster execution of the program.

The basis below SFS-based surface reconstruction lies in the link between surface nature and topography, illumination conditions, and resulting intensity image. Such a relationship is formalized by the so-called image irradiance equation :

$$I(x,y)=R(p,q) \quad (20)$$

where I is the position dependent intensity on the image, and R the reflectance function of the surface, taking into account illumination conditions. p and q denote the surface depth gradients along x and y directions respectively. The reflectance model for SEM images [Jones, 1994; Bunrit, 2000] was used in place of the traditional model for Lambertian surfaces [Tsai, 1994; Bunrit, 2000]:

$$R(p, q) = \frac{\sqrt{p+q+1}\sqrt{p_s+q_s+1}}{pp_s+qq_s+1} \quad (21)$$

where $p_s = \frac{\cos \tau \sin \sigma}{\cos \sigma}$ and $q_s = \frac{\sin \tau \sin \sigma}{\cos \sigma}$, with τ and σ being respectively the tilt and slant angles of the illuminant, and thus take into account the geometrical illumination conditions.

The particularity of the implemented algorithm [Tsai, 1994] lies in the linearization of the reflectance function in Z (surface height) instead of surface gradients (p and q), and in the use of discrete approximation for p and q by finite difference:

$$p = \frac{\partial Z}{\partial x} = Z(x, y) - Z(x-1, y) \quad \text{and} \quad q = \frac{\partial Z}{\partial y} = Z(x, y) - Z(x, y-1) \quad (22)$$

The authors [Tsai, 1994] reach a relatively simple formula to iteratively compute the surface height profile $Z(x, y)$:

$$Z^n(x, y) = Z^{n-1}(x, y) + \frac{-f(Z^{n-1}(x, y))}{\frac{d}{dZ(x, y)} f(Z^{n-1}(x, y))} \quad (23)$$

where n is the iteration order, and $f(Z(x, y)) = I(x, y) - R(p, q)$.

Details for coding the algorithm are given by Tsai and Shah [Tsai, 1994], and involve the implementation of a Kalman filter and a zero value for initiating the iteration of the surface height profile Z .

II.4.2 Profile reconstruction

The test sample assessed in this study was fabricated by FHD of a buffer and core silica layers on top of a thermally oxidized silicon wafer. The core layer was 5.5 μm -high, and etched by standard RIE process. Our images are typically recorded at 1.5kV operating voltage, with magnification of the order of 40,000 times, and saved under 1024x768 pixels coded over an 8-bit grey scale.

The previously described algorithm was directly applied to SEM pictures, and Figure 28 shows an example of a reconstructed waveguide sidewall profile (left), together with its corresponding SEM image (right). The image area of which the profile is represented is delimited by the two horizontal lines.

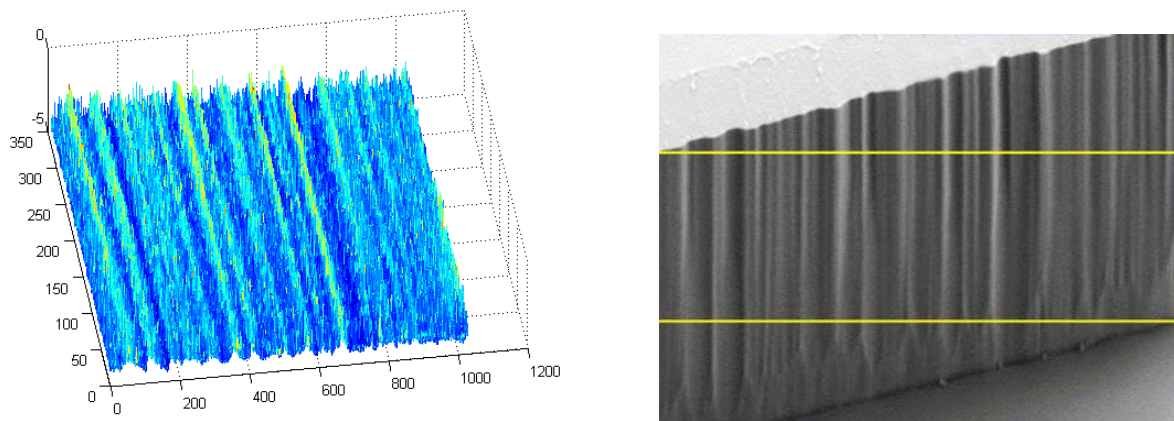


Figure 28: Reconstructed waveguide sidewall profile (left) and corresponding SEM image area (right).

Although the reconstructed profile does present the same vertical striations as the waveguide sidewall on the SEM picture, the general striking feature is the noisy aspect of the profile. This may come from the noise in the SEM image originating from the electron detectors, this noise creating discontinuities in the calculated profile. As the noise in the original SEM picture is constituted of isolated intensity peaks, a low-pass filter available within AnalySIS software from Soft Imaging System GmbH was applied, thus performing a Fourier-based filtering. The filtered image is not displayed here, because no difference would be observed at this scale of display. However, the filter does remove most of the noise on the SEM image, without damaging the edges or the high intensity contrasts. Evidence for this constation is provided by looking at the intensity histogram of the difference between original and low-pass filtered SEM images, which takes a form similar to the one of a white noise as displayed on Figure 29.

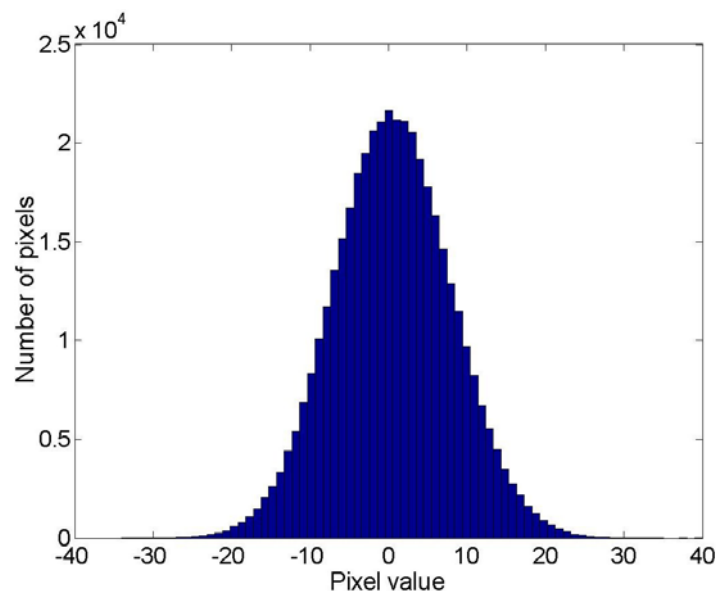


Figure 29: Pixel value histogram for the subtraction of filtered image to original image.

The shape-from-shading algorithm was then applied to the low-pass filtered SEM image. Figure 30 shows two reconstructed profiles of the same area presented on Figure 28 (right). The profile on the left is the same as the one of Figure 28, the one on the right was obtained after the SEM image of Figure 28 had been processed with the low-pass filter.

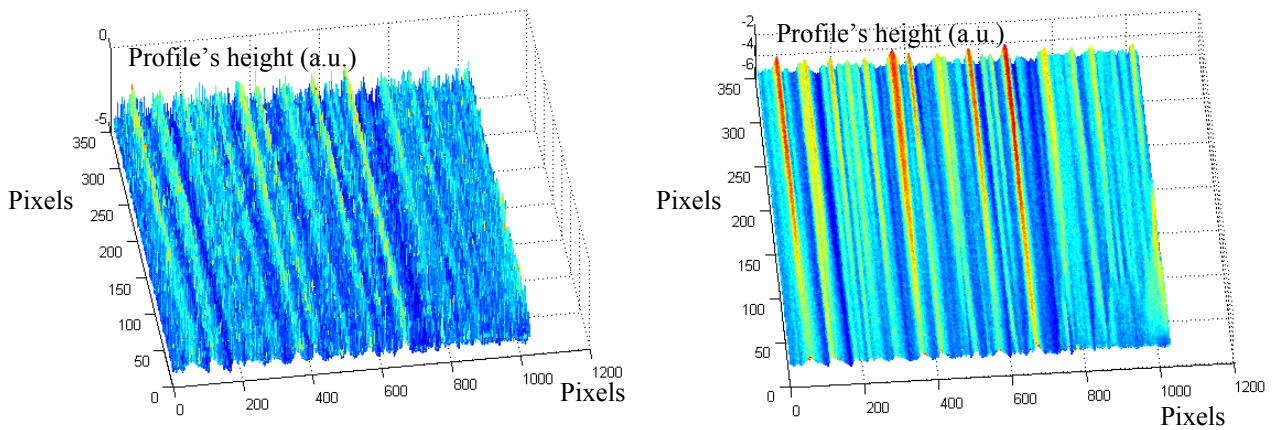


Figure 30: Reconstructed profiles from initial SEM image (left) and low-pass filtered SEM image (right).

As it can be noticed on Figure 30, the new profile contains less noise, and presents distinguishable and identifiable (with respect to the corresponding original SEM image) vertical striations.

II.4.3 Calibration issues

The SEM image being composed of intensity data pixels, the reconstructed profile only contains height values that do not reflect the object dimensions but are proportional to them. Consequently, there is a need for calibrating this height profile. The method we propose is to first characterize the studied sample by top-down SEM imaging, i.e. by imaging the waveguide from its top. The procedure to extract roughness has been described in section II.2.2.

Once the RMS roughness has been extracted via LER measurement, the same value in meter is attributed to the standard deviation of the upper line on the reconstructed sidewall profile. RMS values on lower parts of the waveguide sidewall may then be calculated assuming proportionality relationship is preserved as a function of sidewall's height position.

In our case, such a calibration step is eased due to the tilt of the waveguide sidewall of the order of 3° . However, this angle is not a necessary condition, and LER may be extracted whatever the sidewall angle.

For the calculations induced by the shape-from-shading algorithm, this tilt can be taken into account by a modification of tilt angle τ . Indeed, this tilt angle represents the orientation of the surface of interest with respect to the illumination source. For instance, a sidewall tilt of 3° as represented on Figure 18 leads to a tilt value of 48° , whereas the physical sample tilt within the sample is 45° .

II.4.4 Roughness distinction and resolution

This calibration procedure applied to the sample area displayed on Figure 28 led to RMS roughness values of 25nm and 14nm, for lines measured respectively on the upper and lower parts of the sidewall, as well as to decreasing roughness values when going from the top to the bottom of the inspected area. This is a first indication that the technique can potentially resolve between different roughness amplitudes, considering that on the SEM picture the lower part seemed to be smoother than the upper one.

A second sample was investigated as an attempt to assess the limits of the SFS technique. It shows different form of surface roughness, as one can see on Figure 31 (left part). The associated reconstructed surface profile is displayed on Figure 31 (right part). LER measurement for sample 2 led to RMS roughness value of 25nm, and deduced RMS value of 7nm for the lower part of the sidewall. This second example demonstrates the ability of the technique to reconstruct even low-contrast low-roughness-amplitude areas.

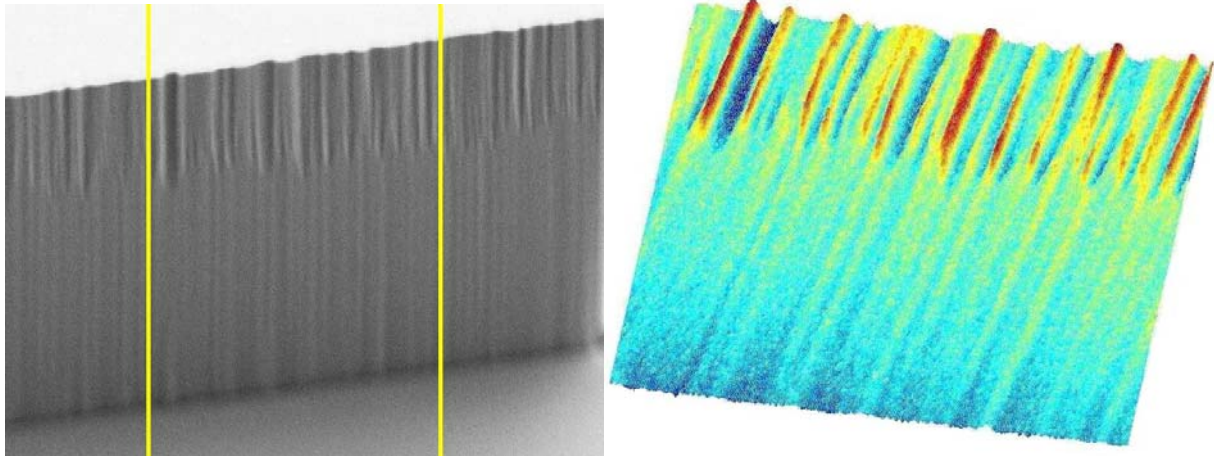


Figure 31: SEM image of 2nd sample and inspected area (left), and corresponding reconstructed profile (right).

The resolution of the technique is in fact limited by the distinguishable features present on the SEM image. Consequently, it has the same order of magnitude as the resolution of the instrument, which is in our case 2.1nm at 1.0kV operating voltage. Taking closed lines in the bottom part of sample 2, standard deviation of estimated RMS roughness values was found to be below 5%, which represents around 0.3nm. The accuracy of the technique depends however on the accuracy of the calibration step, in our case on LER measurement.

II.4.5 Issues for practical implementation

When trying to implement the technique for routine measurement, several practical issues appear. Three legitimate questions are :

- is it necessary to perform LER calibration for every SFS-based measurement ?
- what is the influence of instrument contrast settings on measurement ?
- how the pre-filtering step may affect the following measurement ?

These issues are of importance for measurements aiming at process refinement or fabrication control. Indeed, these operations imply roughness comparison not only on several part of a waveguide, but also on different waveguides on the same wafer and ultimately on waveguides on different wafers.

In order to answer these questions, this sections starts with a definition of contrast, the different sorts of operation to modify it. The link between contrast modification and shape-from-shading is then adressed. The consequences of contrast modification on retrieved roughness parameters are then illustrated on a concrete example. This section is completed with practical recommendations for implementation of a shape-from-shading-based sidewall roughness measurement procedure.

II.4.5.1 Contrast modification procedures

Contrast:

Image contrast may be defined in several different ways. Three main definitions are commonly adopted.

A local definition of contrast [Colliex, 1998] can be expressed as

$$C1 = \frac{I(x + \Delta x, y + \Delta y) - I(x, y)}{\overline{I(x, y)}} \quad (24)$$

where $\overline{I(x, y)}$ stands for the mean value of intensity calculated over a neighborhood of (x, y) .

Extending this notions to the whole image, one may use the following formula:

$$C2 = \frac{\sigma(I)}{\langle I(x, y) \rangle} \quad (25)$$

with $\langle I(x, y) \rangle$ being the intensity averaged over the whole image and

$$\sigma(I) = \frac{1}{\text{Number_of_pixels}} \sum (I(x, y) - \langle I(x, y) \rangle)^2 \quad (26)$$

Another way of defining global image contrast is via the formula:

$$C3 = \frac{\max(I) - \min(I)}{\max(I) + \min(I)} \quad (27)$$

where $\max(I)$ and $\min(I)$ are respectively the maximum and minimum intensity values of the image.

Despite the differences between these mathematical formulations, the idea linked to contrast remains how strong intensity variations are on a given spatial scale. From an observer's point of view, these variations are assimilated to visual detail visibility. Therefore, the notion of contrast enhancement is somehow subjective, and may vary along with the user. A large set of procedures and treatments are available for contrast enhancement. Next section thus sorts out these techniques as a function of the area they consider on the image before modifying it.

Point, local and global operation on images:

A point operation performed on an image results in an image where a given output pixel's gray level depends only on the gray level of the same pixel in the original image [Castleman, 1996]. Two classical applications for point operation are display optimization and contrast-stretching. They consist in extending the range of intensity values taken by image pixels following affine transformation. Thus a given new pixel value only depends on the previous pixel value and on the parameters for transformation.

Local transformations take into account the immediate neighborhood of a pixel to process it [Pérez, 2000, p. 486]. Classical examples of local operations consist in the application of a matrix convolution mask composed of fixed coefficients. The following operator

$$\frac{1}{10} \begin{bmatrix} -1 & -1 & -1 \\ -1 & 8 & -1 \\ -1 & -1 & -1 \end{bmatrix} \text{ represents the local weighted mean, an example of contrast enhancement.}$$

They are linear filters. Non-linear local operators are for instance median and mode operators. The median operator [Jain, 1989, p. 246] attributes to the processed pixel the central value of a set of values sorted in ascending order, whereas the mode operator attributes the most frequently appearing value in this set of values. Both types of local operators may be used to enhance contrast. Another type of local operator is the differential operator, which is the local gradient of the image [Pérez, 2000]. For the case of centered finite differences, it is expressed as

$$\nabla I(x, y) = \frac{I(x+1, y) - I(x-1, y)}{2} e_x + \frac{I(x, y+1) - I(x, y-1)}{2} e_y \quad (28)$$

When the finite differences are not centered, it may be expressed as

$$\nabla I(x, y) = [I(x+1, y) - I(x, y)]e_x + [I(x, y+1) - I(x, y)]e_y \quad (29)$$

The shape-from-shading algorithm [Tsai, 1994] implemented for sidewall roughness evaluation makes use of the finite differences described here.

Finally, a global operator provides a resulting image where a given pixel's value depends of all the pixels of the initial image. Two typical widely used global transformation are discrete Fourier transform, and histogram equalization, the latter consisting in modifying image's intensity histogram so that each intensity set considered has as many representing pixels as the other sets.

As a summary, contrarily to local and global operations, a point operation does not take into account neighbor pixels, and consequently does not alter the spatial relationship within the image processed.

Contrast settings and enhancement for SEM images:

Display optimization is typically performed when imaging within the SEM for better visibility, via modification of so-called contrast and intensity settings. This can be more or less assimilated to a contrast-stretching procedure. The next two sections will investigate the influence of this contrast modification on the shape-from-shading approach for waveguide sidewall metrology purposes.

In the domain of line-edge-roughness metrology, several image treatments are already widespread, such as image smoothing (for instance median or mean convolution processing) and edge enhancement (like via differential operator). Although their use is usually accepted, their influence on measurement data is not always well characterized, and thus somehow problematic [Solecky, 1999].

In this study, the pre-processing corresponding to low-pass filtering of SEM images before applying shape-from-shading algorithm is questionable. Although this global transformation proved unavoidable to ensure an acceptable result in terms of surface profile, its consequences in terms of surface distortion and error on the extracted roughness parameter is not straightforward to deduce.

II.4.5.2 Link between shape-from-shading and contrast modification

As the shape-from-shading algorithm implemented uses finite differences, a first step is to look at the influence of contrast modification on finite differences.

Let assume that an affine point transformation on an image defined by its pixel intensity $I_1(x, y)$. The point operation can be seen as modifying $I_1(x, y)$ into $I_2(x, y)$ in such a way that

$I_2(x, y) = aI_1(x, y) + b$ where a and b are constant values. One may now ask about the consequence of such a transformation on finite differences performed in the shape-from-shading approach.

$$I_2(x+1, y) - I_2(x, y) = a I_1(x+1, y) + b - a I_1(x, y) - b = a[I_1(x+1, y) - I_1(x, y)] \quad (30)$$

Similar straightforward calculations lead to the conclusion that this point transformation changes p and q into $a p$ and $a q$ respectively. This conclusion remains valid for the case of centered finite differences.

In [Tsai, 94], the surface height at a given position is iteratively calculated using the formula :

$$Z^n(x, y) = Z^{n-1}(x, y) + \frac{-f(Z^{n-1}(x, y))}{\frac{d}{dZ(x, y)} f(Z^{n-1}(x, y))} \quad (31)$$

where n is the iteration order, and $f(Z(x, y)) = I(x, y) - R(p, q)$.

In [Tsai, 94], f and df/dZ are expressed with Lambertian reflectance model. Below are the expressions for SEM reflectance model [Bunrit, 2000].

$$f(Z(x, y)) = I(x, y) - \frac{\sqrt{p+q+1}\sqrt{p_s+q_s+1}}{pp_s+qq_s+1} \quad (32)$$

We then calculated the expression of df/dZ and obtained (cf. Annex C):

$$\frac{df(Z(x, y))}{d(Z(x, y))} = - \left\{ \frac{\sqrt{p_s+q_s+1}}{pp_s+qq_s+1} \left[\frac{1}{\sqrt{p+q+1}} - \frac{(p_s+q_s)\sqrt{p+q+1}}{(pp_s+qq_s+1)} \right] \right\} \quad (33)$$

It can thus be noticed that the relationship between estimated surface height and gradient is not linear. Consequently, it is not straightforward to derive a formula quantifying the effect of contrast modification on reconstructed Z height profile.

II.4.5.3 Consequences for practical SFS-based sidewall roughness measurement

It can be deduced from the previous section that the reconstructed Z values obtained depend on the image contrast. Particularly, they are not a priori preserved after image contrast modification. However, as they are relative values before the calibration step, these values are not of prime importance. The most relevant feature to be considered is the proportionality relationship between the Z standard deviations corresponding to areas with different height positions on the waveguide. It is intuitive that given any two SEM images recorded free of saturation for two different contrast settings, assuming the shape-from-shading model is

correct, there should be a spatial correspondence between respective estimated topographies. In the same vein, the conservation of the spatial correspondences within the image constitutes a sufficient condition to keep the proportionality relationship.

To illustrate this point, the SEM image used as a second example (cf. Figure 31) is investigated. The protocole is as follows : the image is first duplicated and processed, resulting in an initial non-modified, contrast-stretched, median-filtered and histogram-equalized images. Parameters for contrast stretching are $a = 2$ and $b = -100$, a 3×3 mask for median convolution processing; the histogram equalization procedure is as available within Matlab software. Only the part of the image used for shape-from-shading profile estimation was processed. Figure 32 shows respectively the original, contrast-stretched, median-processed and histogram-equalized images, with their corresponding intensity histograms represented on Figure 33.

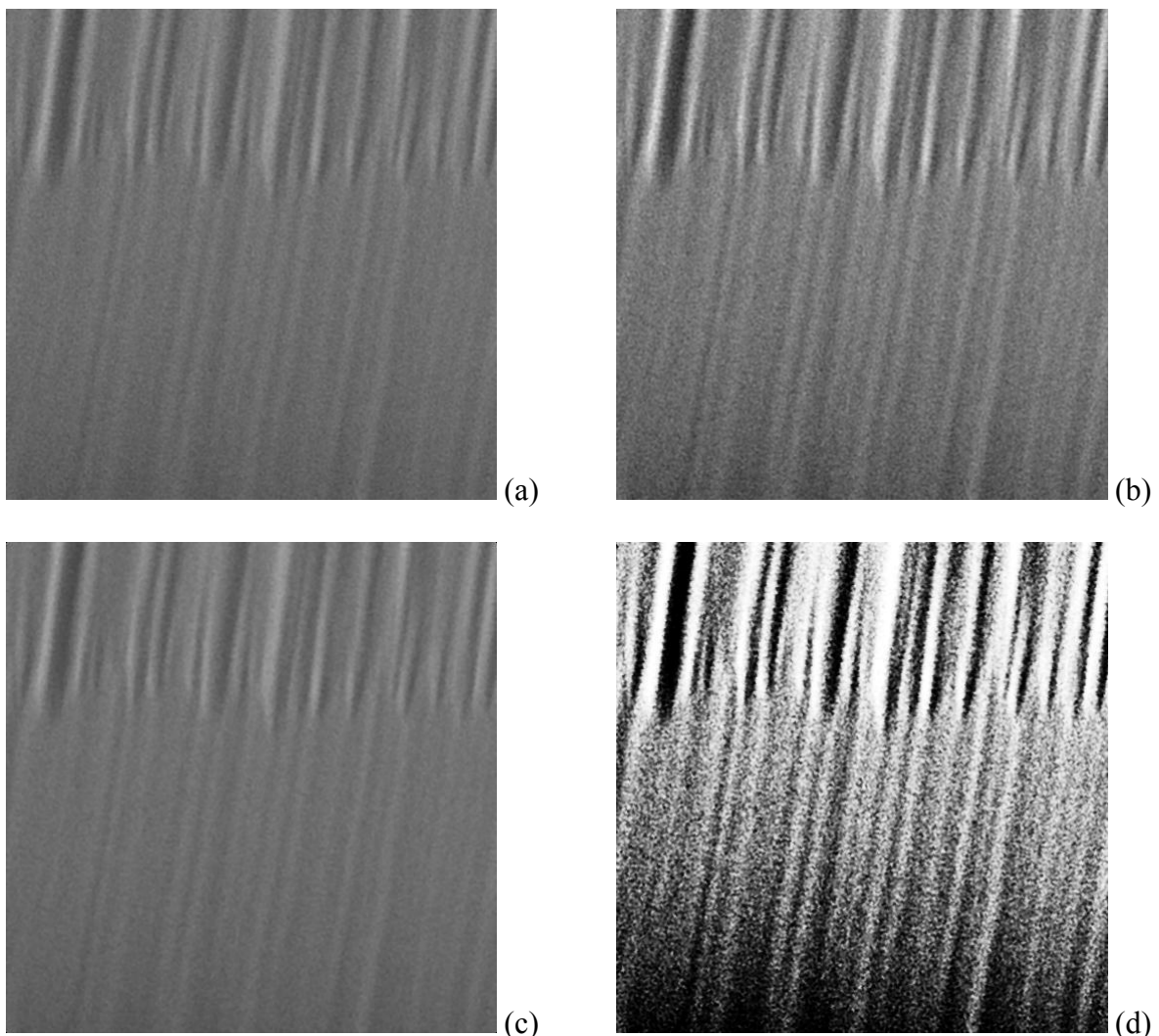


Figure 32: Original (a), contrast-stretched (b), median-processed (c), histogram-equalized (d) images.

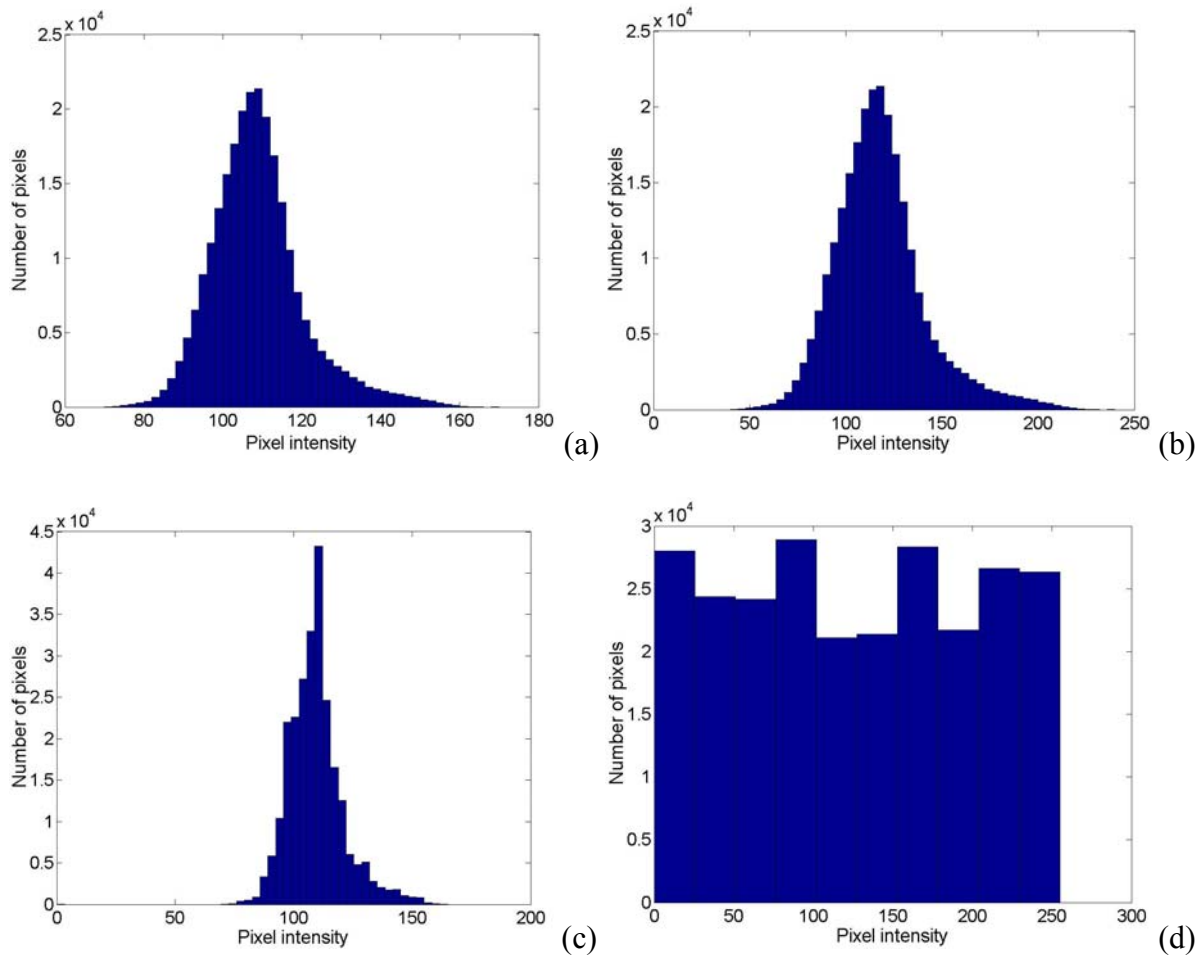


Figure 33: Intensity histograms corresponding to original (a), contrast-stretched (b), median-processed (c), histogram-equalized (d) images.

Visually, the unprocessed and median-processed images are hard to distinguish, whereas the contrast-stretched looks better (with details more easily distinguishable) and the histogram-equalized seems to exaggerate details and to saturate the image. However, the intensity histograms coming from unprocessed and median-processed images do differ, which comes as no surprise considering the nature of median processing. Although presenting different values on x -axis, the histograms from unprocessed and contrast stretched images have the same shape, as the contrast-stretch procedure simply dilates histograms. As expected from its definition, the histogram-equalized image presents an histogram of which the shape is relatively equally spread over the set of values accessible for the pixels.

The reconstructed surface topographies are similar in shape, and can be seen on Figure 31 (right part). The main parameter used for quantitative roughness assessment being surface height standard deviation, Figure 34 represents it as a function of vertical position on the sidewall for the case of the unprocessed and contrast-stretched SEM images.

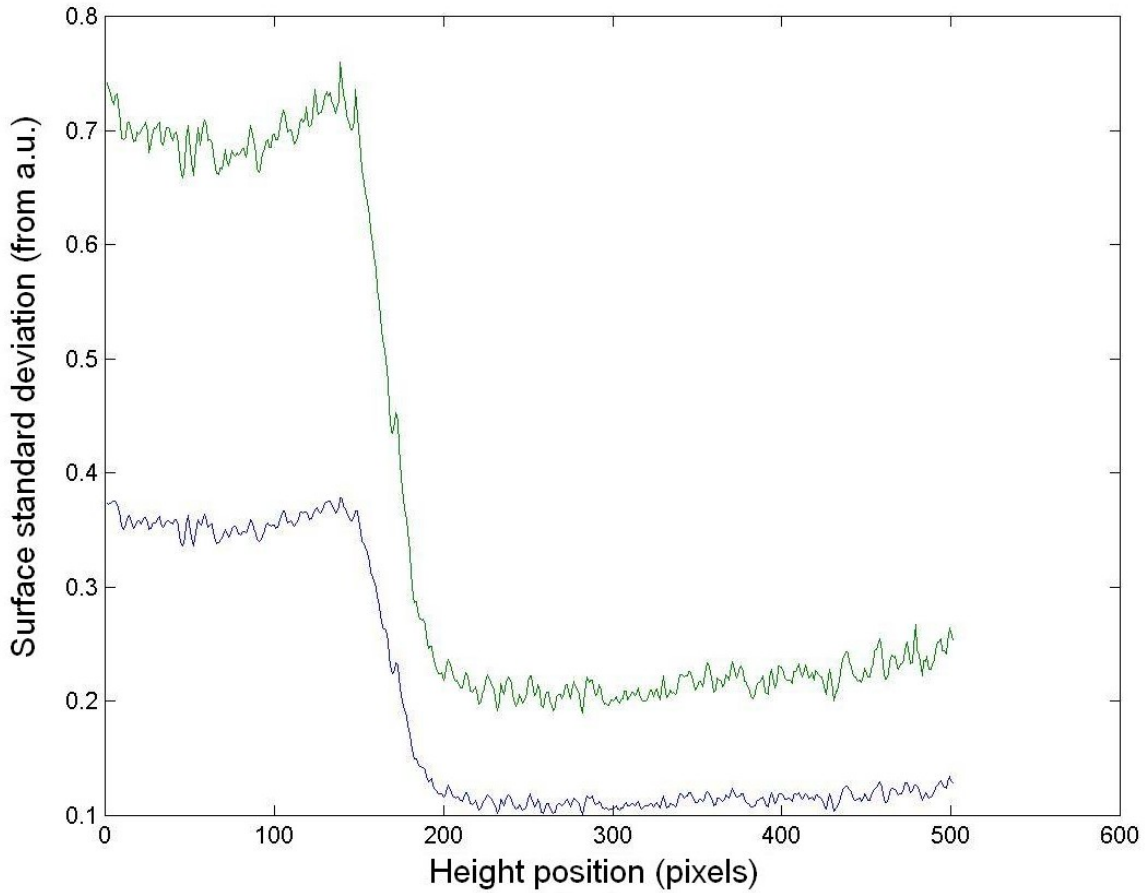


Figure 34: Profile standard deviation as a function of vertical position on the sidewall, extracted from original SEM image (lower) and contrast-stretched image (upper).

The upper curve comes from the topography reconstructed with the contrast-stretched SEM image, the lower one from the original SEM image. It is noticeable, as will be confirmed below by quantitative analysis, that the contrast-stretching procedure preserves the standard deviation ratios across the whole reconstructed profile. This can be observed on Figure 34 by noticing the similarity of both curves down to small variations, the upper being actually nearly the lower multiplied by 2 (multiplying factor also applied in the contrast-stretching procedure). The corresponding curve coming from the median-processed SEM image (not plotted here for clarity) mimics the lower curve on Figure 34, however departing slightly on small scales. The corresponding curve coming from the contrast-equalized SEM image (not plotted here) does not keep the proportionality relationship between the lines, and tends to comparatively overestimate surface height variations on the lower part of the sidewall.

Table 3 reports the surface height standard deviation around lines 50, 250 and 400. Values are obtained with averaging over 9 lines around the central line. Topographies are calculated with 20 iterations.

Line	Original	Contrast-stretched	Median-processed	Histogram-equalized
50	0.2368	0.4729	0.2336	1.1721
250	0.0675	0.1345	0.0632	0.5781
400	0.0682	0.1361	0.0637	0.6194

Table 3: Surface standard deviations for different initial image.

The ratios between standard deviations from different lines of the reconstructed surface are reported in Table 4 for surfaces reconstructed from the different SEM images. These ratios being afterwards related to RMS roughness values, they are of prime importance in comparison with direct standard deviations.

Line Ratios	Original	Contrast-stretched	Median-processed	Histogram-equalized
50/250	3.508	3.516	3.696	2.028
50/400	3.472	3.475	3.667	1.892
250/400	0.990	0.988	0.992	0.933

Table 4: Ratios of standard deviations.

As it can be supposed from Figure 34 and Table 4, the contrast-stretching procedure only slightly alters the line standard deviations' ratios. On the contrary, the median processing alters the ratios in a moderate, but rather unpredictable way, and the histogram equalization completely denatures them.

II.4.5.4 Practical recommendations and alternatives

The following points have been evidenced in this study. First, contrast stretching, although visually enhancing SEM image, does not result in more accurate reconstructed profile. Other contrast enhancement approaches, non-transforming p and q linearly, are not adapted to shape-from-shading due to the alteration of spatial relationships they may introduce.

Secondly (and practically), it has been shown that, taking a given waveguide sidewall of which the statistical roughness parameters are to be extracted, the combination of LER and shape-from-shading lead to a result independent of contrast (assuming there is no saturation when the image is recorded). This point of course legitimates the approach for metrology purposes.

Finally, it has also been shown that there is no bijective relationship between RMS surface roughness and reconstructed profile's standard deviation (cf. Figure 34). This means that LER calibration performed on a given sample can not be directly transposed for roughness measurement on another sample or waveguide for an image recorded in arbitrary contrast conditions. However, it is noticeable that keeping the same brightness and contrast settings when recording the SEM image, direct standard deviation comparisons can be performed between images of distinct waveguides on the same sample.

Assuming the same material composes a series samples (which is often the case for serial production). In the perspective of in-line control, this means one potentially needs just perform a single LER calibration, and may thereafter quantitatively assess a full batch of wafers.

II.4.6 Extension to deep silica etching

Previous section has emphasized the care that should be attributed to contrast settings and characteristics when comparing surface areas on distinct waveguides or samples. In this section, we discuss the precautions that should be taken into consideration when applying the previously designed shape-from-shading approach to largely higher waveguide.

The previously studied samples were composed of $5.5\mu\text{m}$ -high waveguides, with dimensions of typical interest for telecommunications-oriented components. In the micro-fluidic domain, one may etch trenches into silica of the order of $40\mu\text{m}$ depth, with the purpose to use the resulting etched channels as paths to convey fluids. Examples of such realizations can be found in [Ruano, 2000].

Over such significant etching distances, height dependent sidewall roughness may be a more striking factor than in the simpler case of $5\mu\text{m}$ -etching. Figure 35 illustrates this fabrication-induced aspect for a $40\mu\text{m}$ -high sidewall etched at Alcatel SEL AG.

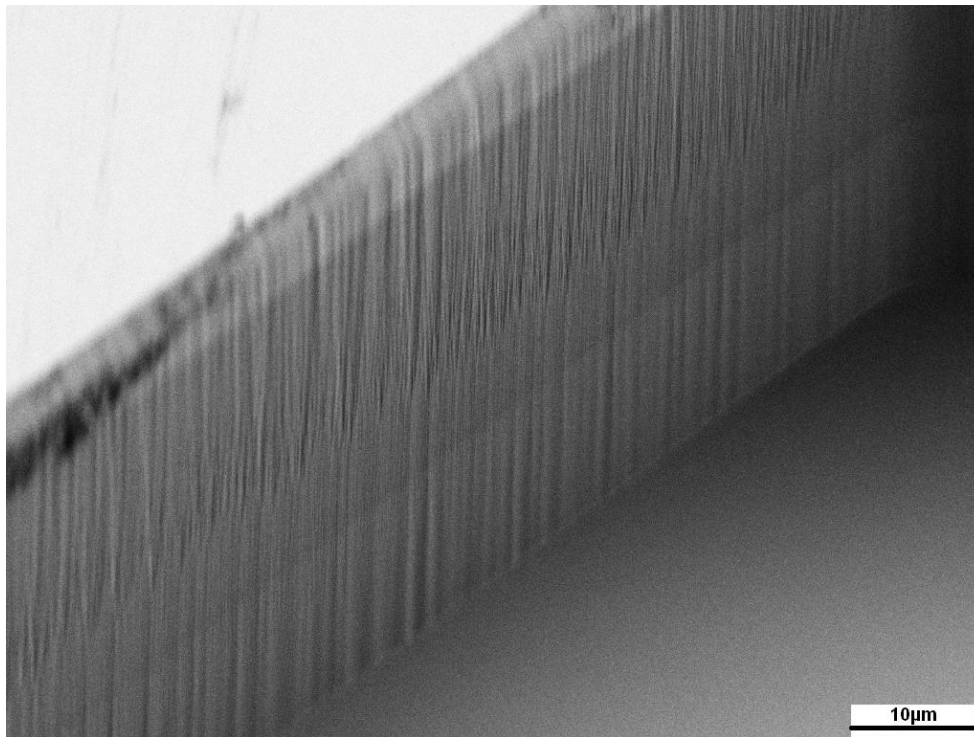


Figure 35 : Sidewall from $40\mu\text{m}$ -etched silica sample.

As it can be seen on Figure 35, the sidewall presents different roughness aspect as a function of the height considered on the sidewall. Although the influence of sidewall roughness is not as well characterized for the case of microfluidic transport as for the case of waveguide light scattering, there may be interest in roughness evaluation aiming at process refinement.

Three major issues appear in the practical implementation of the shape-from-shading technique for high walls. First, due to the dimension of the wall, it is not possible to image the whole sidewall while using sufficient magnification to correctly define all roughness features

on its surface. This then implies imaging several parts of the sidewall, and thereafter applying the shape-from-shading. Thus care has to be taken to conserve contrast settings when moving from one to other part of the sidewall. Ideally, one should keep some common features between two successive areas on the sidewall, for ulterior comparison of the standard deviation values and potential adjustment. Secondly, due to wall's height and tilt angle for observation (45°), it is necessary to change focus (and maybe stigmation) settings between distinct inspected parts of the sidewall. This feature was not present for the inspection of $5.5\mu\text{m}$ -high sidewalls due to the depth of field of the SEM that could ensure the whole sidewall to be imaged in focus, but it has to be considered when applying SFS technique to $40\mu\text{m}$ -high sidewalls. Finally, the calibration step has to be carried out with care. Indeed, in top-down imaging configuration, the scales being the same along the direction of the sidewall and the direction perpendicular to it, it is not possible to image a length of sidewall comparable to the one displayed on Figure 35 with the necessary resolution to measure its LER. A portion of the line has to be selected, which may lead to meaningless data. The procedure should consequently be repeated and averaged.

Once these precautions have been taken, the SFS technique preserves its initial advantages: it enables quantitative roughness comparison between different areas on the sidewall, both with respect to RMS value and to auto-correlation function.

II.5 Comparison of stereoscopy, SFS, and competing techniques.

In this section, the two SEM-based techniques developed in this study for sidewall roughness assessment are compared. Their use for industrial on-site implementation is then discussed with reference to competing techniques.

II.5.1 Comparison of stereoscopy and shape-from-shading techniques

When comparing the stereoscopic and the shape-from-shading (SFS) procedures, the first point that deserves attention is the need for calibration in the SFS technique with the values coming from top-down imaging, whereas the stereoscopic method can a priori be applied straightforwardly. Due to the high discrepancies between quantitative values coming from the stereo approach and the top-down measurements, the calibration of the SFS technique results in large differences between roughness values provided by the two techniques. However, the two techniques are capable of reproducing qualitative sidewall profiles, with a clear advantage for the SFS approach due to its direct addressing of SEM image intensity contrast texture.

An apparent difference between the two techniques lies in their sensitivity for quantitative roughness distinction. The second waveguide sidewall taken as an example illustrated this feature. The SFS technique takes full advantage of the SEM resolution present in image contrast to detect height variations below 10nm, providing data with low dispersion. On the contrary, even for stereo angles of 40°, the vertical resolution of the stereoscopic technique does not exceed 10nm. And this limit is even reduced due to the difficulty for pattern matching induced by the unwanted tilt in the y -direction of the stereo SEM images.

Table 5 summarizes the comparison between the two roughness evaluation techniques.

	Stereoscopy	Shape-from-shading
Need for calibration	No	Yes
Agreement with single SEM image	Generally good	Excellent
Comparison with values from top-down line-edge roughness measurement	Stereoscopic values seem to be over-estimated	Top-down values used for calibration
Quantitative roughness distinction on a single sample	Depends on the roughness magnitudes	Excellent
Sample comparison	Poor sensitivity	Good
Repeatability	Medium	Good
Dependence on image content	Texture contrast sensitive	Brightness and contrast

Table 5: Comparison of stereoscopic and shape-from-shading approaches.

II.5.2 Comparison with competing techniques

From the study carried out in this thesis, it may be expected that the shape-from-shading approach would satisfy the resolution and repeatability requirements. Consequently, the following discussion is restricted to this technique. When SEM is employed in metrology departments for development/fabrication process control, it is mainly in the form of LER measurement or visual inspection as illustrated in section 2 of this chapter. The shape-from-shading technique can thus be seen as a complementary extension for full sidewall surface reconstruction and consecutive roughness measurement.

Over most of AFM commercial set-ups already in use or available, the SEM-based SFS technique has the advantage provided by the apparatus. Indeed, most of SEMs can accommodate large (from 10cm diameter) wafer, without specific sample preparation or cut, what is usually not the case with most of AFMs. For the special case of sidewall roughness measurement, the SFS technique has the advantage stated in the initial requirements imposed prior to this study. Namely, the technique enables sidewall roughness measurement on full wafer, without the need to cut the sample to isolate the surface area of interest. The approach to visualize the sidewall is also easier within the SEM than within classical AFM with the sample tilted to 90° to access sidewall's area.

Recently, several AFM set-ups specially dedicated to sidewall roughness measurement on full wafer have been developed (following the principles stated in [Nyyssonen, 1991; Martin, 1994]) and become available. Although the resolutions are not always as good as within classical AFMs, they present the definite advantage of complete automation. This feature make them user independent, what is an appreciable feature in production facilities for instance. However, the state of development of commercial SEMs, particularly their ability for precise positioning with any given settings of coordinate or tilt angle, and of the robot vision domain, specially the ability to find a given sidewall area, could enable the realization of an SEM-based equivalent apparatus. After an automated LER measurement, the coordinate on the sample would be kept to find and image the corresponding sidewall area, then reconstruct it using the shape-from-shading algorithm before extracting line roughness values as a function of height position on the sidewall. The computing time to reconstruct surface profile from SEM image being of the order of a few seconds, this would make the technique thereafter well suited for in-line inspection.

II.6 Ideas for further developments

Concerning the stereo roughness measurement technique, it looks difficult to enhance the image recording step. Applying larger angles could increase the vertical resolution, but would result in an even more difficult pattern matching between the two stereo images. However, there are still at least two possible ways of improving the processing step. First, as suggested p.319 in [Horn, 1986], correlation-based pattern matching may perform better when applied to edge-enhanced pictures instead of raw (SEM) images. Although we tried to look for improvement in this direction, we did not obtain noticeable result. Secondly, one could think about implementing another matching algorithm, not specially based on correlation as developed within the AnalySiS software.

Further work on the shape-from-shading approach would first imply addressing calibration issues with standard samples of the same order of roughness magnitude. The algorithm selected proved to work fast and quite well, but improvements in profile reconstruction may be obtained through higher-order linearization in depth [Tsai, 1994; Bunrit, 2000] in the model coupled with an appropriate optimization algorithm, or via the implementation of other existing shape-from-shading algorithms, like those using global constraints.

Associations of stereoscopy and shape-from-shading have been reported in literature, and are based on fusion between data obtained from both procedures [Beil, 1990 and 1991], and on the application of shape-from-shading algorithms to stereo pictures [Ellison, 1991] for instance. A preliminary study could be conducted to evaluate the potential implementation of these approaches to our purpose.

Quantitative comparison between these measurements and AFM sidewall assessment could be advantageous to ascertain the limitation of the presented techniques, and for calibration and uncertainties evaluation.

III Light scattering from silica-on-silicon wafers

Whereas the previous chapter was dedicated to roughness estimation of etched optical waveguides into silica, this chapter deals with the same type of wafers, but before waveguide etching. They are thus composed of a silicon substrate covered by a silica layer. Parameters of interest related to metrology are roughness of both air/silica and silica/silicon interfaces, refractive index and thickness fluctuations for the silica layer. As mentioned in section I.3.3, roughness could be evaluated for instance by AFM [Zúñiga-Segundo, 1994] or scattering ellipsometry [Germer, 2000]. Refractive index and thickness fluctuations could be mapped respectively by ellipsometry or interferometry [Perrot, 1995].

The global purpose in this work is not to compete with these techniques, but to explore the potential of laser light scattering approach for metrological purposes related to silica-on-silicon technology, with possible extension to any transparent layer on reflecting substrate thanks to the general character of the problem. As recent advances have been reported in literature on the comprehension of optical behavior for this sample configuration, the adopted approach has consisted in trying to repeat those experimental observations, to extend them, and to discuss them.

This chapter is thus organized as follows. A first section briefly recalls the notions necessary related to laser speckle and angular light scattering. The samples used in this study are described in the second section, together with the set-up realized. A third section reports results related to angle-resolved laser light scattering measurement, and last section those to angular speckle correlation.

III.1 Physical description of the studied phenomena

III.1.1 Physical origin of speckle

Speckle is the term employed to refer to the granular aspect of light scattered by a surface. Indeed, any given surface has roughness whose amplitude may vary from nanometer to micrometer range (or beyond depending on the field of application). The resulting speckle pattern arises from coherent interference between wavelets scattered by surface elements with different heights on the surface.

When studying a surface, there are two principal ways of obtaining a speckle pattern from light scattered by the surface. One consists in illuminating a surface with a laser beam, to collect light scattered via a lens or imaging system, and to record it with a CCD camera. Such a configuration is illustrated on Figure 36 and referred to [Briers, 1993] as imaged (or subjective) speckle pattern.

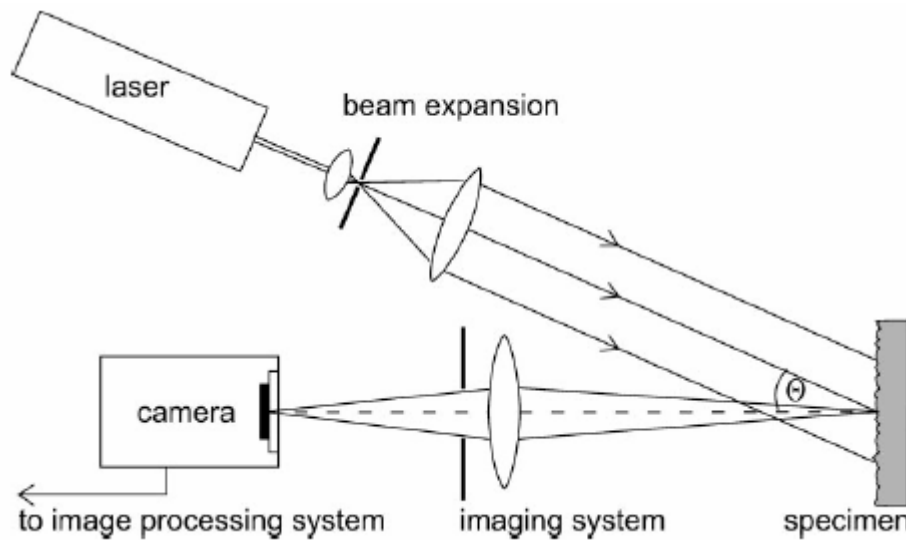


Figure 36: Set-up for imaged (subjective) speckle pattern recording (from [Fricke-Begemann, 2004]).

The second possibility is to replace the imaging system by a simple screen (or photographic film or CCD camera if the speckle pattern is to be recorded) on which the speckle pattern will be observed. The speckle pattern is then referred to as far-field (or objective) speckle [Briers, 1993], and Figure 37 illustrates this set-up configuration.

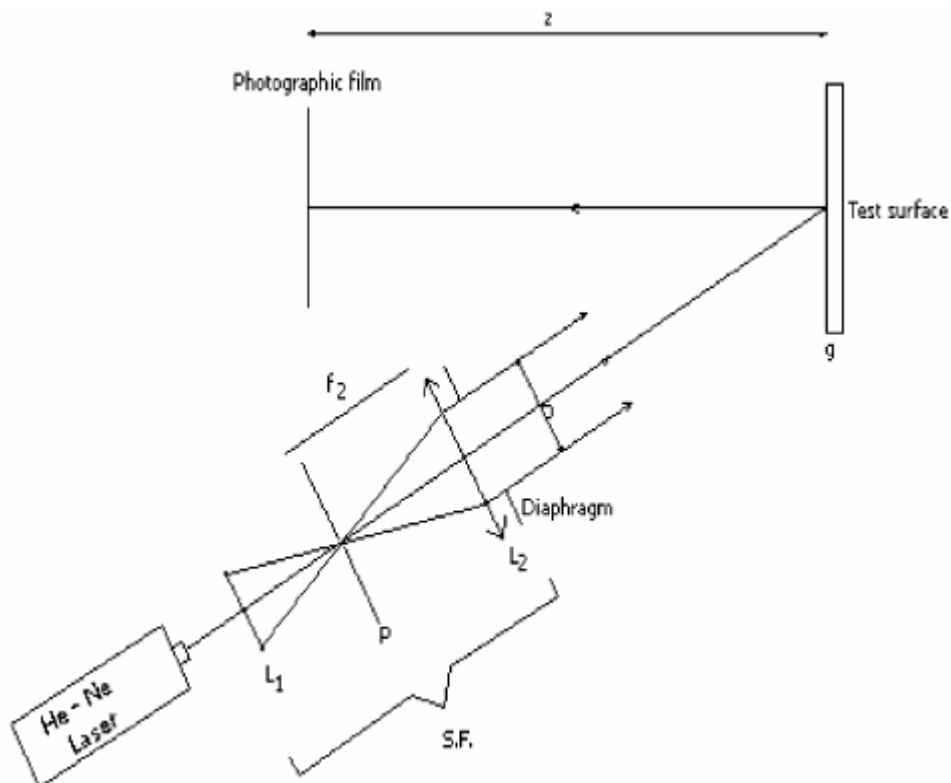


Figure 37: Set-up for far-field (objective) speckle pattern recording (from [Hamed, 2004]).

There is a fundamental difference in the formation conditions of speckle patterns in the two configurations. In the imaging configuration, every pixel is formed by scattering contribution of a unique surface element, comprised within a resolution cell of the imaging component. In

the subjective speckle configuration, every pixel composing the speckle pattern is an average of scattering contributions from all the surface elements of the illuminated area. As far as the statistical properties of those speckle patterns are concerned, no differences should be expected from results coming from either configurations assuming the number of scatterers involved is large enough [Dainty, 1984].

III.1.2 Speckle correlations

Depending on experimental optical wavelength, polarization and angular conditions, namely respectively incident and scattering angle for first pattern $(\theta_{i1}, \theta_{s1})$ and second pattern $(\theta_{i2}, \theta_{s2})$, the scattered intensity spatial distributions may exhibit a certain degree of correlation. Although one may vary the source's wavelength to observe these correlations, the easiest way remains by playing on the angular parameters, and following considerations will be limited to this case. The angles are evaluated as departing from the surface normal, and positive when varying as depicted on next Figure 38.

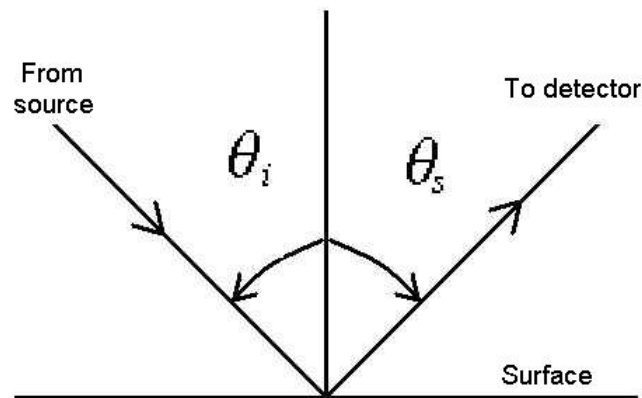


Figure 38: Notations for angles of illumination and scattering.

This paragraph reviews experimental techniques to evaluate these correlations and indicates the strategy usually adopted to look for them.

How to perform speckle correlations ?

An experimental approach to obtain speckle correlation values was used by Léger and coworkers [Léger, 1975]. It consists in recording two interfering speckle patterns obtained with different angles of incidence on the same film. When the two speckle patterns are correlated, they produce Young's fringes at the restitution step. The degree of correlation is assimilated to the visibility of the fringes. The same approach can be accelerated with the use of an interferometric set-up to combine both patterns [Léger, 1976].

Using a single photodiode, one may also perform speckle correlation by considering intensity data sets recorded for different surface areas on the sample [Knotts, 1992; West, 1999]. The degree of correlation is then evaluated as the coefficient correlation between two data sets obtained for distinct illumination and observation angle pairs. The method presents yet the

drawback of being time-consuming when dealing with large data sets and numerous angle pairs.

The natural extension of the preceding method is to employ a CCD matrix as a detector. For the special case of a surface presenting mono-dimensional roughness, the corresponding speckle pattern obtained possesses one-dimensional intensity variations, and the pixel values can be averaged along the columns of the detector [Lin, 1997]. The degree of correlation is then evaluated as the correlation between the resulting intensity vectors. For two-dimensional speckle patterns [Gorecki, 1994; Hinsch, 2000], the degree of correlation may be taken either as the correlation coefficient between the two images, or as the height of the correlation peak when it appears on the inter-correlation image. Both methods are described in section 4 of this chapter.

One should note that whereas the first method carries out amplitude correlation measurement, the following ones perform intensity correlations. Recently, another experimental set-up has been proposed [Gu, 2002a & 2004b], that can both perform amplitude and intensity correlations, but at the expense of set-up simplicity.

Where should speckle correlations be present ?

A fundamental question before recording speckle patterns aiming at correlation evaluation is the angular positions that have to be taken for this operation. Indeed, a complete exploration of all angular possible combinations would be a too long task. Therefore, a discussion on these conditions is provided in [Knotts, 1992]. Significant speckle correlation may be found under the following condition (sometimes referred to as C^1):

$$\sin \theta_{i1} - \sin \theta_{s1} = \sin \theta_{i2} - \sin \theta_{s2} \quad (34)$$

where $(\theta_{i1}, \theta_{s1})$ and $(\theta_{i2}, \theta_{s2})$ represents respectively the incident and observation (scattering) angles for the first and second speckle patterns considered. This condition leads to three particular configurations, where speckle correlation may be observed:

- (a) When keeping $\theta_{i1} = \theta_{i2}$ and slightly moving from formula (34) by scanning θ_{s2}
- (b) When departing from $\theta_{i1} = \theta_{i2}$ and keeping formula (34) satisfied
- (c) By using $\theta_{i2} = -\theta_{s1}$ with formula (34) satisfied, thus looking in a reciprocal scattering configuration

These correlations have been studied in early works [Léger, 1975] for the case of large amplitude roughness on metal surfaces, as well as using different polarization configurations [Knotts, 1992].

More recently, speckle correlations have also experimentally been found for surfaces with small roughness [West, 1999] following a second angular conditions (sometimes referred to as C^{10}):

$$\sin \theta_{i1} + \sin \theta_{i2} = \sin \theta_{s1} + \sin \theta_{s2} \quad (35)$$

For the case of a dielectric layer over a reflecting substrate, two recent papers theoretically addressed the problem of light scattering with slight mono-dimensional roughness at the air-

dielectric interface [Sánchez-Gil, 1997; McGurn, 1998]. They both outlined that speckle correlation could be theoretically found at new distinct angular positions due to the presence of guided waves in the transparent layer. However in practice, the order of magnitude of these correlations are usually below instrument observation capabilities. In [McGurn, 1998] it was also stated that so-called C^{10} correlation should be observable

Experimental observation of $C^{(1)}$ [Lu, 1997] with mono-dimensional roughness and $C^{(10)}$ [Gu, 1999] with 2D-roughness were reported for the case of a dielectric layer over a glass substrate, with the sample being wedge-shaped to avoid reflection from the substrate to lie in the plane of incidence.

III.1.3 Angle-resolved light scattering

When spatially integrating the intensities composing speckle patterns, a single angular intensity value is obtained. As it was stated in the first chapter of this manuscript, analysis of angle-resolved intensity distribution has been used to retrieve surface roughness parameters in the case of metallic surfaces [Vorburger, 1993; Takakura, 1996]. In that case, it is generally a monotonous intensity variation as a function of scattering angle. When a transparent layer covers the reflecting surface, circular rings may be observed as a result of interference between light scattered before entering the transparent layer and light reflected by the substrate. A first observation of the phenomenon dates back to Newton [Newton, 1952], but efforts have still been recently made aiming at a better understanding.

In [Lu, 1998], in order to explain the angular behavior of the intensity maxima, only the roughness at the air-silica interface was considered as an influencing parameter. Depending on this roughness amplitude, the maxima were found:

- (a) not to move when changing the angle of incidence (very low roughness, typically below 10nm)
- (b) to move with the angle of incidence (moderate roughness, typically ~ 100 nm)
- (c) to disappear (higher roughness amplitude)

A refined model was presented in [Kaganovskii, 1999], taking into account long range surface departure from planarity, which are equivalent to thickness fluctuations of the transparent layer. This phenomenon is of interest, keeping in mind that FHD often results in thickness fluctuations of the silica layer over horizontal scales of the order of a few mm. These thickness fluctuations were found to considerably influence the angular behavior of intensity maxima, and particularly to make them move in the roughness range of (a) case, thus creating a (d) case where the scattering behavior is similar to (b) case.

This section has presented the necessary notions to address the experimental results reported in sections 3 and 4 of this chapter. Of particular importance (because they will be checked in this study) are the angular behavior of intensity maxima (section 3) and the angular positions where speckle correlation should appear (section 4).

III.2 Experimental aspects

This section first describes the experimental set-up realized to carry out angle-resolved intensity measurement of light scattered by silica-on-silicon wafers and then continues with a presentation of these samples.

III.2.1 Experimental set-up

The general experimental configuration for angle-resolved light scattering recording or speckle study is the following. The light coming from a laser is linearly polarized before impinging the surface under investigation. A positioning system enables the choice of the angle of incidence, and angular displacement of a detector mounted on a rotating arm. The detector may be coupled with a collecting system and polarization analysis. In order to improve signal-to-noise ratio, a synchronous detection scheme (involving an optical chopper and a lock-in amplifier) may be arranged. Figure 39 illustrates this experimental configuration for the case of angle-resolved light scattering measurement using a photodiode.

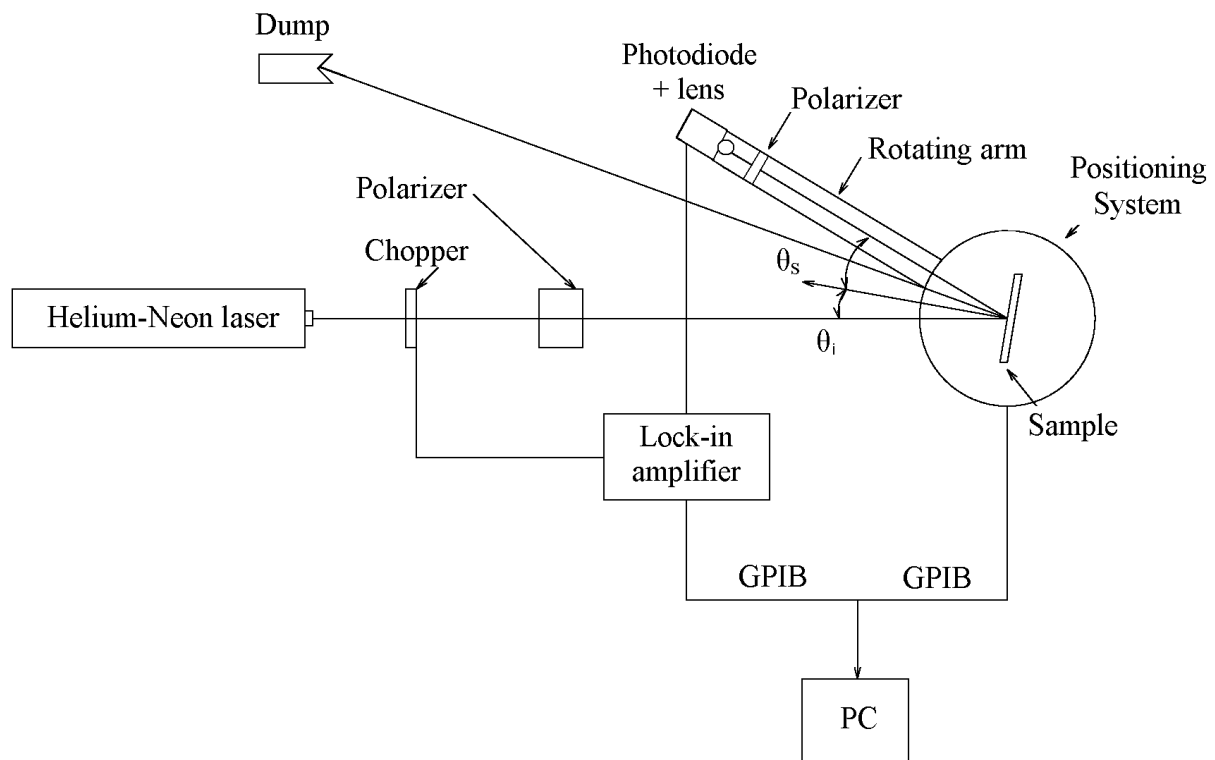


Figure 39: Experimental set-up for angle-resolved light measurement (adapted from [Takakura, 1996]).

In the initial practical implementation of the set-up, a Melles-Griot He-Ne laser emits at a wavelength of 632.8nm, with an output power after warming of 12mW, a random polarization output, and a 1mm-diameter beam. Power output stability after half-an-hour of warming was better than 1%. The laser signal was chopped at 970 Hz. Two Glan-Thomson polarizers are used, one after the chopper, and one before the collecting lens. Our positioner was an Ealing Electro-Optics Digital Positioning System, with two independent coaxial rotary stages, to be

able to both modify the incident angle and scan for light measurement. The Lock-in amplifier was a Scitec Instruments 500MC. The rotating arm was an X26 rail from Newport Micro-Control of 51.8cm. The lens was a bi-convex with a focal length of 2cm, and a diameter of 2cm. The detector was a Melles-Griot High-Speed Si photodiode, coupled with a so-called Large Dynamic Range Amplifier that provides a 10^8 transimpedance gain with a bandwidth of 1 kHz.

The two motors are controlled from a personal computer thanks to a program written under LabVIEW software. Commands are sent in the form of text lines via a GPIB link to the positioning system. The control of the lock-in amplifier is performed in the same way as for the motors, via text line commands on the GPIB link. For each light intensity measurement, the sensitivity ranges of the lock-in amplifier are scanned to determine the optimal working one. A global program ensures the coordination and synchronization of the different operations constituting the measurement.

The initial set-up for angle-resolved light scattering measurement is upgraded for speckle pattern recording. Doing so, the set (photodiode + lens) is replaced by a digital CCD camera, and the optical chopper and lock-in amplifier are removed. The speckle pattern is imaged with a scientific digital CCD camera from Hamamatsu (C4742-95-12-NRB), which outputs 1,024x1,280 pixel images with 12-bit resolution, the detector array covering an area of 8.58mm x 6.86mm at a distance of 40cm from the sample. The resulting speckle grains cover approximately 20-30 pixels, and each image has consequently more than 3,000 grains. As in the initial set-up, the motors and the camera are controlled by a computer via a program running under LabVIEW software. Integration time with the camera is varied to optimize image contrast and limit pixel saturation. Figure 40 represents the experimental set-up upgraded for angle-resolved speckle pattern recording.

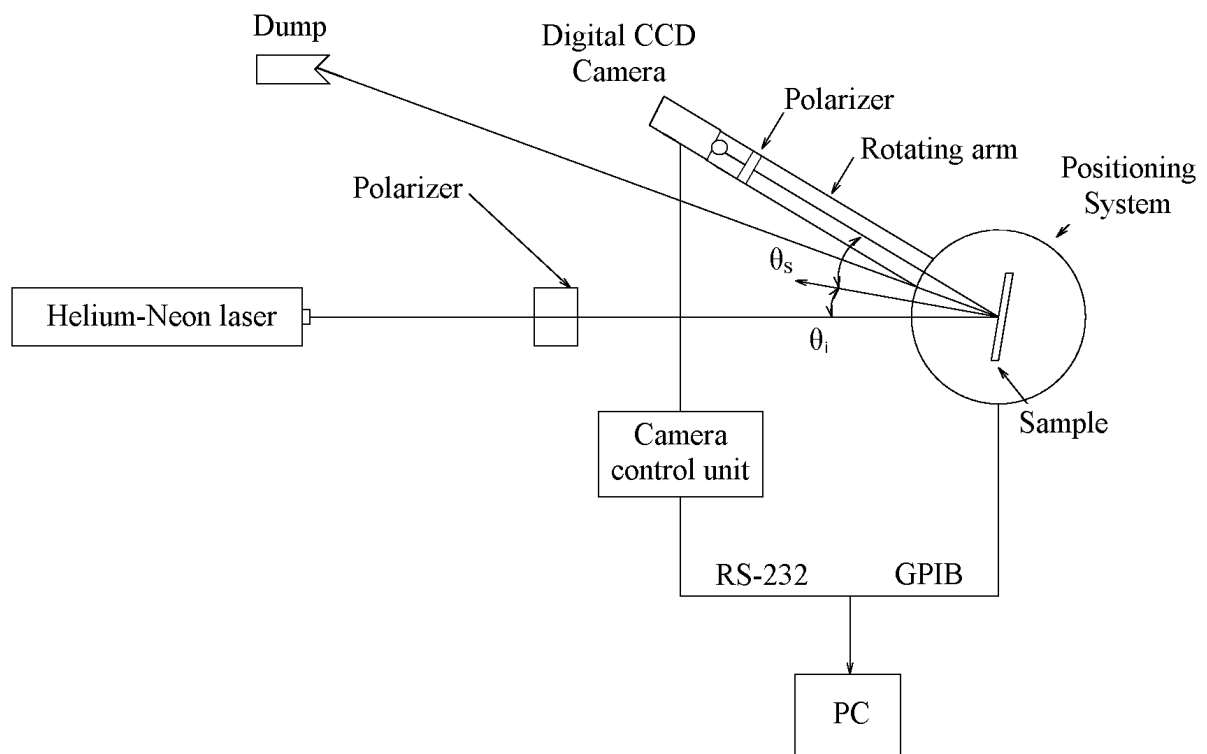


Figure 40: Set-up for angle-resolved speckle pattern recording.

A typical image is displayed on Figure 41, along with the histogram of pixel intensity values, the dark noise of the CCD camera resulting in an upward shift in pixel values from the expected theoretical curve [Dainty, 1984].

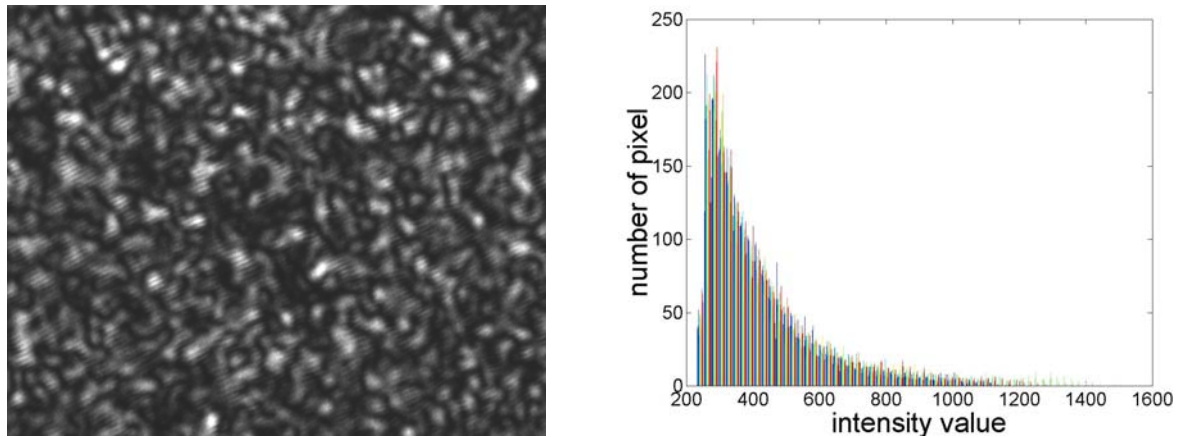


Figure 41: Typical speckle pattern (left) and histogram of pixel intensity data (right).

Angle-resolved intensity measurements were also carried out by summing pixel intensity values over a whole image for a given angular position, and then plotting this value as scattering angle varies.

Difficulties in carrying out measurements:

There are several issues in carrying out angle-resolved light intensity measurement or speckle pattern recording.

Alignment [Knotts, 92] is a critical issue in this experiment. Of particular importance is the alignment of the incident laser beam with the rotation axis of the concentric rotation motors. The plane of the surface under study also has to contain the rotation axis, to avoid illuminating different sample areas when rotating the sample. The detector has to be aligned with the rotation arm. Essential initial precaution consists in careful design of the mechanical part composing the set-up, such as sample-holder. For instance, a special mechanical part was designed to ensure the CCD camera remains aligned with the rotation arm, and is displayed on Figure 42.

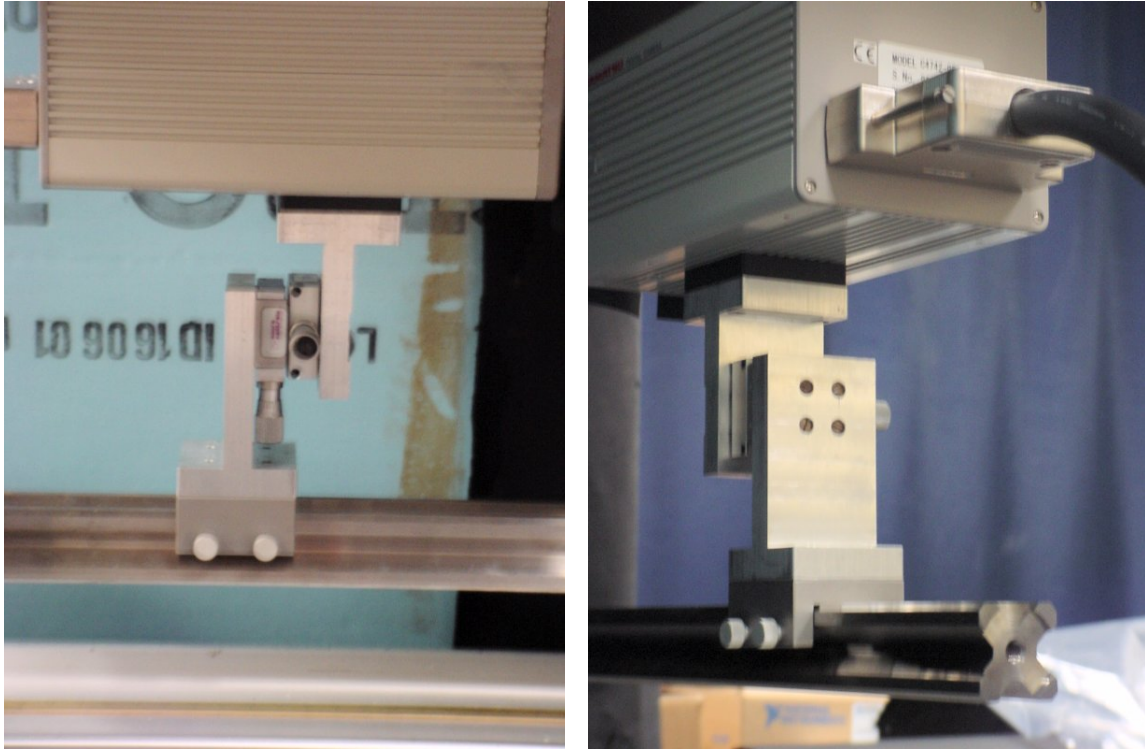


Figure 42: Mechanical part to ensure alignment of CCD camera with rotation arm.

Noise comes mainly from light external to the experiment. The room of the set-up was turned as dark as possible, and the set-up itself covered by black paper. The set-up with lock-in amplifier and photodiode had the additional advantage of performing synchronous detection.

When carrying out intensity measurement over a large angular path, the mean intensity of scattered light may vary significantly. Particularly, this can lead in the two extreme situations to pixel saturation or to too low signal-to-noise ratio. It is therefore of prime importance to check these variations on the full angular range inspected. Using the photodiode and lock-in amplifier, this was done by testing that the lock-in operates in its linear regime for every measurement. With the CCD camera, this was performed by looking at the histogram of speckle patterns for uttermost images of the angular scanning.

Finally, when dealing with polarization [Knotts, 92], determination of the angles of polarization remains of importance.

III.2.2 Description of the samples

In a first phase, three samples are investigated: sample A is a silicon wafer covered by a 325nm thermal oxide; in comparison with sample A, sample B contains an additional 5.8 μ m-thick silica layer deposited by FHD; sample C is a Si wafer covered by a thermal oxide and a FHD layer of respective thickness 15.8 μ m and 5.7 μ m. The refractive index of FHD layer for $\lambda = 633$ nm is $n = 1.46$, and 1.44 for thermal oxide. The roughness at the air-silica interface was visually inspected with a scanning electron microscope (SEM) LEO Gemini 1550, with the sample normal making a 45° angle with the incoming electron beam. This instrument has a resolution of 2nm for an operating voltage of 1.5kV. The roughness was found to be

constituted of isolated residual defects of the order of a few tens of nanometers, which could be considered as 2-dimensional. Figure 43 illustrates this surface aspect for sample C.

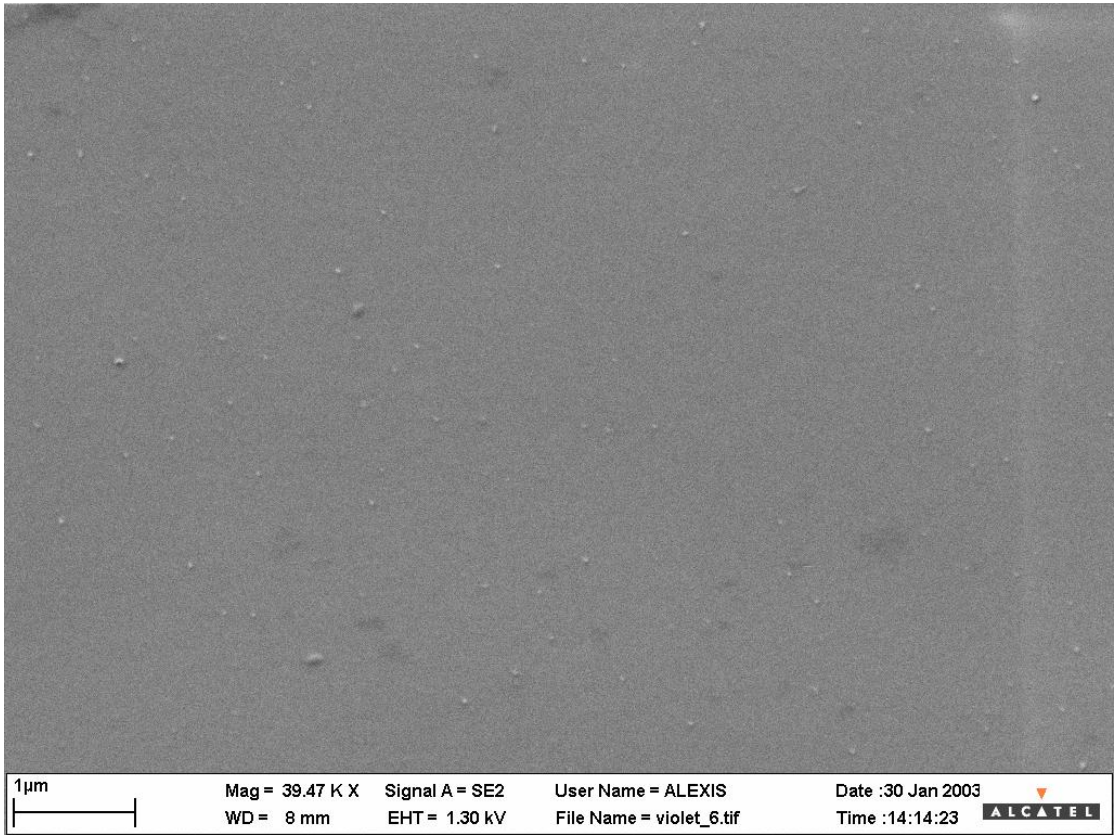


Figure 43: SEM image of sample C.

Additional samples were then provided, consisting of a single silica layer on top of a Silicon substrate. The samples differ from each other with their thickness fluctuations. These thickness fluctuations were inspected with an interferometric microscope. The instrument could reach a vertical resolution of 1nm, and 405 points were measured on the whole wafer surface. A typical result is presented on Figure 44, where the thickness fluctuations for sample M1_1548_1 are plotted.

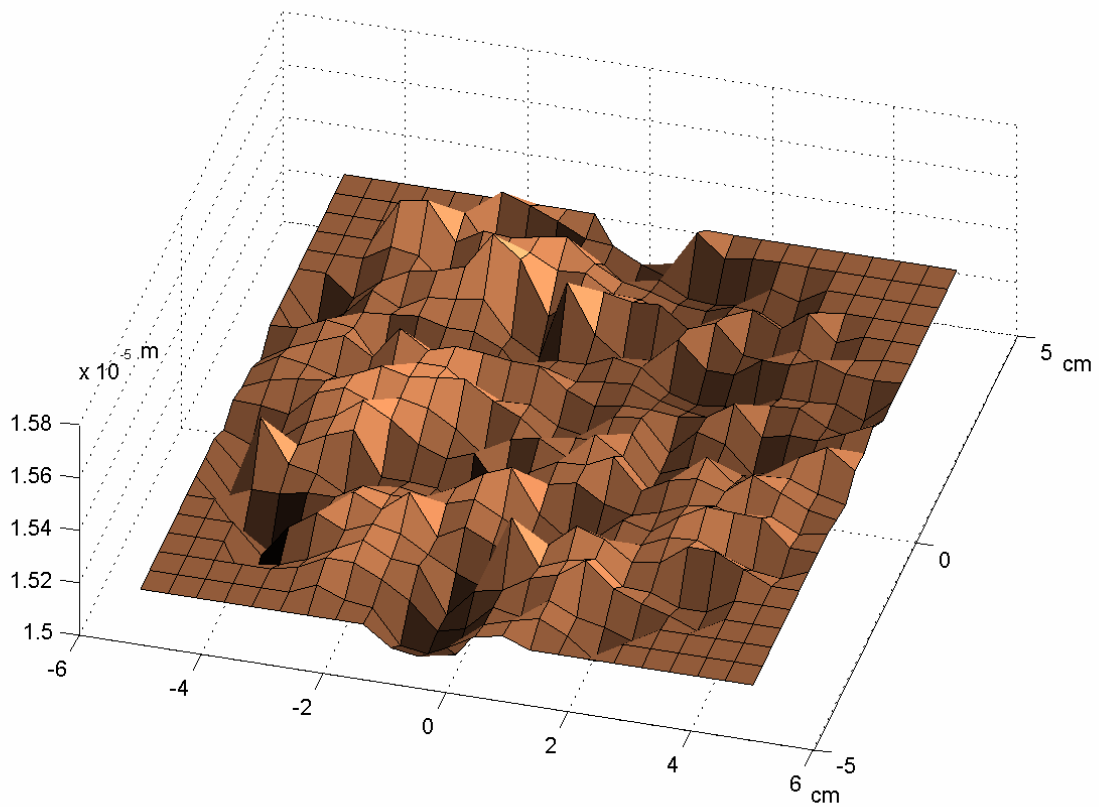


Figure 44: Thickness fluctuations for sample M1_1548_1.

The following table summarizes the principal characteristics for the samples employed in this work. The parameter δt is defined as in [Bulla, 2004]: $\delta t = (t_{\max} - t_{\min}) / (t_{\max} + t_{\min})$, where t_{\max} and t_{\min} are respectively the maximum and minimum thickness values over the whole wafer.

Reference	Mean Thickness (μm)	Thickness fluctuation amplitude (nm)	δt (%)	Thickness standard deviation (nm)	Remark
TO (A)	0.32	Similar to TO_3	NA	NA	TO
M1 (B)	6.1	Similar to M1_1544_1	NA	NA	TO + SiO ₂
V0 (C)	21.5	NA	NA	NA	TO + SiO ₂
Si	0	NA	NA	NA	Si(100)
TO_3	3.1	≤ 10	≤ 0.15	1.4	TO
M3_117_3	5.5	50	≤ 0.6	4.3	
¹ M1_1544_1	5.7	220	2.0	40	
M1_1548_1	15.2	450	1.5	64	Cf. Figure 44
TO_15	15.5	260	≤ 1.0	61	Cf. Footnote ¹
M3_101_1	20.0	740	1.9	85	

Table 6: Samples used for angled-resolved light scattering and speckle correlation studies.

¹The values for sample TO_15 are somehow confusing, comparing to the actual thickness variation distributions. Indeed, more than half of the wafer presents thickness variations of which the amplitude is below 40nm.

This section has presented the set-up realized for angle-resolved light scattering and speckle correlation studies with a wavelength of 632.8nm. At this wavelength, the samples assessed can be considered as a transparent layer over a reflecting substrate, with roughness of the order of a few tens of nanometers at the air/dielectric interface, thickness fluctuations of various amplitudes, and negligible roughness at the dielectric/substrate interface. Next section investigates the angle-resolved light properties of these samples. It also constitutes a test of the measurement system, in an attempt to obtain results available in literature.

III.3 Angle-resolved light scattering

This section first reports experimental observations related to diffused fringes as described in [Lu, 1998; Kaganovskii, 1998 & 1999]. It is then shown how one may retrieve silica layer's thickness from angle-resolved light intensity measurements. As a perspective, two experimental approaches aiming at thickness fluctuation evaluation for silica-on-silicon samples are presented.

III.3.1 Diffused fringes

As a first step, in order to validate both the experimental set-up and the frame of study for these samples, the angular intensity oscillations predicted in the first section of this chapter are looked for, as well as their behavior as a function of the angle of incidence

Angle-resolved intensity measurements:

The set-up containing a photodiode and a lock-in amplifier is used for the results of this section. Figure 45 gives the general shape for the curves recorded with the light scattering measurement set-up. Here the angle of incidence is set to 5° , and the reflected beam is consequently at 5° . Thus the curve shows its envelope around the specular direction. At 5° , the system is blind and gives meaningless values. This is because the gain provided by the transimpedance amplifier (10^8 V/A), fixed to get data at large angles, makes the signal overpass the upper limit in detection enabled by the lock-in amplifier.

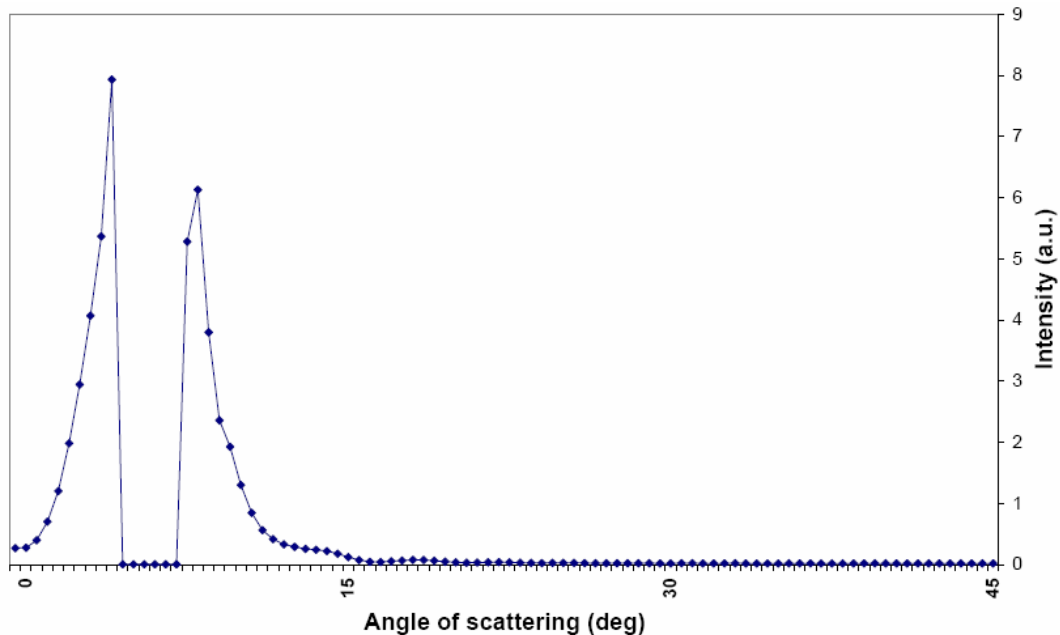


Figure 45: Overview of angle-resolved scattered intensity for sample C, $\theta_i = 5^\circ$.

By decreasing the transimpedance gain down to 10^6 V/A, information on the specular beam can be obtained. Its order of magnitude is found to be 10^4 times greater than at large angles

(typically 30°). This order of magnitude is characteristic of surface roughness in the nanometer domain [Takakura, 1996].

When zooming the previous curve at large angles, intensity oscillations are detected. Figure 46 represents angle-resolved light intensity measurement performed with $\theta_i = 5^\circ$ for samples B and C. The curve for sample B is shifted upward for clarity.

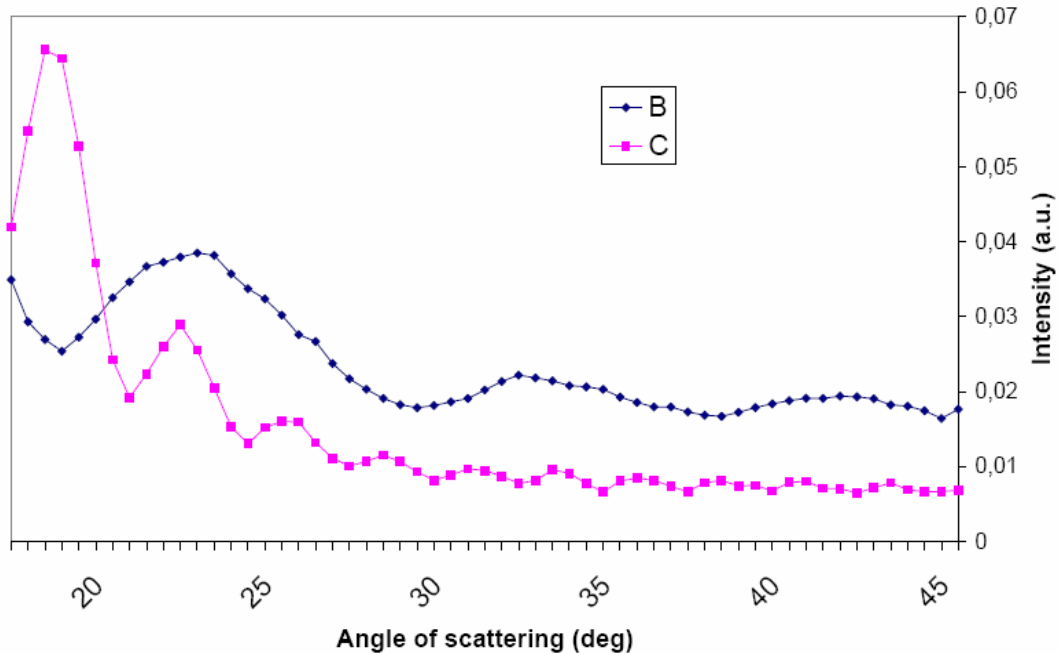


Figure 46: Angle-resolved intensity measurement for sample B and C, $\theta_i = 5^\circ$.

As detailed in the first section of this chapter, theoretical predictions [Lu, 1998] lead to the presence of intensity oscillations as a function of scattering angle. As stated, the periodicity of these oscillations depends on the refractive index and thickness of the transparent layers involved, which can be experimentally noted when comparing results with sample B and C. These oscillations are said to be the one-dimensional projection of rings centered around the sample's normal [Lu, 1998], and are thus expected to be symmetrical with respect to sample's normal when measured in this work. Figure 47 shows the angle-resolved intensity oscillations for sample B, both obtained with $\theta_i = 5^\circ$, and by scanning successively in the forward and backward directions. Measurements in the backward direction, thus corresponding to negative scattering angles, are plotted with the absolute value of their x -coordinate to enable direct comparison with measurements in the forward scattering direction.

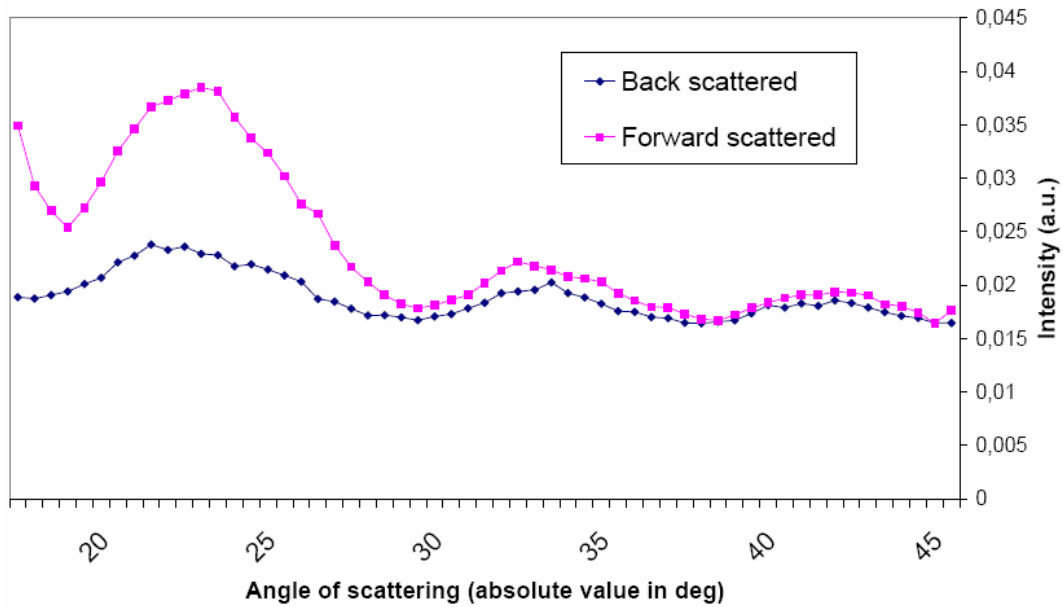


Figure 47: Forward and back scattered angle-resolved intensity for sample B.

As it can be noticed, the position of intensity maxima is symmetrical with respect to sample's normal. As it was also predicted, the global intensity is higher in the forward than in the backward direction.

A key question in light scattering from a transparent layer over a reflecting substrate is the behavior of these intensity maxima's position as a function of angle of incidence [Lu, 1998; Kaganovskii, 1999]. Figure 48 represents the curves obtained with sample C for an incident angle of 10° (lower), and 5° (upper, multiplied by 6 for clarity).

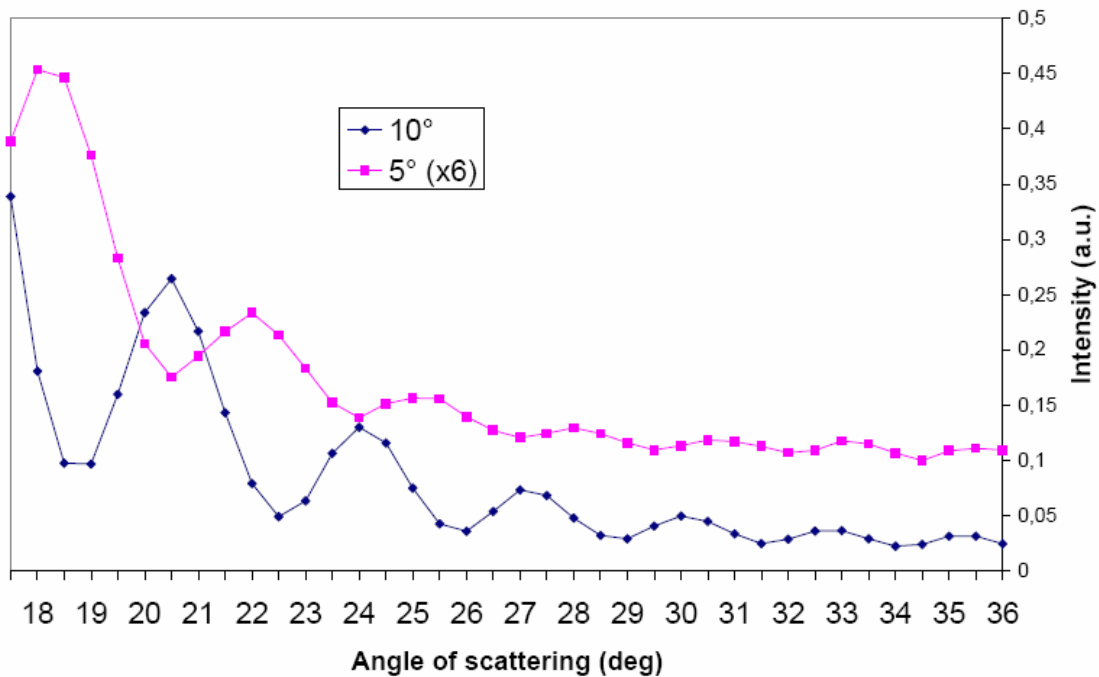


Figure 48: Angle-resolved intensity for sample C, with $\theta_i = 5^\circ$ (upper) and $\theta_i = 10^\circ$ (lower).

For the samples assessed in this study, the maxima were found to have a behavior as described in [Lu 1998] for the case of moderate roughness. The global intensity scattered at large angles is found to increase when increasing the angle of incidence.

Finally, when considering sample A, due to the relative small thickness of the transparent layer, no intensity oscillations are observed, but a slow decrease when going towards large scattering angles. This is measured both in forward and backward directions, with a global intensity higher in forward direction.

Comparison with results reported in literature:

Such an experimental observation had been reported for similar samples consisting, for the wavelength of study, in a transparent layer over a reflecting substrate in three recent papers [Gu, 1996; Kaganovskii, 1998 & 1999].

In [Gu, 1996], results are reported for a 5.2 μm thick Teflon layer covering an aluminium substrate. The roughness present on the top surface had an RMS height of 6nm and a correlation length of 300nm. The authors observed the angle-resolved intensity oscillations symmetrically located with respect to sample's normal. The global intensity was found to be higher in the forward scattering direction, and, for a fixed scattering angle, the intensity was measured to increase as the angle of incidence increased (and consequently as the specularly reflected beam gets closer), as illustrated on Figure 48. The authors were mainly focused on quantifying enhanced backscattering peaks, and although they had known the theoretical work to be presented in [Lu, 1998] (their Ref. 16), they did not yet stress the fact that the intensity oscillations reported were moving with the angle of incidence. This result is however somehow in contradiction with the predictions for "slight roughness" in [Lu, 1998], considering the sample's roughness claimed.

Such a dilemma is addressed in [Kaganovskii, 1998 & 1999], where samples with roughness of the order of 50-100nm are investigated. As written in the first section of this chapter, some of them possessed additional long scale roughness, assimilated to thickness fluctuations. The main effect induced by these fluctuations was the move of angle-resolved intensity oscillations when changing the angle of incidence. Such a move was not observed for samples lacking long scale roughness. The other results presented in these works are conform to the previous observations reported in this section.

One may now rise the question on which information can be extracted from these intensity oscillations. As an effort to answer this question, it is shown in next section, how the thickness of the transparent layer may be retrieved from the angular position of intensity maxima.

III.3.2 Thickness retrieval

It was experimentally evidenced in the previous section that the thickness of the transparent layer contributes (along with its refractive index and the laser wavelength) to define the intensity maximum positions. On the other way, knowing the wavelength of study and the refractive index of the transparent layer, it is also possible to obtain the thickness of the transparent layer. Thickness values are here calculated using the intensity maximum positions of Figure 46, and then compared to values measured independently by Alcatel's engineers using interferometric or ellipsometric set-ups.

Theoretical considerations:

We will refer to [Lu, 1998] in this study for several reasons. First, the materials they used in their work is sometimes similar to ours (SiO_2 layers on Si) with order of magnitude for the thickness of the layers comparable (several microns). The second reason is that they observe similar features with light scattering measurements, that-is-to-say angular intensity variations, that depend both on the layer thickness and on the angle of incidence.

According to [Lu, 1998], for a dielectric layer on a perfectly reflecting substrate, with a “moderate” roughness on the air-dielectric interface, the position of the fringes is described by the following relation

$$2nd(\cos\theta_{d0} - \cos\theta_{ds}) = m\lambda \quad (36)$$

where d is the layer thickness, n the refractive index of the layer, λ the wavelength of the incident beam, m the order of interference for the fringe considered, θ_{d0} and θ_{ds} are related to the incident and scattering angles θ_0 and θ_s by the relations

$$n \sin \theta_{ds} = \sin \theta_s \quad \text{and} \quad n \sin \theta_{d0} = \sin \theta_0 \quad (37)$$

Here the term "moderate" refers to roughness in the range of 100nm, which is in good agreement with the samples investigated.

Thickness estimation results:

As a first approximation, we consider the refractive index of the thermal oxides and of the FHD layers to be equal to the one of the layers. By considering equation (36) for two consecutive intensity maxima, and by dividing them term-by-term, it is possible to calculate the order of interference for the first visible maximum. According to [Lu, 1998], there is always an intensity maximum linked to the specular beam, and this fringe constitutes the zero-order fringe. Consequently, we expect small numbers for the orders of interference of the visible maxima.

The first maximum for sample C is found to have an order $m = 2$, whereas for sample B it has an order $m = 1$. This is in good agreement regarding the “angular frequency” of appearance of the fringes. Indeed, because the fringes are closer to one another for sample C, and considering their global intensity with respect to the specular beam, it is likely that the first order fringe is hidden by the specular beam.

Knowing the order of interference and refractive index, it is possible to retrieve the layer thickness. To do so, we assumed the order of interference to be unknown, but small, and computes the thickness using as many maxima as available, as displayed on Figure 46.

Figure 49 shows such a calculation for sample C.

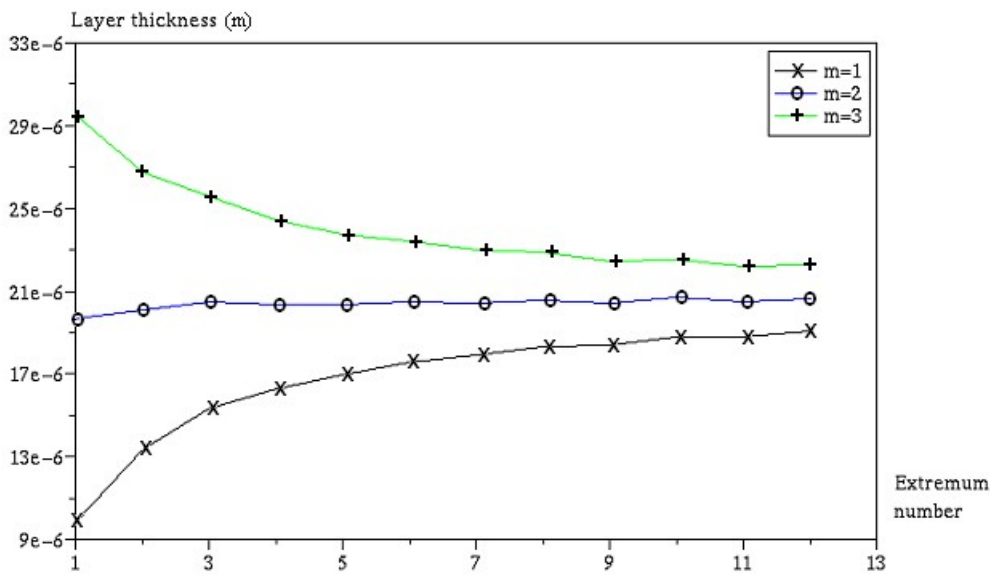


Figure 49: Thickness estimation for sample C.

On the y -axis is the layer thickness, and on the x -axis the number of the maximum considered. Twelve maximum positions were used for Figure 49. m in the legend of Figure 49 refers to the order of interference of the first visible fringe. It can be noticed that when the order of interference is over- (or under-) estimated, then the formula gives different values for the set of maxima. When considering the right order of interference, values around $20.6\mu\text{m}$ are found, which is in good agreement with the reference data. This result has been obtained both with incident angles of 5° and 10° .

Figure 50 shows the same calculations for sample B.

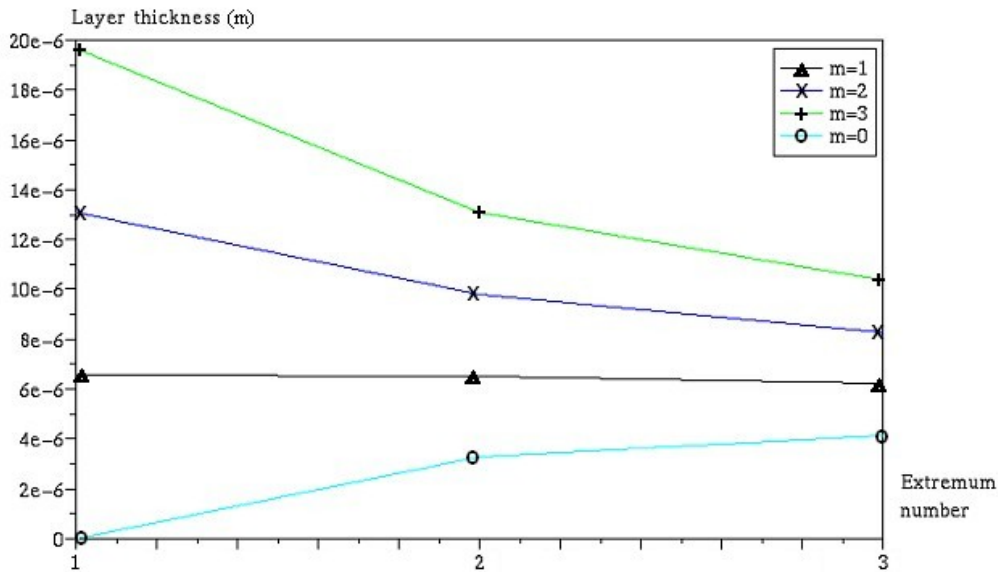


Figure 50: Thickness estimation for sample B.

The maxima on the scattering curve being more spaced than for sample C, only three points have been used for this sample. Again it is found that with the correct order of interference for the first visible fringe, the value retrieved for the thickness (around 6.4 μm) is in good agreement with the reference value.

Discussion:

The technique provides satisfying estimation of the layer thickness. However, several limitations restrain the interest of the method. First, the refractive index of the transparent layer has to be known, as the system of equations involved only enables solving one unknown (refractive index or thickness) in a direct way. Secondly, the difference in refractive index between the different transparent layers has to be small enough so that the set of layers may be assimilated to a single transparent layer, or the system should contain only one transparent layer. Finally, the angle-resolved scattering pattern must present intensity oscillations, what sets a minimal thickness accessible, depending on the working wavelength.

The purpose of this work on thickness retrieval was to validate the concept of thickness evaluation via measurement of angle-resolved scattered light intensity. This brings more confidence in the angle-resolved light measurements themselves coming from the experimental set-up built for this doctoral work. Developments are still required before having the technique as a well characterized measurement procedure or prototypal apparatus. There exist several optical techniques for thickness measurement, and comparative potential breakthrough should be assessed before dedicating more effort in the angle-resolved light measurement approach. Among competing techniques are, just to name a few, confocal microscopy, reflectometry, ellipsometric and interferometric measurements. One of the definite advantage of the light scattering approach is the simplicity of the model for calculation, coupled with a relatively simple experimental set-up. The main drawbacks are the time required to carry out the angular scan, as well as the range of thickness available. The technique may however constitute an interesting alternative to already existing techniques.

III.3.3 Grazing angle approach

The precedent section provided an alternative method for thickness measurement in the case of a transparent layer on a reflecting substrate. A typical problem however with flame hydrolysis deposition is the presence of thickness inhomogeneity for the silica layer. These thickness fluctuations should be as low as possible, as they will thereafter be translated into waveguide's size fluctuation, and may contribute to propagation loss.

Common ways to estimate these thickness fluctuations are multiple, and were described in chapter 1 of this thesis. One may think of using an interference microscope (as it was the case for the samples presented in section 2 of this chapter) or a confocal microscope.

The purpose of this section and of next section is to discuss two potential approaches for estimating these thickness fluctuations using the already available angle-resolved light scattering set-up. The present state of advancement of these works limits these sections to a discussion on potential results, but it is hoped that further developments will bring interesting conclusion in a near future.

Background, published related works, and motivations:

The increase of the angle of incidence may appear a natural continuation of angle-resolved light scattering studies in the perspective of completeness. However, practical measurements at large angles of incidence are challenging, essentially because the illuminated area on the surface becomes huge [Gu, 2002b]. For this reason, even detailed experimental studies on angle-resolved light scattering are often limited to angle of incidence up to 60° or 70° [Ruiz-Cortés, 2002].

In order to investigate the proportionality between speckle contrast and roughness in the small amplitude roughness domain, Leonard and Toal [Leonard, 1998] used an angle of incidence of 80° . This technique enables extending the range of the speckle contrast roughness measurement method up to $0.4\mu\text{m}$ RMS roughness for the case of metallic surfaces.

For the case of a transparent layer on a reflecting surface, experimental evidence has been given of the importance of thickness fluctuations for the transparent layer on the angular light intensity distribution [Kaganovskii, 1999]. For the case of moderate roughness, as it is the case for the samples in this study, the light-surface interaction phenomenon can be assimilated to a single scattering event followed by multiple successive reflections on the boundaries constituted by the interfaces air/dielectric (here air/silica) and dielectric/reflector (here silica/silicium) [Blumberg, 2004]. It is thus interesting to remark, as was stated in [Gu, 2004a], that the influence of thickness fluctuations would be more important for an incident laser beam at grazing angle. Indeed, in this geometrical configuration, the reflections at the interfaces would become the dominant phenomenon. The authors [Gu, 2002b & 2004a] then investigated the backscattering enhancement of a sample with RMS roughness of 6nm (cf. Annex D) and an average thickness of $5.2\mu\text{m}$ for an angle of incidence of 89° . There is no mention however on the amplitude of thickness fluctuation for their sample, and no comparison for samples with different thicknesses.

It should thus be possible to get comparative information for samples with different thickness fluctuations by comparing their angle-resolved light intensity distribution for grazing angle of incidence.

Experimental considerations:

Four samples are used for this study : M3_117_3 and M1_1544_1, having respectively thickness fluctuations amplitude of 50nm and 220nm, and similar mean thickness (5.5-5.7 μ m), and samples TO_15 and M1_1548_1, having respectively thickness fluctuations amplitude of 40nm and 450nm, and similar mean thickness (15.5-15.2 μ m).

The angle of incidence is fixed to 80°. Scanning is carried out from 50° to -72°. Specular beam is trapped with a dump to avoid stray reflection. The general speckle texture is as depicted on Figure 51. False colors are employed to indicate high intensity areas (bright) and low intensity ones (dark).

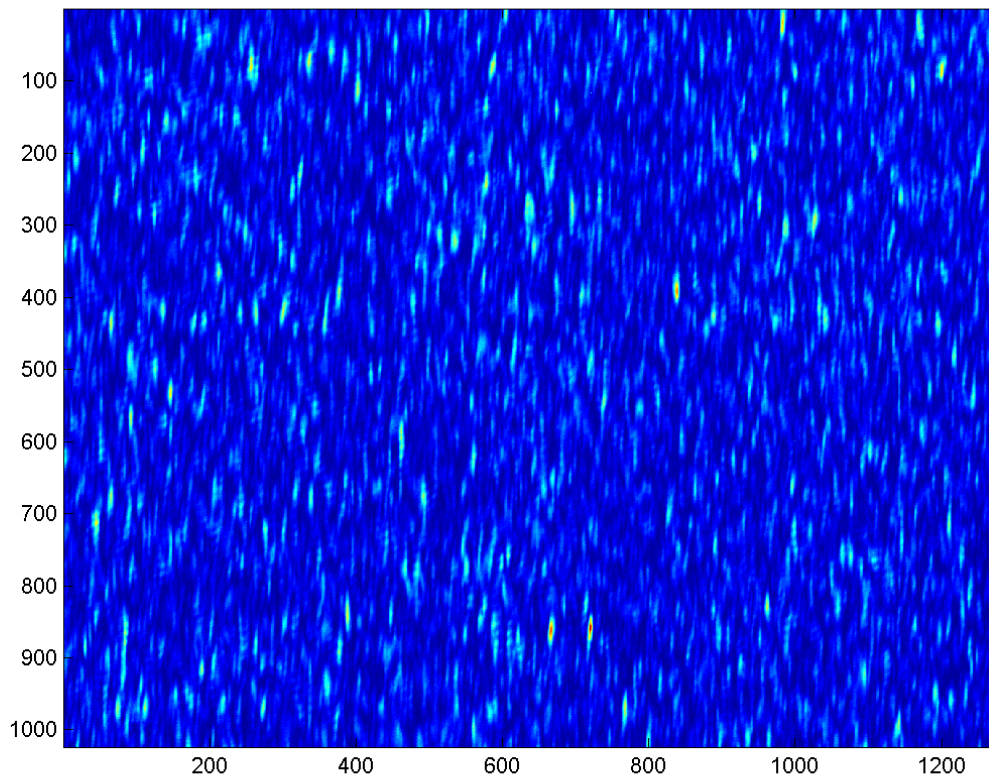


Figure 51: Speckle pattern obtained with an angle incidence of 80°.

This elongated aspect is caused by the illumination conditions. Due to the large angle of incidence, the illuminated area on the sample takes the form of an elongated ellipse. One reminds [Born & Wolf, p. 444] that the central far-field diffraction pattern of an elliptical aperture has the form of an ellipse of which the major axis is perpendicular to the high axis of the aperture. Considering as stated in [Briers, 1993] that the objective speckle granular shape is related to the far-field diffraction pattern of an aperture having the same aspect as the surface's illuminated area (here an ellipse), this feature comes as no surprise.

This elongated aspect can be used as a criterion to check the consistency of the obtained speckle patterns.

III.3.4 Retrodiffusion approach

Background:

The angle-resolved light scattering curves presented intensity oscillations in the plane of incidence, with the position of the intensity maxima varying when changing the angle of incidence. At the wavelength of investigation ($\lambda = 633\text{nm}$), the samples can reasonably be assimilated to a transparent layer (silica + thermal oxide) over a reflecting substrate, the upper layer presenting 2D roughness in the nanometer range. The positions of the intensity maxima when changing the angle of incidence were found in good agreement with the theoretical model provided in [Lu, 1998].

As a reminder, we recall the four diffused fringes' angular behavior evoked in the first section of this chapter. The fringes were found:

- (a) not to move when changing the angle of incidence (very low roughness, typically below 10nm)
- (b) to move with the angle of incidence (moderate roughness, typically $\sim 100\text{nm}$)
- (c) to disappear (higher roughness amplitude)
- (d) similar to (b) (low roughness coupled to thickness fluctuations)

Laser light retroreflection:

Light retroreflected corresponds to light back-scattered from the surface in the direction of the incoming laser beam. Except in (a) case, where the angular intensity maxima are fixed with respect to sample's normal, the other cases lead to the presence of non-null light intensity value in the retroreflection direction. For the cases (b) and (d), this is due to the presence of a diffuse fringe, for case (c), to the presence of the backscattering peak.

In a recent paper [Blumberg, 2002], it was highlighted that thickness fluctuations play a dominant role in the amplitude of light retroreflected from a transparent layer over a reflecting substrate. When varying the angle of incidence, and keeping the observation at the direction of the impinging laser beam, i.e. $\theta_i = \theta_s$, it is theoretically possible to observe oscillations in intensity. Figure 52 illustrates this theoretical prediction.

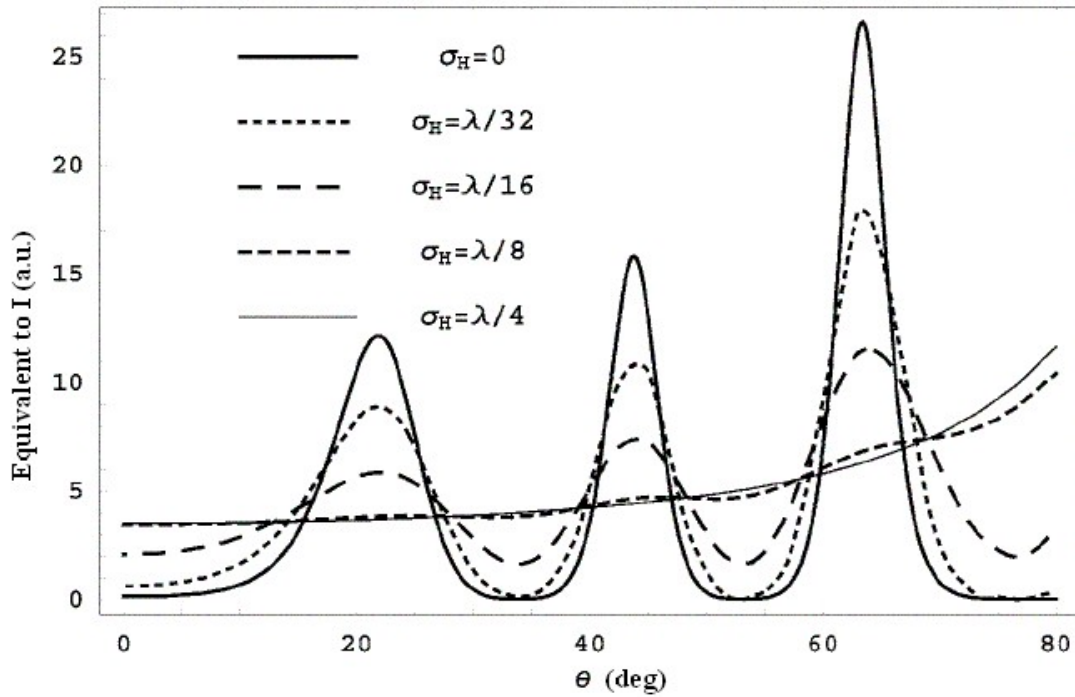


Figure 52: Retroreflection as a function of the angle of incidence for different thickness fluctuation amplitudes σ_H (from [Blumberg, 2002]).

It can be noticed that depending on the amplitude of thickness fluctuations σ_H , the contrast of these oscillations in intensity varies. The contrast is maximum in the absence of thickness fluctuations and tends to zero for thickness fluctuations getting close to $\lambda/4$.

Figure 53 contains experimental verification of this phenomenon taken from [Blumberg, 2002].

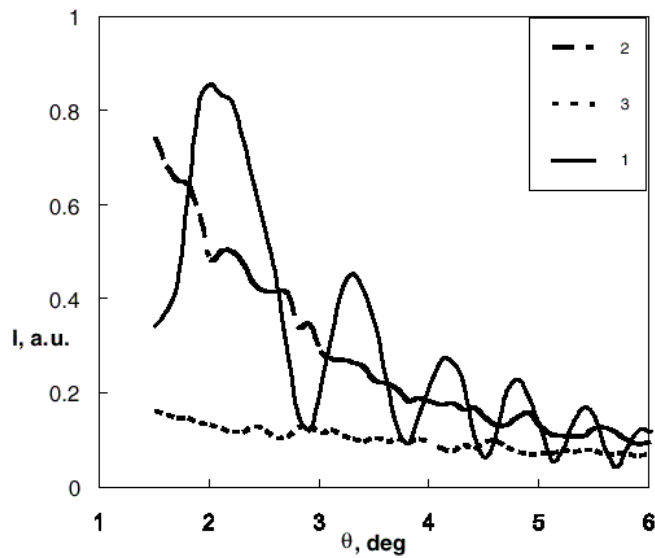


Figure 5. Backscattering from a Fabry–Perot plate (1), thin regular layer (2) and semi-infinite dielectric (3) with the same rms height of short-scale roughness.

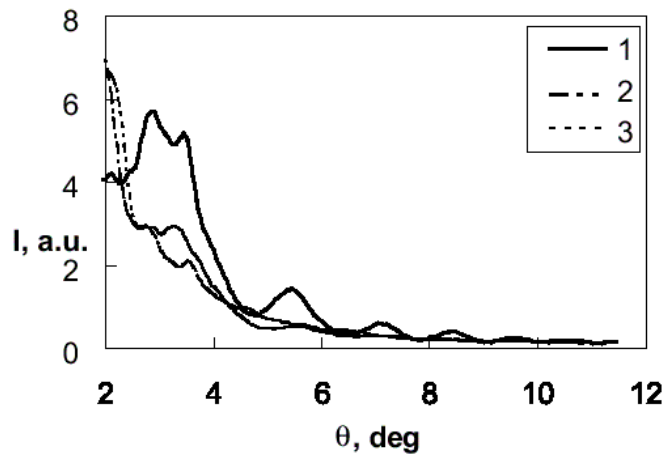


Figure 6. Backscattering from glass plates with different long-scale variations of the thickness σ : 1— $\sigma = \lambda/15$; 2— $\sigma = \lambda/10$; 3— $\sigma = \lambda/2$.

Figure 53: Two experimental sets of retroreflections curves from [Blumberg, 2002].

The experimental study carried out in [Blumberg, 2002] shows encouraging results. One could therefore think about using the angular intensity variations of the retro-reflected light as a tool for thickness fluctuation inspection.

The objectives of future work could be, first, to observe these oscillations as a function of the angle of incidence (keeping $\theta_i = \theta_s$), and then to try to correlate them with different amplitudes of silica thickness fluctuations assessed by white light interferometry.

In this section, experimental angle-resolved light scattering curves were displayed for silica-on-silicon samples. The intensity maximum positions were found in agreement with theoretical predictions from [Lu, 1998], which in return enabled thickness evaluation of silica layer. Two proposals for assessing fluctuations of these thickness values have been presented. Next section will now discuss angular speckle properties for these samples.

III.4 Speckle correlations

This section begins with a reminder of the practical principles for recording speckle patterns and evaluating their correlation. The $C^{(l)}$ is then explored for three samples looking at the reciprocal scattering configuration, its departure from so-called memory effect, and its appearance in the presence of diffused fringes. Issues noticed at this first step can be explained by looking at the two-dimensional cross-correlation between two speckle patterns. Finally, efforts to observe $C^{(l0)}$ correlation are reported and discussed.

III.4.1 Principles of speckle pattern recording and of correlation evaluation

Speckle pattern recording:

The speckle pattern is obtained by direct illumination of the CCD camera, without the use of an optical objective, this situation corresponding to a so-called objective or far-field speckle pattern. This approach experimentally differs from previous similar experiments [Lu, 1997; Gu, 1999].

Correlation evaluation:

When a first speckle pattern $I(\theta_{i1}, \theta_{s1})$ is recorded using illumination and observation angles θ_{i1} and θ_{s1} respectively, its correlation coefficient with a second image $I(\theta_{i2}, \theta_{s2})$ obtained for angles θ_{i2} and θ_{s2} is given by [Lu, 1997]:

$$C(\theta_{i1}, \theta_{s1}; \theta_{i2}, \theta_{s2}) = \frac{\langle I(\theta_{i1}, \theta_{s1}) I(\theta_{i2}, \theta_{s2}) \rangle - \langle I(\theta_{i1}, \theta_{s1}) \rangle \langle I(\theta_{i2}, \theta_{s2}) \rangle}{\left[\left(\langle I(\theta_{i1}, \theta_{s1})^2 \rangle - \langle I(\theta_{i1}, \theta_{s1}) \rangle^2 \right) \left(\langle I(\theta_{i2}, \theta_{s2})^2 \rangle - \langle I(\theta_{i2}, \theta_{s2}) \rangle^2 \right) \right]^{\frac{1}{2}}} \quad (38)$$

where the symbols $\langle \dots \rangle$ imply averaging over the pixels composing the images. In what follows, this parameter C is represented as a function of θ_{s2} for fixed values of the other angular parameters.

A maximum in the correlation function is observed when the following angular condition is satisfied [McGurn, 1998; Sánchez-Gil, 1997]:

$$\sin \theta_{i1} - \sin \theta_{s1} = \sin \theta_{i2} - \sin \theta_{s2} \quad (39)$$

which leads to the observation of short-range intensity correlations. As stated in section 1 of this chapter, the two main manifestations of these correlations are visible when departing from the initial angle of incidence while keeping Equation (39) satisfied (sometimes referred to as "memory effect") and in the reciprocal scattering configuration (sometimes referred to as time-reversed memory effect).

III.4.2 Experimental angle-resolved speckle correlations

An exploring experimental study [Bony, 2003] was conducted to have a global idea of samples' properties in terms of speckle correlation. This section starts looking at speckle correlation for a special case of $C^{(l)}$ angular condition denoted reciprocal scattering configuration. This scheme is expected to lead to significant correlation values, due to the reciprocity nature of electromagnetic scattering [Saxon, 1955]. It constitutes thus a good test of the whole set-up as well. $C^{(l)}$ angular condition is then looked for in the case where θ_{i2} slightly departs from θ_{i1} [Léger, 1975]. The last point of this section deals with the presence of diffused fringes as mentioned in section 3 of this chapter, and how they may deteriorate speckle correlation evaluation.

Reciprocal scattering configuration:

In the particular case where $\theta_{i2} = -\theta_{s1}$, a peak of correlation is detected in the direction of observation for $\theta_{s2} = -\theta_{i1}$, in agreement with Eq. (39). This peak arises from the reciprocal scattering condition. Taking values of $\theta_{i1} = 10^\circ$, $\theta_{s1} = 0^\circ$, $\theta_{i2} = 0^\circ$, and scanning θ_{s2} around the value of -10° expected from Eq. (39), a peak of correlation is observed for all the three samples both for s-s and p-p polarization configurations. However, all configurations lead to maximal values for the peak of correlation ranging from 0.5 to 0.8 depending on sample and polarization. In [Gu, 1999], the difference between the correlation peak value and unity was attributed to experimental alignment. A technique similar to the one presented in [Lin, 1997] was used to account for angular misalignment by numerically matching the two speckle patterns considered to obtain the maximum value of correlation achievable. These values remained yet well (0.8) below unity. When changing θ_{i1} to $\theta_{i1} = 15^\circ, 20^\circ, 30^\circ$, the maximal value of the correlation peak decreased and the peak tended to slightly broaden.

Figure 54 illustrates this observation for sample A, with s-s polarization. Comparison of the two speckle images that should present the maximum of correlation for $\theta_{i1} = 30^\circ$ revealed a change in the size of the speckle grains and in the global scale of the pattern. As the observation system is in a non-imaging configuration (no optical objective, nor lens, before the receiver), the average size of the speckles is approximately the one of an Airy task produced by a circular aperture having the diameter of the illuminated area on the sample [Briers, 1993]. Consequently, when increasing the angle of incidence, the illuminated area becomes larger, and the speckle grains smaller than at normal incidence. Nevertheless, the two speckle patterns considered are still visually similar, thus confirming the presence of the time-reversed memory effect, even for large incident angles. However, due to the direct point-to-point correlation calculation, the correlation values are found to decrease with growing angles of incidence.

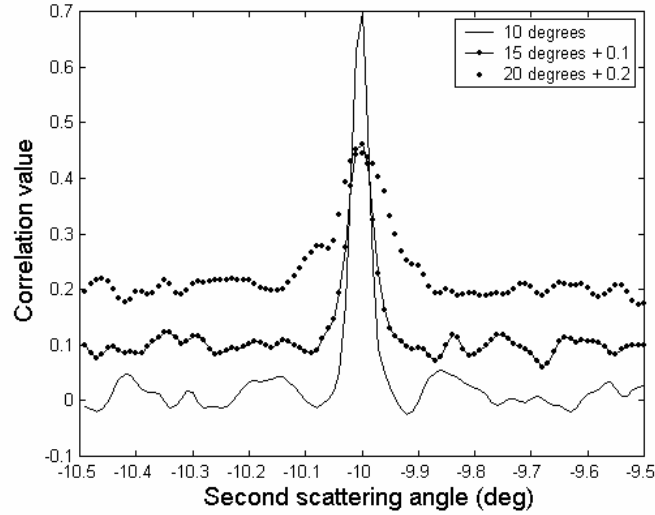


Figure 54: Correlation in the reciprocal scattering configuration as a function of θ_{s2} for fixed θ_{i2} (initially 10°). (Curves at 15 and 20° are superimposed and shifted for clarity).

General $C^{(l)}$ angular condition:

When the incident angle θ_{i2} is closed to θ_{i1} , the speckle pattern can be seen to follow the direction of displacement of the laser. This move is in agreement with Equation (39), and for small difference $\Delta\theta_i$ in incident angle the change in angle of incidence is equal to the change in angle of scattering observation to maximize the correlation function. This results in a memory line [Gu, 1999; Lin, 1997]. When increasing $\Delta\theta_i$, a maximum of correlation can be found following angular condition (39). To test the general validity of condition (2), we set the scattering system in an arbitrary configuration, i.e. $\theta_{i1} = 5^\circ$, $\theta_{s1} = 15^\circ$, $\theta_{i2} = 10^\circ$. Equation (39) provides a peak of correlation for $\theta_{s2} = 20.2^\circ$. Table 7 summarizes the results for the maximal value of the correlation lobe as a function of sample and polarization.

	Sample A	Sample B	Sample C
s-s	0.60	Below 0.1	Below 0.1
p-p	0.65	Below 0.1	0.40

Table 7: Maximal correlation value for $\theta_{s2} = 20.2^\circ$ as a function of sample and polarization.

Some values were below 0.1 and could not be distinguished from background fluctuation contributions. From the results of Table 7, it can be noticed that depending on the sample investigated, condition $C^{(l)}$ may not lead to a distinguishable correlation peak, and for sample C, this value is highly dependent on the polarization configuration. Equation (39) being linked to the memory effect, the absence of a correlation peak when Eq. (39) is satisfied indicates a decrease in the memory effect when increasing $\Delta\theta_i$ [Léger, 1975]. Table 8 represents the maximal value of the correlation peak observed for sample B as a function of θ_{i2} , for $\theta_{i1} = 5^\circ$, $\theta_{s1} = 15^\circ$, and θ_{s2} satisfying Eq. (39). It is noticeable that contrarily to what happens in reciprocal scattering configuration, the decrease in correlation is not due to a change in the average scale of the speckle pattern.

	$\theta_{i2} = 6^\circ$	$\theta_{i2} = 7^\circ$	$\theta_{i2} = 8^\circ$	$\theta_{i2} = 9^\circ$
Correlation	0.9	0.7	0.3	Below 0.1

Table 8: Correlation value for sample B, s-s, when increasing $\Delta\theta_i$, but keeping θ_{i2} satisfying $C^{(l)}$ condition.

Presence of fringes:

The angle-resolved scattering curve for samples B and C displayed diffused fringes, with the positions of maxima of intensity changing with the angle of incidence in agreement with [Lu, 1998]. Figure 55 represents the correlation and intensity curves obtained in the conditions of Table 7 for sample C in p-p polarization.

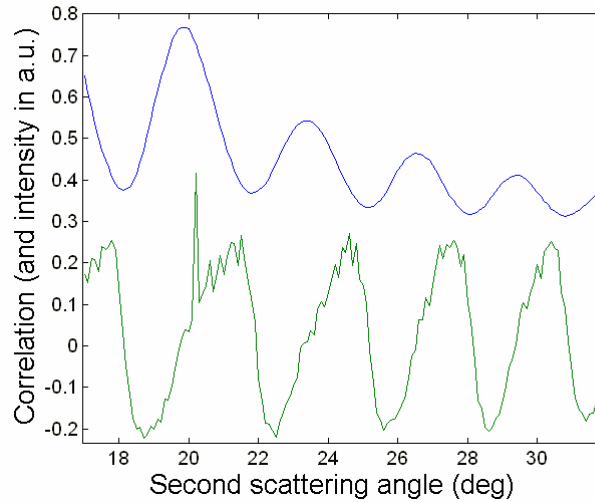


Figure 55: Correlation (down) and intensity (up) for sample C as a function of θ_{s2} , for p-p polarization.

It can be noticed that the angular intensity oscillations result in induced correlation oscillations, although the involved speckle patterns do not show signs of similitude, but present similar global intensity distribution. On the contrary, the correlation peak present for $\theta_{s2} = 20.2^\circ$, does come from similar speckle patterns. This problem may rise interest in the application of other correlation calculators, rather than direct blind point-to-point intensity product between the two images.

Next section thus considers the use of cross-correlation calculation between two speckle images as a potential solution to the issues highlighted in this section.

III.4.3 Alternative way of evaluating speckle correlation (via digital correlation calculation in Fourier plane)

Several issues were highlighted in the previous preliminary study. Among them are the apparent lack of correlation when looking for it in the reciprocal scattering configuration with high angles of incidence and the presence of intensity oscillations which may hide the correlation peak. To solve these problems, attempts were carried out to use an image correlation technique, namely the point-to-point multiplication of two distinct image Fourier transforms. We thus first recall some basic properties of image Fourier transform and multiplication, and then discuss our results obtained via this technique.

Reminder on Fourier transform:

As stated in the first section of this chapter, another way of evaluating speckle correlation between two speckle patterns different than using formula (38) consists in calculating image inter-correlation. The inter-correlation IC_{AB} between two $M \times N$ -sized images $A(m,n)$ and $B(m,n)$ is defined as

$$IC_{AB}(p, q) = \sum_m \sum_n A(m, n) B(m + p, n + q) \quad (40)$$

with p and q ranging from $-M$ to M and from $-N$ to N respectively.

This calculation can be computer resource-consuming, therefore leading to the use of discrete Fourier transform to speed up the process. The interest in using Fourier transform to calculate image correlation relies on one of its properties: after Fourier transform of the images, the correlation can be calculated via a simple multiplication. The discrete Fourier transform (DFT) of image A is expressed as

$$DFT_A(p, q) = \sum_{m=0}^{M-1} \sum_{n=0}^{N-1} A(m, n) e^{-j2\pi(\frac{mp}{M} + \frac{nq}{N})} \quad (41)$$

The correlation C_{AB} between images A and B can then be calculated as

$$C_{AB}(p, q) = DFT^{-1} [DFT(A) \cdot DFT(B)^*] \quad (42)$$

where "." operator means a point-to-point multiplication between the two matrices, "*" stands for the complex conjugate of the designed matrix, and DFT^{-1} represents the discrete inverse Fourier transform.

Here it should be noticed that IC_{AB} and C_{AB} do a priori differ, although they both assess the same property, i.e. image likelihood. Indeed, in the calculation using discrete Fourier transform, the images are supposed to be periodic, and the calculation is therefore equivalent to a circular convolution [Heitz, 2000]. A means to compensate this point is to complete the initial images with surroundings zero values before performing calculations, thus zero-padding the images.

Results with image Fourier transform multiplication:

Calculating the degree of correlation for two identical images using the previous formula leads to a value of unity. Point-to-point multiplying the Fourier transform of the raw speckle images, and keeping the absolute value of the inverse Fourier transform of the product, one obtain the result shown on Figure 56. For all the Figures of this section, x - and y -axis represent pixel position.

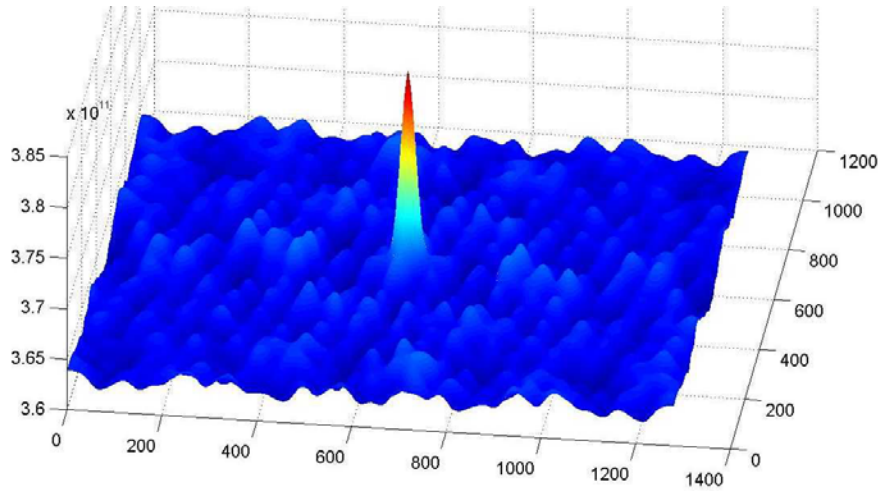


Figure 56: Correlation peak for two identical speckle images.

In order to test the approach on a less trivial case, the speckle images used to obtain the lower curve displayed on Figure 54 are analyzed, corresponding to angles $\theta_{i1} = 10^\circ$, $\theta_{s1} = 0^\circ$, $\theta_{i2} = 0^\circ$, and $\theta_{s2} = -10^\circ$. The procedure results in the correlation image of Figure 57.

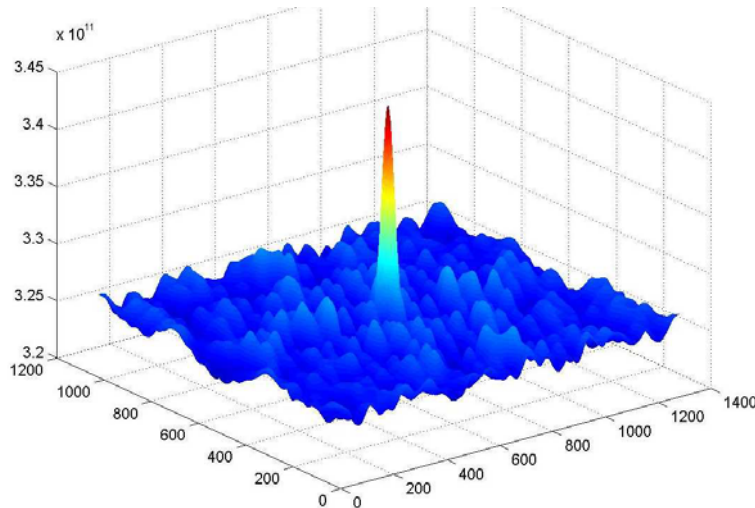


Figure 57: Correlation peak for sample A in reciprocal configuration with $\theta_{i1} = 10^\circ$.

The x and y coordinates correspond to the pixel position on the initial images from the CCD camera. When slightly departing from the angular reciprocal condition, the correlation peak moves towards right or left depending on angular displacement, which is a result of the θ_{s2} displacement-induced speckle shift.

As expected, the technique detects the correlation between two images where it should find it. In the previous section (cf. Figure 54), the correlation peak in the reciprocal configuration was found to decrease when θ_{i1} was increased. This effect was visually attributed to a change in the average speckle pattern size. This observation is confirmed when comparing the correlation image obtained in reciprocal scattering configuration for $\theta_{i1} = 15^\circ$ and $\theta_{i1} = 20^\circ$, as shown on Figure 58.

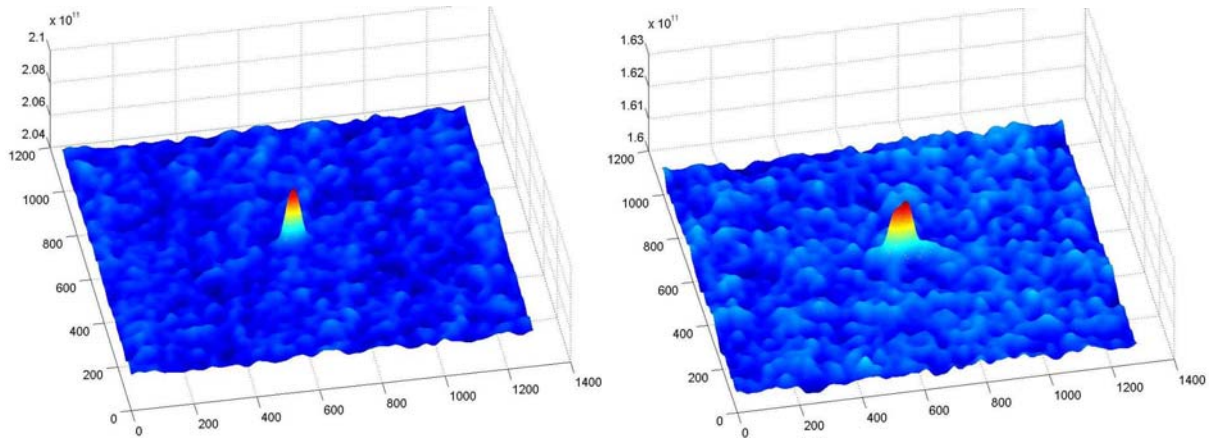


Figure 58: Correlation image for sample A in reciprocal configuration, $\theta_{il} = 15^\circ$ (left) and $\theta_{il} = 20^\circ$ (right).

Indeed, the correlation peak tends to broaden when θ_{il} is increased, as a consequence of the change in the average speckle pattern size. The relative size of the peak with respect to the surrounding background also tends to decrease, because the similarity between the two images decreases. For $\theta_{il} = 30^\circ$, no significant correlation value could be found in the previous section. However, the effects of reciprocity still exist, as evidenced by the presence of an elongated correlation peak on the correlation image displayed on Figure 59.

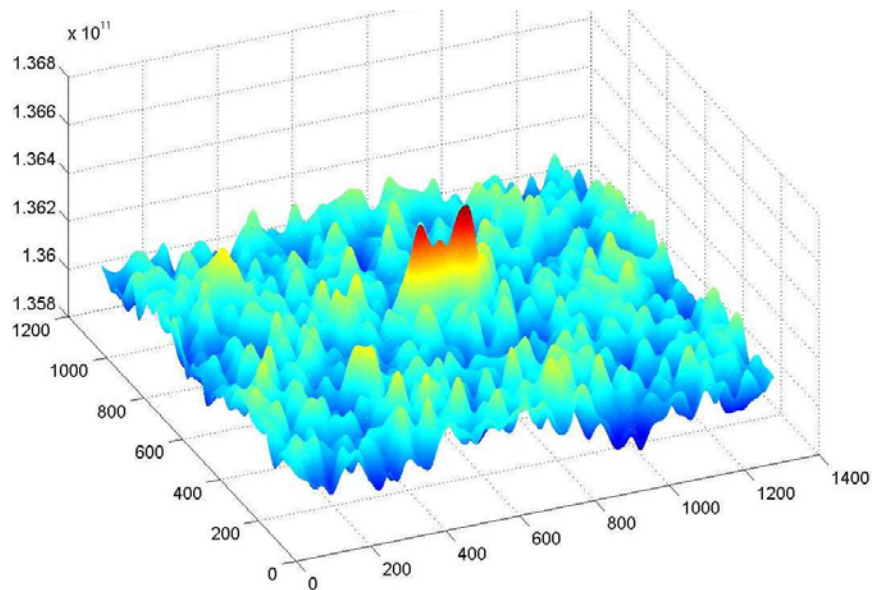


Figure 59: Correlation peak for sample A in reciprocal configuration with $\theta_{il} = 30^\circ$

The second problem evidenced in the previous section was the potential presence of oscillations on the angle-resolved correlation curve, when similar oscillations appear on the angle-resolved intensity curve. This is displayed on Figure 55, and was attributed to global (on the scale of the whole image) intensity distribution similarity between the two images, whatever the two speckle patterns considered may look like. Figure 60 shows the correlation image for sample C, in the same conditions as those for Figure 55, for a scattering angle $\theta_{s2} = 20.2^\circ$.

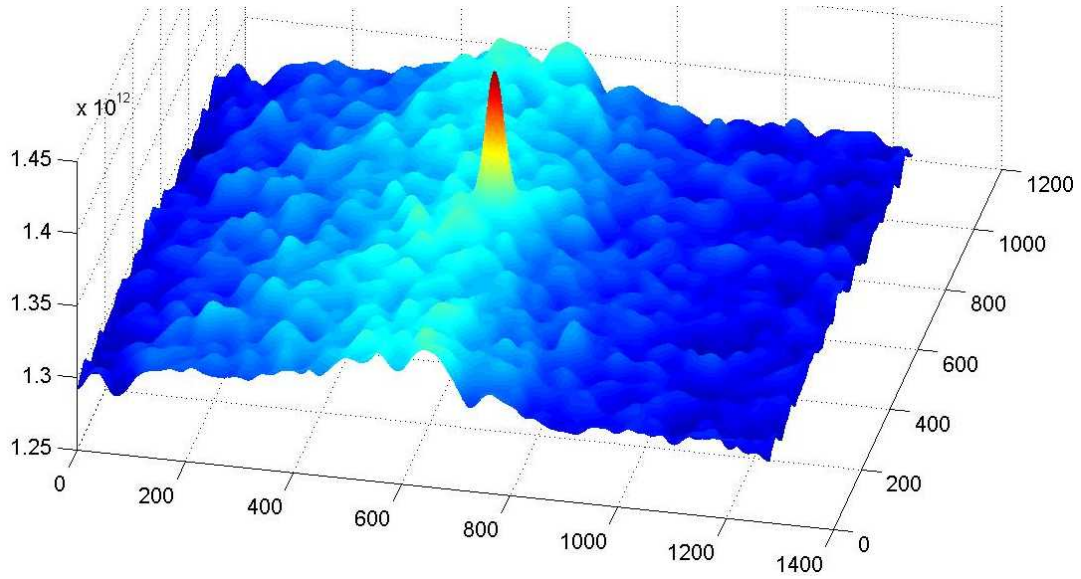


Figure 60: Correlation image for sample C, same condition as for Figure 55, $\theta_{s2} = 20.2^\circ$.

The correlation image presents a vertically central band, as a result of intensity distribution similarity between the two images, but also a central peak, as a consequence of the presence of correlation between the two speckle patterns. In comparison, the correlation image corresponding to a maximum (or minimum) on the angle-resolved intensity curve in the absence of speckle correlation leads to a central band without central peak. Figure 61 illustrates this effect for an intensity maximum, corresponding to $\theta_{s2} = 24.6^\circ$, and an intensity minimum, $\theta_{s2} = 25.6^\circ$.

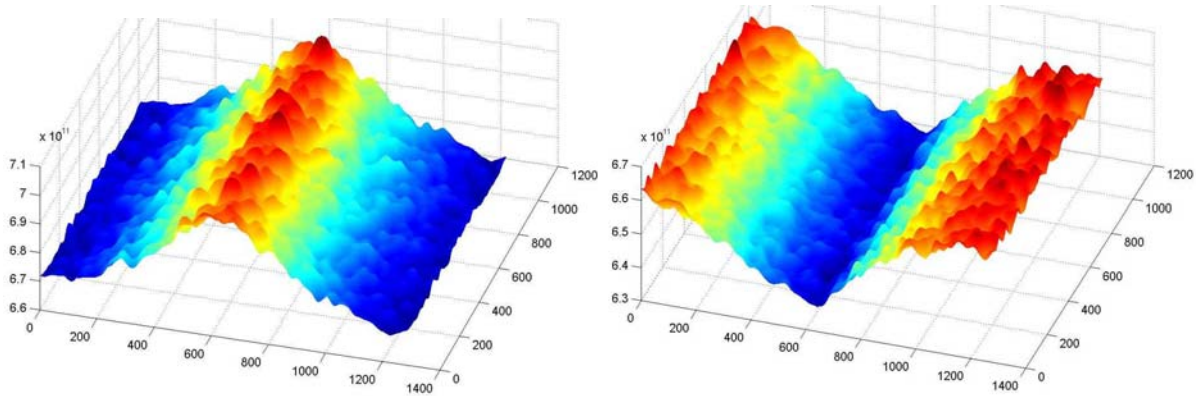


Figure 61: Same as Figure 60, but $\theta_{s2} = 24.6^\circ$ (left) and $\theta_{s2} = 25.6^\circ$ (right).

Considering the results of Table 8 for sample B, when looking for the memory effect with θ_{i2} progressively departing from θ_{i1} , one can observe a decrease in the central correlation peak's height as θ_{i2} increases. For $\theta_{i2} = 9^\circ$, a small peak is still distinguishable from the background, whereas it could not be extracted from noise when calculated in previous section. Figure 62 shows this decrease for the angles $\theta_{i1} = 6^\circ$ and $\theta_{i2} = 9^\circ$.

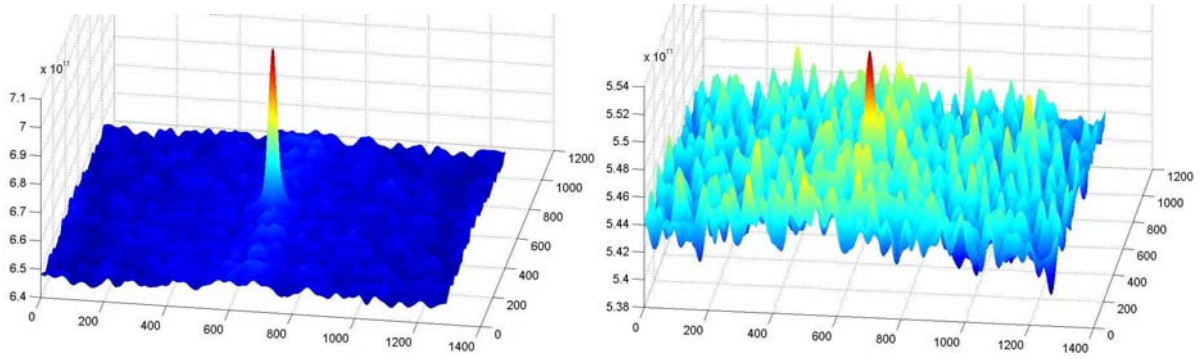


Figure 62: Correlation image, sample B, same conditions as Table 8, with $\theta_{i2} = 6^\circ$ (left) and $\theta_{i2} = 9^\circ$ (right).

The results of this section illustrate the robustness of the image correlation calculation in comparison with the direct point-to-point degree of correlation calculation to detect the presence of correlation between two speckle patterns. However, when the correlation is too weak or does not exist, the procedure does not lead to any noticeable correlation peak. This for instance the case for sample B, in the conditions of Table 8 or Figure 62, when extending the previous process to $\theta_{i2} = 10^\circ$. This is also the case when investigating sample C in the conditions of Table 7 for s-s polarization.

The previous calculations were all performed assuming periodicity conditions for the speckle images. Fourier transform calculations would have required preliminary zero-padding of the images. However, the correlation peak is much more well defined using Fourier transform calculations without zero-padding. Results obtained with preliminary zero-padding (2048x2048) are illustrated on Figure 63 for sample A, s-s polarization, $\theta_{i1} = 10^\circ$, in the reciprocal scattering configuration.

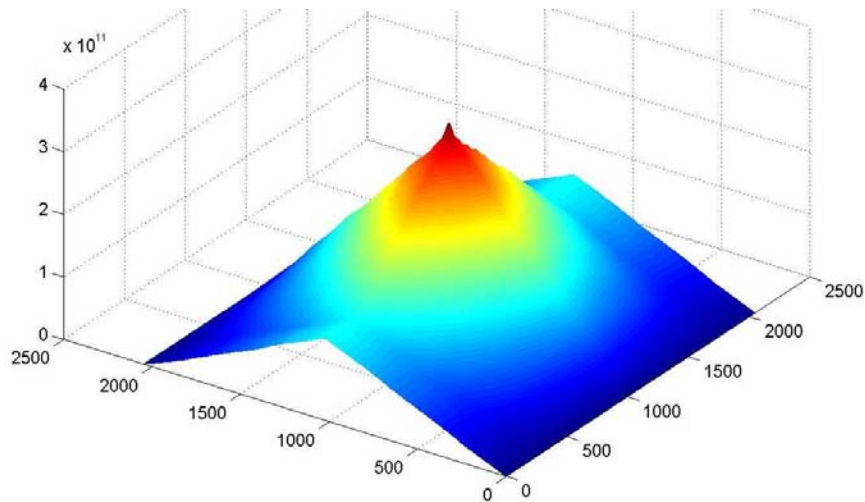


Figure 63: Same as Figure 57, but with preliminary zero-padding.

The work presented in this section has been mainly oriented towards obtaining qualitative correlation peaks, in order to decide whether there exists some correlation or not. However, with proper calibration of the images, one can extend the technique to quantitative correlation measurements, by evaluating the height of the correlation peak [Hinsch, 2000].

III.4.4 $C^{(10)}$ correlation condition

In [McGurn, 1998], a second angle condition for intensity correlation maximum is provided:

$$\sin \theta_{i1} + \sin \theta_{i2} = \sin \theta_{s1} + \sin \theta_{s2} \quad (43)$$

corresponding to correlations denoted $C^{(10)}$, that should be of the same order of magnitude as correlations obeying $C^{(1)}$ angular condition. In [Gu, 1999], this type of correlation was reported taking $\theta_{i1} = \theta_{i2}$, and looking at scattering positions symmetric around the specular direction. A vertical symmetry of the speckle patterns was also noticed for images obtained symmetrically around the specular direction. Due to the presence of the specular beam, and to comply with the geometrical parameters of our set-up, it was not possible to record speckle pattern closer than 4° with respect to specular direction. No symmetry was noticeable in the two patterns obtained symmetrically with respect to the specular direction.

To try to observe intensity correlation according to Eq. (43), we tested the following angular configurations:

- (a) $\theta_{i1} = 10^\circ$, $\theta_{s1} = 0^\circ$, $\theta_{i2} = 0^\circ$, and scanning around $\theta_{s2} = 10^\circ$,
- (b) $\theta_{i1} = 5^\circ$, $\theta_{s1} = 15^\circ$, $\theta_{i2} = 10^\circ$, and scanning around $\theta_{s2} = 0.11^\circ$,
- (c) $\theta_{i1} = 10^\circ$, $\theta_{s1} = 0^\circ$, $\theta_{i2} = -10^\circ$, and scanning around $\theta_{s2} = 0^\circ$.

None of these configurations coupled with any combination of sample and polarization could provide a set of correlation values that could be extracted from background fluctuation contributions.

The Fourier multiplication procedure was applied to images recorded in order to try to observe $C^{(10)}$ correlation. Unfortunately, no evidence of this correlation was found for these samples using this procedure either.

The influence of roughness amplitude in the potential observation of speckle correlation obeying $C^{(10)}$ angular condition is not presently completely characterized. In their numerical simulation [McGurn, 1999], McGurn and Maradudin set the roughness amplitude to a value of 15nm. However, they made no comment on the evolution of this correlation as a function of roughness amplitude. Two theoretical approaches attempted to assess the problem. Kawanishi et al. [Kawanishi, 1999] showed that contrarily to $C^{(1)}$ correlation, $C^{(10)}$ should only be observable in the single scattering regime. This yet does not resolve the paradox for the case of silica-on-silicon, keeping in mind that for this roughness amplitude the scattering phenomenon is that of single scattering with single or multiple reflection [Lu, 1998; Kaganovskii, 1999; Blumberg, 2004]. Nieto-Vesperinas et al. [Nieto-Vesperinas, 1997] reaches the conclusion that this phenomenon was independent of scattering regime, but that it would disappear as roughness amplitude increases, namely $\sigma > 14\text{nm}$.

With regard to these considerations, it is possible that the roughness amplitude of the samples studied in this work is too high to enable the observation of significant speckle correlation according to $C^{(10)}$ condition. For the observations reported in [Gu, 1999], the roughness amplitude was measured to be of 11nm, thus in a similar range as used in [McGurn, 1999; Nieto-Vesperinas, 1997]. The question remains however open, considering experimental results reported by West and O'Donnell [West, 1999], where two metal surfaces with σ of the order of 10 nm were found to give rise to observable $C^{(10)}$ correlation or not depending on their surface spectrum.

III.5 Conclusions on speckle and light scattering studies

In this chapter, angle-resolved light scattering measurements were reported on a set-up specially built for this work. Using silica-on-silicon wafers provided by Alcatel SEL, angle-resolved intensity have been observed in light scattered by the surface which corresponds to diffused fringes described in literature [Lu, 1998]. Several properties of these fringes were obtained, like their symmetry with respect to sample's surface normal or their move as a function of incident angle. Upgrading the set-up with a CCD camera, angular speckle correlation was investigated for the same samples. We show the interest of two-dimensional cross-correlation image calculation to avoid the ambiguity in correlation evaluation that could introduce the presence of diffused fringes. Three main experimental results were also found: speckle correlation is always observed in the reciprocal scattering configuration, whatever the sample or polarization; speckle correlation corresponding to $C^{(1)}$ angular condition depends on the sample illuminated; speckle correlation corresponding to $C^{(10)}$ could not be observed for any sample nor polarization.

Regarding the results presented so far, one may reasonably ask on the potential of angle-resolved light scattering and speckle correlation aiming at roughness evaluation in silica-on-silicon technology. The first indication that can be extracted is the range of roughness magnitude. Indeed, due to the angular behavior of the fringes as a function of the angle of incidence, this sets the roughness to be of the order of several tens of nanometers, or lower if thickness fluctuations are present. The question of the presence of thickness fluctuations could be potentially solved by adopting for instance the retroreflection configuration suggested in [Blumberg, 2002].

Further work is required for a quantitative evaluation of roughness amplitude. Among the possible promising continuations is the investigation of fringe contrast. Blumberg et al. [Blumberg, 2004] assimilated this contrast to be a linear function of σ^2 for σ below 100nm, and this could be a very convenient way for assessing silica-on-silicon wafer surface roughness. Another interesting feature is the dependence of $C^{(1)}$ speckle correlation on sample assessed. A study with characterized samples composed of a transparent layer on a reflecting substrate could help investigate further this effect. Finally, the conditions of appearance of $C^{(10)}$ remains subject to discussion, and this correlation could provide a tool of investigation for small amplitude roughness.

General conclusion

This work was dedicated to the study of roughness in silica-on-silicon technology for optical applications. Two different aspects were evoked: first, its intrinsic characteristics, through the evaluation of waveguide sidewall roughness; secondly, its influence on light scattering, with angle-resolved measurements of scattered light intensity and angular speckle correlation calculation.

Chapter 1 described the statistical characterization of a surface topography, together with the different instruments or techniques available to evaluate it. These techniques were sorted out according to their working principles, probe-, electron-, or optics-based. This review illustrated the need to clarify the objectives and constraints before carrying out roughness measurement, each instrument presenting its advantages and drawbacks with respect to the problem to be addressed. The optical waveguide fabrication process was then given to define the challenge constituted by this work.

Chapter 2 tackled the measurement issue contained in the evaluation of waveguide sidewall surface quality. The procedure known as line-edge roughness was first applied to the samples of this study. The values obtained in that way served as comparison and calibration respectively for the stereoscopic and shape-from-shading approaches. The stereoscopic approach for sidewall roughness measurement developed in this work was then reported. Modeling moves within the scanning electron microscope using rotation matrices, an elegant solution was obtained to record stereoscopic image pair and thereafter extract surface topography. The procedure was then practically implemented, and the influence of recording and reconstructing parameters investigated. Results were compared with LER values and discussed. To overcome the limitations of the stereoscopic technique, an approach based on the use of a shape-from-shading algorithm was developed, which consists in the surface topography reconstruction, and then calibration of the reconstructed profile. In our case, we proposed a calibration based on LER values. The technique showed promising results, both in terms of reconstruction quality and ability to assess and distinguish low amplitude roughness. Due to its fast calculation aspect, its repeatability subject to image conditions was checked in order to enable its implementation for in-line inspection.

Chapter 3 dealt with laser light scattering from silica-on-silicon wafers. The principles of speckle formation and correlation were first recalled, together with predictions on their localization and on angular light scattered distribution. The realization of the set-up aiming at carrying out measurements for this thesis was then detailed, and the characteristics of the samples addressed in this work were given, concerning the thickness of silica layers, their roughness and thickness fluctuation amplitude. Angle-resolved measurements of laser light scattered by these samples were then reported. They demonstrated the presence of diffused fringes centered around sample's normal and moving with the angle of incidence, in conformity with theoretical calculations and numerical simulations available in literature. Furthermore, the possibility to retrieve silica layer's thickness from an analysis of intensity extrema's angular position was evidenced. Two approaches to assess these thickness fluctuations were then proposed based respectively on the use of a grazing angle of incidence and light retroreflection. Angular speckle correlations showed a stable value in the reciprocal configuration, thus excluding this configuration as surface probe, varying $C^{(1)}$ values depending on sample and polarization, the absence of significant $C^{(10)}$ value. Due to the

presence of diffused fringes, it was demonstrated how the calculation of speckle pattern cross-correlation may provide additional clue to determine the presence of correlation.

The results presented in this thesis were all obtained for silica-on-silicon technology. However, it is important to note the general nature they contain. Concerning the SEM-based approaches for sidewall roughness measurement, the principles of both stereoscopy and shape-from-shading remain unaltered when replacing silica by another material. The electron yield within the SEM may change (thus requiring adequate calibration), but the irradiance equation is still valid. This also preserves the basis for stereoscopic inspection. Concerning light scattering and speckle correlation studies, the results may be extended to any system of transparent layer over a reflecting substrate, assuming the magnitude relationship between optical wavelength, layer thickness and roughness amplitude is preserved.

Bibliography

- [AHAMMAD, 2002] P. Ahammad, A. Mukherjee. *Modified shape-from-shading approach to SEM based photoresist CD metrology*. Proc. SPIE 4889, 365-373, 2002.
- [AZZAM, 1987] R. M. A. Azzam, N. M. Bashara. *Ellipsometry and polarized light*. North-Holland, Amsterdam, 1987.
- [AZIZ, 2000] D. Aziz. *High-resolution optical tools for shrinking pole tips*. Application Note, Veeco Metrology Group, 2000.
- [BAZYLENKO, 1996a] M. V. Bazylenko, M. Gross, M. Faith. *Effect of reactive ion etching-generated sidewall roughness on propagation loss of buried-channel silica waveguides*. Appl. Phys. Lett. 69, 2178-2180, 1996.
- [BAZYLENKO, 1996b] M. V. Bazylenko and M. Gross. *Reactive ion etching of silica structures for integrated optics applications*. J. Vac. Sci. Technol. A 14, 2994-3003, 1996.
- [BEIL, 1990] W. Beil and I. C. Carlsen. *A combination of topographical contrast and stereoscopy for the reconstruction of surface topographies in SEM*. J. Microscopy 157, 127-133, 1990.
- [BEIL, 1991] W. Beil and I. C. Carlsen. *Surface reconstruction from stereoscopy and "shape from shading" in SEM images*. Machine Vision and Applications 4, 271-285, 1991.
- [BENATMANE, 2002] A. Benatmane. *Développement de la microscopie interférométrique pour une meilleure analyse morphologique des couches minces et épaisses des matériaux semiconducteurs et optiques*. Ph.D. dissertation, Louis Pasteur University, 2002.
- [BINNIG, 1982] G. Binnig, H. Rohrer, Ch. Gerber, E. Weibel. *Surface studies by scanning tunneling microscopy*. Phys. Rev. Lett. 49 (1), 57-60, 1982.
- [BINNIG, 1986] G. Binnig, C. F. Quate, Ch. Gerber. *Atomic Force Microscope*. Phys. Rev. Lett. 56 (9), 930-933, 1986.
- [BLUMBERG, 2002] D. G. Blumberg, V. Freilikher, I. Fuks, Y. Kaganovskii, A. A. Maradudin and M. Rosenbluh. *Effects of roughness on the retroreflection from dielectric layers*. Waves in Random Media 12, 279-292, 2002.
- [BLUMBERG, 2004] D. Blumberg, V. Freilikher, Y. Kaganovskii, A. Kotlyar, A. Maradudin. *Backscattering of light from a dielectric layer on a reflecting substrate*. Opt. Lett. 29 (12), 1372-1374, 2004.
- [BONY, 2003] A. Bony, Y. Takakura, K. Satzke, P. Meyrueis. *Angular correlation properties of 2D-nano-roughness-induced speckle patterns for silica-on-silicon wafers*. Physica Status Solidi c, Vol. 0 (8), pp. 3027-3031, 2003.

[BONY, 2004] A. Bony, A. Heid, Y. Takakura, K. Satzke, P. Meyrueis. *Waveguide sidewall roughness estimation via shape-from-shading reconstruction of SEM pictures*. Proc. SPIE 5355, 103-110, 2004.

[BORN & WOLF, 2002] M. Born, E. Wolf. *Principles of Optics*. 7th expanded edition, Cambridge University Press, 2002.

[BULLA, 2004] D. A. P. Bulla, W.-T. Li, C. Charles, R. Boswell, A. Ankiewicz, J. Love. *Deposition and characterization of silica-based films by helicon-activated reactive evaporation applied to optical waveguide fabrication*. Appl. Opt. 43 (14), 2978-2985, 2004.

[BRIERS, 1993] J. D. Briers. *Surface roughness evaluation*. In [SIROHI, 1993], Chapter 8, pp. 375-426.

[BRIERS, 1999] J. D. Briers. *Interferometric optical testing: an inter-laboratory comparison*. J. Opt. A: Pure Appl. Opt 1, 1-14, 1999.

[BUNRIT, 2000] S. Bunrit, N. Covavisaruch, B. Thipakorn. *Determining surface shape of SEM images using non-linear shape from shading technique*, Proceedings Image and Vision Computing New-Zealand 2000, pp. 316-321, Hamilton, 2000.

[CASTLEMAN, 1996] K. R. Castleman. *Digital Image Processing*. Prentice-Hall, 1996.

[CHI] T. Chi, T. Ballinger, R. Olds. *Measuring microelectromechanical systems (MEMS) using stylus surface profilers*. Application note, Veeco Metrology Group.

[COLLIEX, 1998] C. Colliex. *La microscopie électronique*. "Que Sais-je" 1045, Presses Universitaires de France, 1998.

[CONSTANTOUDIS, 2003] V. Constantoudis, G. P. Patsis, A. Tserepi, E. Gogolides. *Quantification of line-edge roughness of photoresists. II. Scaling and fractal analysis and the best roughness descriptors*. J. Vac. Sci. Technol. B 21 (3), 1019-1026, 2003.

[COURSEY, 2001] M. Coursey. *A better roughness gauge ?*. Photonics Spectra, pp. 125-130, July 2001.

[DADAP, 1994] J. I. Dadap, B. Doris, Q. Deng, M. C. Downer, J. K. Lowell, A. C. Diebold. *Randomly oriented Angstrom-scale microroughness at the Si(100)/SiO₂ interface probed by optical second harmonic generation*. Appl. Phys. Lett. 64 (16), 2139-2141, 1994.

[DAINTY, 1984] J. C. Dainty. *Laser speckle and related phenomena*. Springer-Verlag, Berlin, Second Enlarged Edition, 1984.

[DOMINGO, 2003] C. Domingo. *Espectroscopía infrarroja sobre superficies de nanopartículas metálicas*. Proceeding Summer School "Nanoestructuras: Fabricación, Caracterización y Aplicaciones", Jaca, Spain, pp. 73-94, 2003.

[DUPARRE, 2002] A. Duparré, J. Ferre-Borrull, S. Gliech, G. Notni, J. Steinert, J. M. Bennett. *Surface characterization techniques for determining the root-mean-square*

roughness and power spectral densities of optical components. Appl. Opt. 41 (1), 154-171, 2002.

[ELLISON, 1991] T. P. Ellison and C. J. Taylor. *Calculating the surface topography of integrated circuit wafers from SEM images*. Image and Vision Computing 9, 3-9, 1991.

[ELSON, 2001] J. M. Elson. *Propagation in planar waveguides and the effects of wall roughness*. Opt. Express 9, 461-475, 2001.

[FOREST, 2004] C. R. Forest, C. R. Canizares, D. R. Neal, M. McGuirk, M. L. Schattenburg. *Metrology of thin transparent optics using Shack-Hartmann wavefront sensing*. Opt. Eng. 43 (3), 742-753, 2004.

[FRICKE-BEGEMANN, 2004] T. Fricke-Begemann, K. D. Hinsch. *Measurement of random processes at rough surfaces with digital speckle correlation*. J. Opt. Soc. Am. A 21 (2), 252-262, 2004.

[FRIIS, 2001] P. Friis, K. Hoppe, O. Leistiko, K. B. Mogensen, J. Hübner, J. P. Kutter. *Monolithic integration of microfluidic channels and optical waveguides in silica on silicon*. Appl. Opt. 40 (34), 6246-6251, 2001.

[GERMER, 2000] T. A. Germer. *Measurement of roughness of two interfaces of a dielectric film by scattering ellipsometry*. Phys. Rev. Lett. 85 (2), 349-352, 2000.

[GOH, 1997] T. Goh, S. Suzuki, A. Sugita. *Estimation of waveguide phase error in silica-based waveguides*. J. Lightwave Technol. 15, 2107-2113, 1997.

[GOODMAN, 1984] J. W. Goodman. *Statistical properties of laser speckle patterns*. In [Dainty, 1984], pp. 9-75, 1984.

[GORECKI, 1994] C. Gorecki. *Phase-correlation techniques for quasi real-time measurement of deformations with digital speckle interferometry*. Appl. Opt. 33 (14), 2933-2938, 1994.

[GORECKI, 2000] C. Gorecki. *Optimization of plasma-deposited silicon oxinitride films for optical channel waveguides*. Opt. Lasers Eng. 33, 15-20, 2000.

[GU, 1996] Z.-H. Gu, M. Josse, M. Ciftan. *Observation of giant enhanced backscattering of light from weakly rough dielectric films on reflecting metal substrates*. Opt. Eng. 35 (2), 370-375, 1996.

[GU, 1999] Z.-H. Gu, A. R. McGurn. *Dynamic behavior of speckles from rough surface scattering*. Proc. SPIE 3784, 285-295, 1999.

[GU, 2002a] Z.-H. Gu. *High order correlation from rough surface scattering*. Proc. SPIE 4780, 15-23, 2002.

[GU, 2002b] Z.-H. Gu, I. M. Fuks, M. Ciftan. *Enhanced backscattering at grazing angles*. Opt. Lett. 27 (23), 2067-2069, 2002.

- [GU, 2004a] Z.-H. Gu, I. M. Fuks, M. Ciftan. *Grazing angle enhanced backscattering from a dielectric film on a reflecting metal substrate*. Opt. Eng. 43 (3), 559-567, 2004.
- [GU, 2004b] Z.-H. Gu. *High-order correlations from rough-surface scattering*. Appl. Opt. 43 (15), 3061-3065, 2004.
- [HAMED, 2004] A. M. Hamed, H. El-Ghandoor, F. El-Diasty, M. Saady. *Analysis of speckle images to assess surface roughness*. Opt. Laser Techno. 36 (3), 249-253, 2004.
- [HEID, 2003] A. Heid. *Influence of sidewall roughness on waveguide attenuation*. Internal technical report, Alcatel SEL AG, 2003.
- [HEITZ, 2000] F. Heitz. *Traitement du signal bidimensionnel. (Notes de cours)*. 2000.
- [HINSCH, 2000] K. D. Hinsch, T. Fricke-Begemann, G. Gülker, K. Wolff. *Speckle correlation for the analysis of random processes at rough surfaces*. Opt. Lasers Eng. 33, 87-105, 2000.
- [HORN, 1986] B. K. P. Horn. *Robot Vision*. The MIT Press, 1986.
- [HORN, 1990] B. K. P. Horn. *Height and gradient from shading*. International Journal of Computer Vision 5 (1), 37-75, 1990.
- [HU, 2003] Y. Hu, C. Wermer, D. Li. *Influence of three-dimensional roughness on pressure-driven flow through microchannels*. Journal of Fluids Engineering 125, 871-879, 2003
- [HUN, 2002] C. Hun. *Exploitation de la texture d'images de speckle pour caractériser, de façon globale, l'état de surface des chaussées à l'échelle de la microtexture*. Ph.D. dissertation, Louis Pasteur University, 2002.
- [ISHIKAWA, 1999] K. Ishikawa, H. Ogawa, S. Fujimura. *Contribution of interface roughness to the infrared spectra of thermally grown silicon dioxide films*. J. Appl. Phys. 85 (8), 4076-4082, 1999.
- [JAIN, 1989] A. K. Jain. *Fundamentals of digital image processing*. Prentice-Hall 1989.
- [JANG, 2003] J. H. Jang, W. Zhao, J. W. Bae, D. Selvanathan, S. L. Rommel, I. Adesida, A. Lepore, M. Kwakernaak, J. H. Abeles. *Direct measurement of nanoscale sidewall roughness of optical waveguides using an atomic force microscope*. Appl. Phys. Lett. 83 (20), 4116-4118, 2003.
- [JONES, 1994] A. G. Jones and C. J. Taylor. *Automated interpretation of SEM images*. IEEE Region 10's Ninth Annual International Conference: Frontiers of Computer Technology, Proceedings, Vol. 2, pp. 872-876, 1994.
- [JOY, 1997] D. C. Joy. *Scanning Electron Microscopy*. In "Electron Microscopy. Principles and fundamentals", edited by S. Amelinckx, D. van Dyck, J. van Landuyt, G. van Tendeloo. VCH, Weinheim, pp. 305-327, 1997.

- [JUAN, 1996] W. H. Juan and S. W. Pang. *Controlling sidewall smoothness for micromachined Si mirrors and lenses*. J. Vac. Sci. Technol. B 14 (6), 4080-4084, 1996.
- [KACZMAREK, 1998] D. Kaczmarek. *Backscattered electrons topographic mode problems in the scanning electron microscope*. Scanning Microscopy 12 (1), 161-169, 1998.
- [KAGANOVSKII, 1998] Y. S. Kaganovskii, V. D. Freilikher, E. Kanzieper, Y. Nafcha, M. Rosenbluh. *Interference in light scattering from slightly rough dielectric layers*. Opt. Lett. 23 (5), 316-318, 1998.
- [KAGANOVSKII, 1999] Y. S. Kaganovskii, V. D. Freilikher, E. Kanzieper, Y. Nafcha, M. Rosenbluh, I. M. Fuks. *Light scattering from slightly rough dielectric films*. J. Opt. Soc. Am. A 16 (2), 331-338, 1999.
- [KANO, 1996] H. Kano, S. Kawata. *Two-photon-excited fluorescence enhanced by a surface plasmon*. Opt. Lett. 21 (22), 1848-1850, 1996.
- [KAWANISHI, 1999] T. Kawanishi, Z. L. Wang, M. Izutsu, H. Ogura. *Conjugate memory effect of random scattered waves*. J. Opt. Soc. Am. A 16 (6), 1342-1349, 1999.
- [KAWASHI, 1990] M. Kawashi. *Silica waveguides on silicon and their application to integrated-optic components*. Optical and Quantum Electronics 22, 391-416, 1990.
- [KNOTTS, 1992] M. E. Knotts, T. R. Michel, K. A. O'Donnell. *Angular correlations functions of polarized intensities scattered from a one-dimensionally rough surface*. J. Opt. Soc. Am. A 9 (10), 1822-1831, 1992.
- [LACEY, 1990] J. P. R. Lacey and F. P. Payne. *Radiation loss from planar waveguides with random wall imperfections*. IEE Proc. 137, pp. 282-288, 1990.
- [LADOUCEUR, 1992] F. Ladouceur, J. D. Love, and T.J. Senden. *Measurement of surface roughness in buried channel waveguides*. Electron. Lett. 38 (28), 1321-1322, 1992.
- [LADOUCEUR, 1994] F. Ladouceur, J. D. Love, T. J. Senden. *Effect of side wall roughness in buried channel waveguides*. IEE Proc.-Optoelectronics, Vol. 141, pp. 242-248, 1994.
- [LADOUCEUR, 1996] F. Ladouceur and J. D. Love. *Silica-based buried channel waveguides and devices*. Chapter 2. Chapman & Hall, 1996.
- [LADOUCEUR, 1997] F. Ladouceur. *Roughness, inhomogeneity, and integrated optics*. J. Lightwave Technol. 15, 1020-1025, 1997.
- [LÉGER, 1975] D. Léger, E. Mathieu, J. C. Perrin. *Optical surface roughness determination using speckle correlation technique*. Appl. Opt. 14 (4), 872-877, 1975.
- [LÉGER, 1976] D. Léger, J. C. Perrin. *Real-time measurement of surface roughness by correlation of speckle patterns*. J. Opt. Soc. Am. 66 (11), 1210-1217, 1976.

- [LEHMANN, 1999] P. Lehmann. *Surface-roughness measurement based on the intensity correlation function of scattered light under speckle-pattern illumination*. Appl. Opt. 38 (7), 1144-1152, 1999.
- [LEONARD, 1998] L. C. Leonard, V. Toal. *Roughness measurement of metallic surfaces based on the laser speckle contrast method*. Opt. Lasers Eng. 30, 433-440, 1998.
- [LEOPOLD, 1997] J. Leopold, M. Hertwig, H. Günther, B. Staeger. *Three-dimensional measurement of macro- and microdomains using optical methods*. Opt. Lasers Eng. 28, 1-16, 1997.
- [LIN, 1997] Z. Q. Lin, Z.-H. Gu. *Experimental study of the angular correlation function in the double passage of waves through a one-dimensional random phase screen*. Waves in Random Media 7, 435-456, 1997.
- [LU, 1997] J. Q. Lu, Z.-H. Gu. *Angular correlation function of speckle patterns scattered from a one-dimensional rough dielectric film on a glass substrate*. Appl. Opt. 36 (19), 4562-4570, 1997.
- [LU, 1998] J. Q. Lu, J. A. Sánchez-Gil, E. R. Méndez, Z.-H. Gu, A. A. Maradudin. *Scattering of light from a rough dielectric film on a reflecting substrate: diffuse fringes*. J. Opt. Soc. Am. A 15 (1), 185-195, 1998.
- [MARTIN, 1994] Y. Martin and K. Wickramasinghe. *Method for imaging sidewalls by atomic force microscopy*. Appl. Phys. Lett. 64, 2498-2500, 1994.
- [MARX, 1990] E. Marx, T. V. Vorburger. *Direct and inverse problems for light scattered by rough surfaces*. Appl. Opt. 29 (25), 3613-3626, 1990.
- [MATSUTANI, 1995] A. Matsutani, F. Koyama, K. Iga. *Three-dimensional electron probe roughness analysis of InP sidewalls processed by reactive ion beam etching*. Appl. Phys. Lett. 66 (1), 64-66, 1995.
- [McGURN, 1998] A. R. McGurn, A. A. Maradudin. *Speckle correlations in the light scattered by a dielectric film with a rough surface : Guided waves effects*. Phys. Rev. B 58 (8), 5022-5031, 1998.
- [McLAUGHLIN, 1998] A. J. McLaughlin, J. R. Bonar, M. G. Jubber, P. V. S. Marques, S. E. Hicks, C. D. W. Wilkinson, J. S. Aitchison. *Deep, vertical etching of flame hydrolysis deposited hi-silica glass films for optoelectronic and bioelectronic applications*. J. Vac. Sci. Technol. B 16 (4), 1860-1863, 1998.
- [NELSON, 1999] C. Nelson, S. C. Palmateer, A. R. Forte, and T. M. Lyszczarz. *Comparison of metrology methods for quantifying the line edge roughness of patterned features*. J. Vac. Sci. Technol. B 17, 2488-2498, 1999.
- [NEWTON, 1952] Sir Isaac Newton. *Opticks*. Dover, New York, 1952.

[NIETO-VESPERINAS, 1990] M. Nieto-Vesperinas, J. A. Sánchez-Gil, A. J. Sant, J. C. Dainty. *Light transmission from a randomly rough dielectric diffuser: theoretical and experimental results*. Opt. Lett. 15 (22), 1261-1263, 1990.

[NIETO-VESPERINAS, 1997] M. Nieto-Vesperinas, A. A. Maradudin, A. V. Shchegrov, A. R. McGurn. *Speckle patterns produced by weakly rough random surfaces: existence of a memory effect twin peak in the angular correlations and its consequences*. Opt. Commun. 142, 1-6, 1997.

[NYSSONEN, 1991] D. Nyssonen, L. Landstein, E. Coombs. *Two-dimensional atomic probe microprobe trench metrology system*. J. Vac. Sci. Technol. B 9 (6), 3612-3616, 1991.

[O'DONNELL, 1987] K. A. O'Donnell, E. R. Mendez. *Experimental study of scattering from characterized random surfaces*. J. Opt. Soc. Am. 4 (7), 1194-1205, 1987.

[O'DONNELL, 1993] K. A. O'Donnell. *Effects of finite stylus width in surface contact profilometry*. Appl. Opt. 32 (25), 4922-4928, 1993.

[OGILVY, 1991] J. A. Ogilvy. *Theory of wave scattering from random rough surfaces*. Institute Of Physics Publishing, 1991.

[PÉREZ, 2000] J.-P. Pérez. *Optique, Fondements et applications*. Dunod, 2000.

[PERROT, 1995] O. Perrot, L. Guinvarc'h, D. Benhaddou, P. C. Montgomery, R. Rimet, B. Boulard, C. Jacoboni. *Optical investigation of fluoride glass planar waveguides made by vapour phase deposition*. J. Non-Cryst. Solids 184, 257-262, 1995.

[PIAZZESI, 1973] G. Piazzesi. *Photogrammetry with the scanning electron microscope*. J. Phys. E 4, 392-396, 1973.

[PLATT, 2001] B. C. Platt, R. Shack. *History and principles of Shack-Hartmann wavefront sensing*. J. Refract. Surg. 17, 573-577, 2001.

[RODRÍGUEZ, 1999] J. Rodríguez, R. D. Crespo, S Fernández, J. Pandavenes, J. Olivares, S. Carrasco, I. Ibáñez, J. M. Virgós. *Radiation losses on discontinuities in integrated optical devices*. Opt. Eng. 38 (11), 1896-1906, 1999.

[REYNOLDS, 1999] G. W. Reynolds and J. W. Taylor. *Correlation of atomic force microscopy sidewall roughness measurements with scanning electron microscopy line-edge roughness measurements on chemically amplified resists exposed by x-ray lithography*. J. Vac. Sci. Technol. B 17 (6), 2723-2729, 1999.

[RUANO, 2000] J. M. Ruano, V. Benoit, J. S. Aitchison, J. M. Cooper. *Flame hydrolysis deposition of glass on silicon for the integration of optical and microfluidic devices*. Anal. Chem. 72 (5), 1093-1097, 2000.

[RUANO, 2003] J. M. Ruano, A. Glidle, A. Cleary, A. Walmsley, J. S. Aitchison, J. M. Cooper. *Design and fabrication of a silica on silicon integrated optical biochip as a fluorescence microarray platform*. Biosensors and Bioelectronics 18, 175-184, 2003.

- [RUIZ-CORTÉS, 2002] V. A. Ruiz-Cortés, J. C. Dainty. *Experimental light scattering measurements from large-scale composite randomly-rough surface*. J. Opt. Soc. Am. A 19 (10), 2043-2052, 2002.
- [SANCHEZ-GIL, 1997] J. A. Sánchez-Gil. *Degenerate optical memory effect in dielectric films with randomly rough surfaces*. Phys. Rev. B 55 (23), 15928-15936, 1997.
- [SANCHEZ-GIL, 2002] J. A. Sánchez-Gil, J. V. García-Ramos, E. R. Méndez. *Electromagnetic mechanism in surface-enhanced Raman scattering from Gaussian-correlated randomly rough metal substrates*. Opt. Express 10 (17), 879-886, 2002.
- [SATO, 1991] A. Sato, Y. Tsukamoto, M. Baba, and S. Matsui. *Measurement of sidewall roughness by scanning tunneling microscope*. Jpn. J. Appl. Phys. 30, 3298-3301, 1991.
- [SAXON, 1955] D. S. Saxon. *Tensor scattering matrix for the electromagnetic field*. Phys. Rev. 100 (6), 1771-1775, 1955.
- [SIROHI, 1993] R. Sirohi. *Speckle Metrology*. Marcel Dekker Inc, 1993.
- [SMIT, 1988] M. K. Smit. *New focusing and dispersive planar component based on an optical phased array*. Electron. Lett. 24 (7), 385-386, 1988.
- [SOLECKY, 1999] E. Solecky and C. Archie. *Image Processing for SEMs: Is this the way to go for CD metrology?*. Proc. SPIE 3677, 796-806, 1999.
- [STAMPFL, 1996] J. Stampfl, S. Scherer, M. Gruber, O. Kolednik. *Reconstruction of surface topographies by scanning electron microscopy for application in fracture research*. Appl. Phys. A 63, 341-346, 1996.
- [TAKAKURA, 1996] Y. Takakura, M. T. Sehili, P. Meyrueis. *Method to improve the accuracy of super-smooth surface scatter data*. Proc. SPIE 2862, 34-42, 1996.
- [TSAI, 1994] P.-S. Tsai and M. Shah. *Shape from shading using linear approximation*. Image and Vision Computing 12, 487-498, 1994.
- [TURNER, 2003] P. S. Turner, C. E. Nockolds, S. Bulcock. *Electron Microscope Techniques for Surface Characterization*. In "Surface Analysis Methods in Materials Science", edited by D. J. O'Connor, B. A. Sexton, R. St. C. Smart. Springer. Pp. 85-105, 2003.
- [VEECO, 2003] *Replacing Cross-Section SEMs with the dimension X3D AFM for sensitive 193nm photoresist metrology*. Application Note, Veeco Metrology Group, 2003.
- [VORBURGER, 1993] T. V. Vorburger, E. Marx, T. R. Lettieri. *Regimes of surface roughness measurable with light scattering*. Appl. Opt. 32 (19), 3401-3408, 1993.
- [VORBURGER, 2002] T. V. Vorburger, J. Fu, N. Orji. *In the rough*. SPIE's OEmagazine, pp. 31-34, March 2002.
- [WEBB, 1996] R. H. Webb. *Confocal optical microscopy*. Rep. Prog. Phys. 59, 427-471, 1996.

[WEST, 1999] C. S. West, K. A. O'Donnell. *Angular correlation functions of light scattered from weakly rough metal surfaces*. Phys. Rev. B 59 (3), 2393-2406, 1999.

[ZHANG, 1999] R. Zhang, P.-S. Tsai, J. Cryer and M. Shah. *Shape from shading: a survey*. IEEE Transactions on Pattern Analysis and Machine Intelligence 21, 690-706, 1999.

[ZUÑIGA-SEGUNDO, 1994] A. Zúñiga-Segundo, F. Ruiz, C. Vázquez-López, J. González-Hernández, G. Torres-Delgado, D. V. Tsu. *Characterization of SiO₂ layers on Si wafers using atomic force microscopy*. J. Vac. Sci. Technol. A 12 (4), 2572-2576, 1994.

Annexes

- A) Mathematical relationships used in section II.3.1 for the simplification of stereoscopic calculations.
- B) Practical implementation of Tsai's shape-from-shading algorithm.
- C) Calculation of f and df/dZ for shape-from-shading algorithm implementation.
- D) E-mail exchanged with Zu-Han Gu about [Gu, 2002b] and [Gu, 2004a].

A) Mathematical relationships used in section II.3.1 for the simplification of stereoscopic calculations.

The rotation operation can also be considered as a change of base, from base (x,y,z) to base (x',y',z). It is consequently useful to notice that the inverse of the rotation matrix is such that

$$R_z(\theta)^{-1} = R_z(-\theta) = R_z(\theta)^T \quad (\text{A-1})$$

where the last element is the transpose of the rotation matrix. Another property used further in this report is that

$$R_z(\theta)R_z(\alpha) = R_z(\theta + \alpha) \quad (\text{A-2})$$

Finally, two trigonometric identities are used to simplify expressions:

$$\cos(p) - \cos(q) = -2 \sin\left(\frac{p+q}{2}\right) \sin\left(\frac{p-q}{2}\right) \quad (\text{A-3})$$

$$\sin(p) - \sin(q) = 2 \sin\left(\frac{p-q}{2}\right) \cos\left(\frac{p+q}{2}\right) \quad (\text{A-4})$$

B) Practical implementation of Tsai's shape-from-shading algorithm.

In the algorithm used for this work, a few points are modified in comparison with the initial Tsai's shape-from-shading algorithm.

First, the SEM image was rotated before applying the shape-from-shading algorithm, so that the upper limit of the waveguide sidewall appears horizontal. This then directly enables line roughness measurement at any vertical position on the sidewall. This operation does not a priori modify any computing parameter, as the tilt and slant angles are defined by imaging conditions.

Secondly, the image irradiance equation $I(x,y)=R(p,q)$ as formulated in chapter 2, is not a strict equality. The link between the image intensity and the surface's reflectance map is indeed a proportionality relation, and the introduction of a factor ρ is necessary, leading to the equation

$$I(x, y) = \rho R(p, q) \quad (\text{B-1})$$

This factor represents what is usually referred to as the albedo of the surface. However, for the practical implementation of the shape-from-shading algorithm [Ahammad, 2002], such a proportionality constant can be omitted, provided the image irradiance has previously been normalized [Horn, 1990].

Finally, in order to decrease calculation time, the gradient calculations are performed using matrix point-to-point operations, thus parallelizing this step. One reminds that gradients p and q are evaluated as follows

$$p = \frac{\partial Z}{\partial x} = Z(x, y) - Z(x-1, y) \quad (\text{B-2})$$

$$\text{and } q = \frac{\partial Z}{\partial y} = Z(x, y) - Z(x, y-1) \quad (\text{B-3})$$

Matrix replicas with shifted rows and columns are thus created to ease the calculations of q and p respectively. The consecutive calculations of $f(Z)$, $df(Z)/dZ$ and Z can then be summarized as a sequence of matrix sum or point-to-point multiplication.

C) Calculation of f and df/dZ for shape-from-shading algorithm implementation.

In the shape-from-shading approach of section II.4, the following formula is used to compute surface topography :

$$Z^n(x, y) = Z^{n-1}(x, y) + \frac{-f(Z^{n-1}(x, y))}{\frac{d}{dZ(x, y)} f(Z^{n-1}(x, y))} \quad (C-1)$$

Here the expression of f and df/dZ as a function of p and q is written explicitly.

$$\text{The function } f \text{ is defined as } f(Z(x, y)) = I(x, y) - R(p, q) \quad (C-2)$$

1) As a test, we first re-calculate the expression available in [Tsai, 94] for the case of Lambertian reflectance model. For this case, f takes the form :

$$f(Z(x, y)) = I(x, y) - \frac{pp_s + qq_s + 1}{\sqrt{1 + p_s^2 + q_s^2} \sqrt{1 + p^2 + q^2}} \quad (C-3)$$

Carrying out differentiation with respect to Z , one obtains Equation (C-4):

$$\frac{df(Z(x, y))}{d(Z(x, y))} = - \left\{ \frac{(p_s + q_s) \sqrt{1 + p_s^2 + q_s^2} \sqrt{1 + p^2 + q^2} - (1 + pp_s + qq_s) \left[\frac{1}{2} \frac{2(p+q)}{\sqrt{1 + p^2 + q^2}} \sqrt{1 + p_s^2 + q_s^2} \right]}{(1 + p_s^2 + q_s^2)(1 + p^2 + q^2)} \right\}$$

This, after simplifications turns into

$$\frac{df(Z(x, y))}{d(Z(x, y))} = - \left\{ \frac{(p_s + q_s)}{\sqrt{1 + p_s^2 + q_s^2} \sqrt{1 + p^2 + q^2}} - \frac{(p+q)(1 + pp_s + qq_s)}{\sqrt{1 + p_s^2 + q_s^2} \sqrt{(1 + p^2 + q^2)^3}} \right\} \quad (C-5)$$

which is the formula provided in [Tsai, 94].

2) Taking into account SEM model for $R(p, q)$, f takes the form [Bunrit, 2000]:

$$f(Z(x, y)) = I(x, y) - \frac{\sqrt{p+q+1} \sqrt{p_s+q_s+1}}{pp_s + qq_s + 1} \quad (C-6)$$

Differentiating with respect to $Z(x,y)$ leads to Equation (C-7) :

$$\frac{df(Z(x,y))}{d(Z(x,y))} = - \left\{ \frac{\frac{1+1}{2\sqrt{p+q+1}} \sqrt{p_s+q_s+1} (pp_s+qq_s+1) - (p_s+q_s) \sqrt{p+q+1} \sqrt{p_s+q_s+1}}{(pp_s+qq_s+1)^2} \right\}$$

which, after simplification, leads to

$$\frac{df(Z(x,y))}{d(Z(x,y))} = - \left\{ \frac{\sqrt{p_s+q_s+1}}{pp_s+qq_s+1} \left[\frac{1}{\sqrt{p+q+1}} - \frac{(p_s+q_s) \sqrt{p+q+1}}{(pp_s+qq_s+1)} \right] \right\} \quad (C-8)$$

D) E-mail exchanged with Zu-Han Gu about [GU, 2002b] and [GU, 2004a]

Alexis Bony wrote:

Dear Dr. Gu,

I am a Ph.D. student from the university of Strasbourg, France, working in the domain of nanorange surface metrology using SEM and light scattering. I was very interested in your publications on light scattering at grazing angles (Optics Letters, Vol 27, No 23, pp 2067-2069, 1st December 2002) and (Optical Engineering, Vol 43, No 3, pp 559-567, March 2004). I have a question concerning the experimental aspects of these studies.

The experimental curves in both publications look exactly the same. However, two parameters for the sample used for the measurements vary from the first publication (OL) to the second one (OE), namely the thickness of the dielectric layer (going from 52 μm in OL to 5.2 μm in OE) and its RMS roughness value (going from 6nm in OL to 60nm in OE). I would greatly appreciate if you could tell whether you got similar results with two different samples, or whether there was some typographical error in one of the publications.

Thank you in advance for your attention.

Best regards,
Alexis Bony.

Dear Alex:

Thank you for your e-mail. I have not checked the OE reprints yet. However, I have checked the reprints with our manuscript, and found the typographical error. We have used the $H = 5.2 \mu\text{m}$, and rms roughness value 60 angstrom.

Thanks.

Zu-Han